Experimental study on rheological properties of mantle minerals: Implication for subducting slab and the lower mantle

今村, 公裕

Experimental study on rheological properties of mantle minerals: Implication for subducting slab and the lower mantle

Masahiro Imamura

Department of Earth and Planetary Sciences, Graduate School of Science, Kyushu University

2018

Abstract

Seismic tomography images show various behaviors of subducting slabs such as the stagnation around the 660 km discontinuity or the depth of ~1000 km, and the penetration into the bottom of the lower mantle. To explain these behaviors, it is necessary to understand the strength of the subducting slabs. However, rheological properties of deep mantle minerals have been poorly constrained due to the difficulty of high-pressure deformation experiments.

In chapter 1, we report results of the deformation experiments in ringwoodite and wadsleyite at low temperatures, and discuss the strength of subducting slab in the mantle transition zone. The deformation experiments were carried out by in-situ X-ray observations at 7-18 GPa and 200-1000°C with a constant strain rate (0.96-9.1×10^{-5} s^{-1}) using the D-DIA and D-111 apparatuses installed at synchrotron facilities of Photon Factory Advanced Ring (PF-AR) and SPring-8.

The flow strength of ringwoodite obtained in this study was smaller than those estimated from diffusion and dislocation creep in the previous study. Dynamic recrystallization was not observed in recovered samples. These results suggest that ringwoodite deformed by the Peierls mechanism in this study. The creep data were fitted to the flow law of the Peierls mechanism, $\dot{\varepsilon} = \mathrm{A}\sigma^2 exp\left\{-\left(\frac{H_0}{RT}\right)\left[1-\left(\frac{\sigma}{\sigma_p}\right)^p\right]^q\right\}$, where

$\dot{\varepsilon}$ is the strain rate, A is a constant, σ is the stress, H_0 is the zero-stress activation enthalpy, σ_p is the Peierls stress, and p and q are the Peierls parameters. We could constrain the flow law of the Peierls mechanism in ringwoodite from our data assuming the several sets of Peierls parameters. The Peierls stress is estimated to be 6.4-8.3 GPa. Our results indicated that the flow strength of wadsleyite is lower than that of ringwoodite although the flow law of wadsleyite could not be constrained in this study.

The strength of the cold subducting slabs such as Tonga and Mariana slabs in mantle transition zone was estimated to be 200-900 MPa based on the Peierls mechanism of ringwoodite. It is desirable to conduct a numerical simulation studies on the slab dynamics taking more realistic rheology such as the Peierls mechanism into considerations.

In chapter 2, we report experimental results on the grain growth kinetics in pyrolitic material under lower mantle conditions, and discuss the rheology of the lower mantle and lower-mantle slabs based on the grain-size evolution inferred. Bridgmanite is a major phase in the lower mantle, and ferropericlase, Ca-perovskite, and majoritic garnet are present as minor phases. The grain size of the lower mantle minerals is largely controlled by the grain growth process after the grain-size reduction due to the post-spinel transformation. The grain growth kinetics can be described by $d^n-d_0^n=kt$ (d:

grain size, d_0: initial grain size, n: grain growth exponent, k: Arrhenius-type temperature-dependent rate constant, t: time). In the multi-phase system, the grain growth of major phase is controlled by Zener pinning and Ostwald ripening of minor phase, in which the grain size ratio between the major and minor phase can be described by the Zener relationship, $d_I/d_{II}=\beta/f_{II}^z$ (d_I: grain size of primary phase, d_{II}: grain size of secondary phase, f_{II}: volume fraction of secondary phase, β and z: Zener parameters).

In this study, the grain growth experiments of pyrolitic material were conducted at 25-27 GPa and 1600-1950°C for 30-3000 minutes. We analyzed the grain growth data obtained considering the grain growth kinetics in multi-phase system mentioned above. In the recovered samples annealed at 25 GPa, 4 phases of bridgmanite, ferropericlase, Ca-perovskite, and majoritic garnet were present, whereas at 27 GPa, 3 phases without majoritic garnet existed. The grains of minor phase were solely located at the grain boundary of the major phase of bridgmanite. The d_I/d_{II} ratio was roughly constant and estimated to be about 1.4 and 1.8 at 25 GPa (4-phase system) and at 27 GPa (3-phase system), respectively. These observations suggest that the grain growth of bridgmanite was controlled by Zener pinning and Ostwald ripening of the miner phase.

Our data on the d_I/d_{II} ratio with the volume fraction of minor phase are almost

consistent with the Zener relationship obtained in the previous study (Tasaka and Hiraga, 2013). The grain growth kinetics of bridgmanite, ferropericlase, and majoritic garnet in the 4-phase system were constrained from our grain growth data. Those in the 3-phase system was estimated by using the grain growth kinetics of ferropericlase in the 4-phase system and the Zener parameters (z=0.5, β=0.80). On the basis of these results obtained, we discussed the grain-size evolution and the dominant deformation mechanisms in the lower mantle.

Our grain growth data suggests that diffusion creep is largely dominant in the lower mantle and lower-mantle slabs. The deformation mechanism would change to the dislocation creep under relatively high-stress conditions such as the regions near the subducting slab and D" layer. Considering that the rate-controlling process is common between the grain growth kinetics and the diffusion creep in multi-phase system (e.g., Hiraga et al., 2016), the diffusion creep viscosity was also estimated. The viscosity of cold subducting slabs is thought to be lower than that of the surrounding warmer lower mantle at least at the top of the lower mantle (up to ~1000-1500 km depths) because of the smaller grain size. On the other hand, the lower mantle viscosity estimated from the geophysical model ($10^{21\text{-}23}$ Pas) may be explained if we consider the grain size of ~5-9 mm that can be achieved at the bottom of the lower mantle.

Contents

Chapter 1:

Deformation experiments of mantle transition zone minerals at low temperatures: Implications for the strength of subducting slabs

1.1. Introduction

Seismic tomography images that subducting slabs horizontally stagnate near the 660 km discontinuity (stagnant slab) or around 1000 km, and descend into the lower mantle (e.g., Fukao and Obayashi, 2013). It was suggested that several factors such as trench retreat, negative Clapeyron slope of the post-spinel transformation, the lower mantle viscosity, dip angles, and strength of subducting slabs affect behaviors of deep subducting slabs (e.g., Torii and Yoshioka, 2007; Nakakuki and Mura, 2013). In this chapter, we focus on the strength of subducting slabs in the mantle transition zone.

Phase equilibrium studies on the pyrolite material have revealed that wadsleyite and ringwoodite are major constituent minerals at mantle transition zone (Fig. 1.1) (e.g., Ringwood, 1991). To understand the rheology of the deep slab in the mantle transition zone, it is necessary to constrain the flow laws of wadsleyite and ringwoodite at low temperatures.

Flow law can be described below.

$$\dot{\varepsilon} = Ad^{-m}\sigma^{n}\exp(^{-H^{*}}/_{RT}) \qquad (1.1)$$

, where A is constant, d is grain size, σ is the differential stress, H^{*} is the activation enthalpy, R is gas constant, T is temperature (e.g., Frost and Ashby, 1982). The m and n values depend on the deformation mechanism. The diffusion creep has grain-size dependent newtonian rheology (n=1 and m=2 or 3 for volume and grain-boundary diffusion), whereas the dislocation creep has grain-size independent non-newtonian rheology (n=3-5 and m=0). The dominant deformation mechanism changes with stress and grain size conditions, which is generally described by a deformation mechanism map. As an example, the deformation mechanism map in dry olivine is shown in Fig. 1.2 (Katayama and Karato, 2008). The diffusion creep is dominant under the small grain size and low stress conditions (a of Fig. 1.2). The dislocation creep is dominant at high stress and large grain size conditions (b of Fig. 1.2). At the higher stress conditions than several hundreds of MPa, Peierls mechanism becomes dominant (c of Fig. 1.2).

In the Peierls mechanism, strain rates increase with stress more rapidly than a power-law relationship of dislocation creep (power-law breakdown, e.g., Karato, 2008). The flow law is described as follows:

$$\dot{\varepsilon} = B\sigma^{2}exp\left\{-\left(\frac{H_0}{RT}\right)\left[1-\left(\frac{\sigma}{\sigma_p}\right)^{p}\right]^{q}\right\} \qquad (1.2)$$

, where B is constant, H_0 is the zero-stress activation enthalpy, σ_p is the Peierls stress,

p and q are the Peierls parameter ($0 \leq p \leq 1$, $1 \leq q \leq 2$, Kocks et al., 1975; Frost and Ashby, 1982). In this mechanism, the activation enthalpy decreases with stress and becomes zero at a threshold value of Peierls stress (e.q. 1.2). The strength in this regime is weakly dependent with temperature and strain rate, and therefore often referred to as yield strength. Fig. 1.3 shows an example of the appearance of the Peierls mechanism in olivine (Tssen and Carter, 1987). The deviation from the power-law relationship in the dislocation creep can be seen at lower temperatures and higher stress conditions.

Several studies have discussed the rheology of the subducting slab in the mantle transition zone. Karato et al. (2001) proposed the 2D deformation mechanism maps in subducting slab based on the flow law of analogue materials. The strengths of the deep slab such as Mariana and Tonga slabs had been considered by the previous studies (e.g., Kubo et al., 2009; Kaneshima and Yoshioka, 2014) mainly based on the flow law derived from the Si diffusivity in ringwoodite (Shimojuku et al., 2009). However, the strength of deep slab has not been discussed directly from the creep strength of ringwoodite.

Some studies have reported the flow law of ringwoodite without conducting quantitative deformation experiments. Xu et al. (2003) conducted the stress relaxation experiments of $(Mg_{0.9}, Fe_{0.1})_2SiO_4$ ringwoodite and estimated the flow law for the

Peierls mechanism of ringwoodite. Shimojuku et al. (2009) has conducted the diffusion experiments of $(Mg_{0.9}, Fe_{0.1})_2SiO_4$ ringwoodite, and constructed flow laws for diffusion creep and dislocation creep of ringwoodite based on the Si diffusivity.

In order to conduct the quantitative deformation experiments at mantle transition zone pressures, several types of deformation apparatus have been developed so far. Among them, we focus on two kinds of deformation apparatus as follows. The first is Deformation-DIA (D-DIA) type apparatus (Wang et al., 2003) that is generally used in combination with synchrotron X-ray. Nishiyama et al. (2005) first performed quantitative deformation experiments of $(Mg_{0.9}, Fe_{0.1})_2SiO_4$ ringwoodite at around 10 GPa and room temperature by using D-DIA apparatus, and reported the strength of ringwoodite measured by using synchrotron monochromatic X-ray. Kawazoe et al. (2016) further conducted the similar D-DIA experiments up to 18 GPa and 1427°C, and proposed the flow law for dislocation creep of $(Mg_{0.9}, Fe_{0.1})_2SiO_4$ ringwoodite. However, no deformation experiments were performed under relatively low temperature conditions to construct the flow law of the Peierls mechanism of ringwoodite..

Another deformation apparatus is D-111 type apparatus developed in Hunt et al. (2014) that can generate mantle transition zone pressures, in which Kawai-type multi-anvil apparatus was modified for deformation experiments at constant strain rate.

This deformation apparatus can also be used for synchrotron radiation study. It is expected that the deformation experiments will be carried out at higher pressures than those usually generated using the D-DIA apparatus.

In this study, the deformation experiments of wadsleyite and ringwoodite were conducted at low-temperature and high-stress conditions using D-DIA and D-111 apparatuses. We will report the flow law for the Peierls mechanism of ringwoodite and some implications for the rheology of the subducting slab in the mantle transition zone.

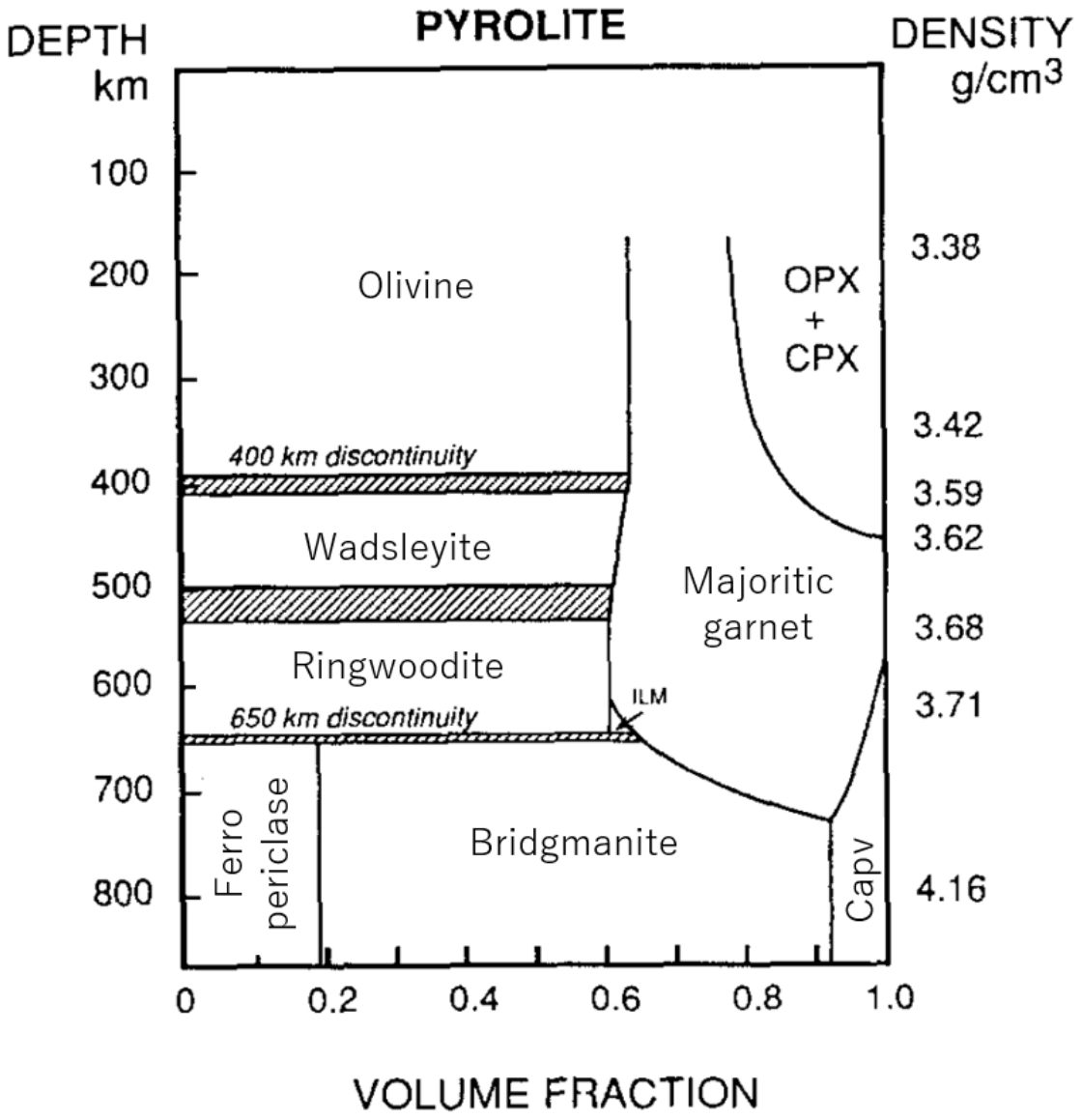

Fig. 1.1 Phase relation in pyrolite material (modified from Ringwood 1991). Wadsleyite and ringwoodite are major constituent minerals in the upper and lower parts of mantle transition zone, respectively.

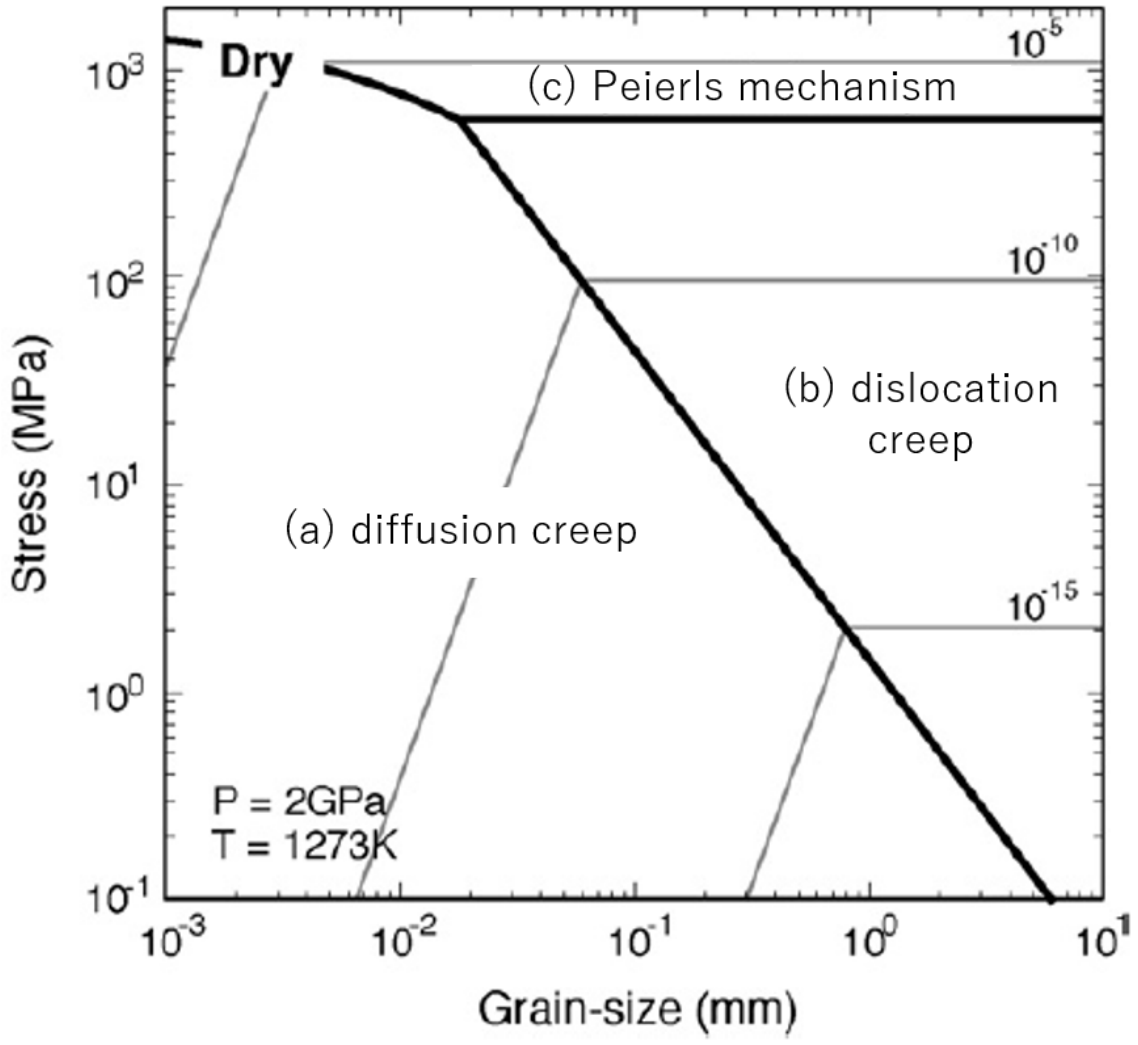

Fig. 1.2 Deformation mechanism map for olivine (modified from Katayama and Karato, 2008, a: diffusion creep regime, b: dislocation creep regime, c: Peierls mechanism regime).

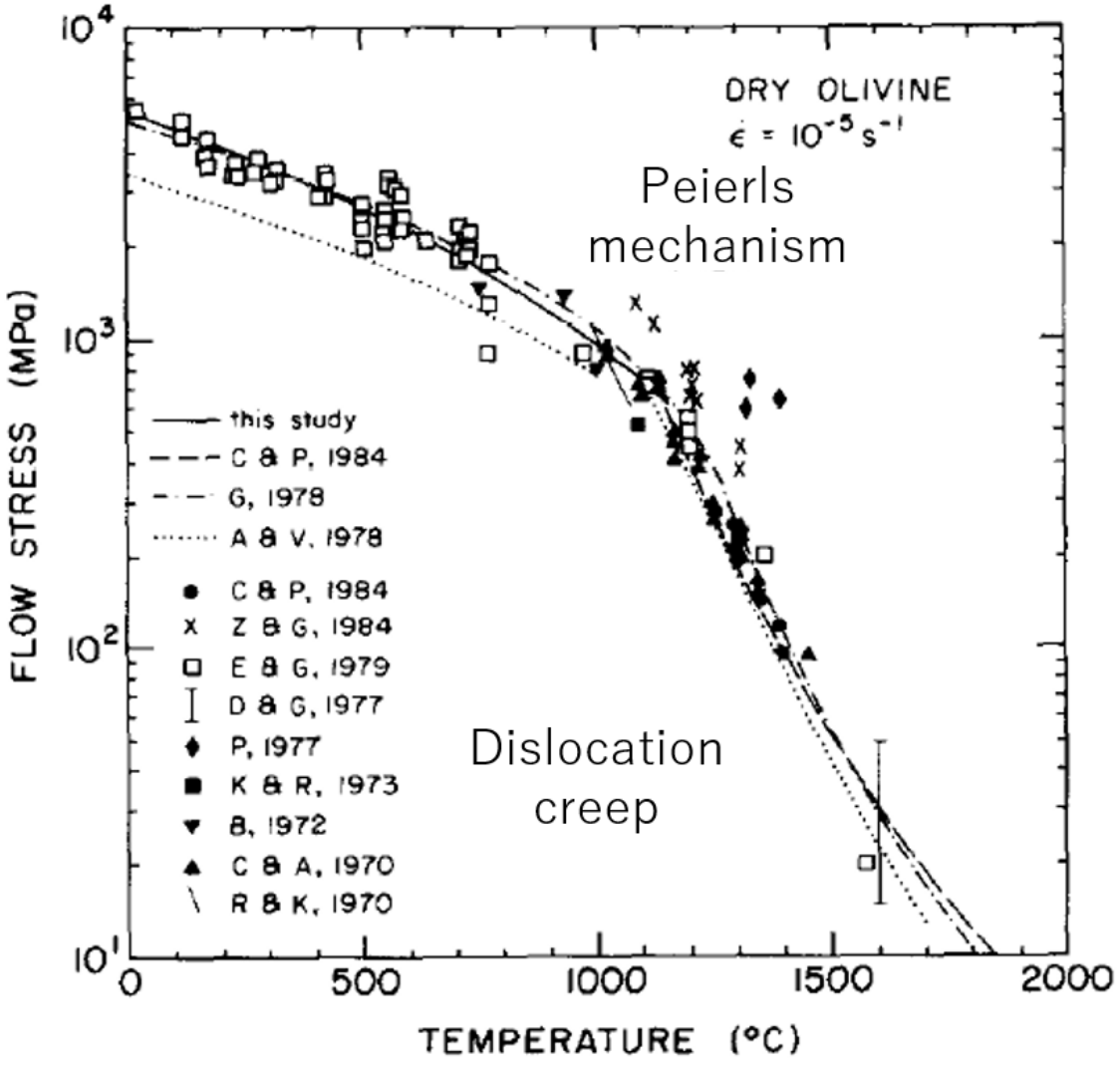

Fig. 1.3 Temperature dependence of flow stress in olivine at the constant strain rate (modified from Tssen and Carter, 1987). The Peierls mechanism is dominated at low temperatures up to about 1100°C and high stress above about 8×10^2 MPa.

1.2. Experimental procedures

1.2.1. Synthesis of starting materials

Starting materials for deformation experiments were cylindrical polycrystalline wadsleyite and ringwoodite. These were synthesized from cylindrical single crystal San Carlos Olivine ($(Mg_{0.90}, Fe_{0.10})_2SiO_4$) with the diameter of 0.6-0.9 ± 0.01 mm and length of 0.9-1.0 ± 0.01 mm.

The synthesis experiments of wadsleyite and ringwoodite were conducted at 16 GPa and 1400°C for 1 h, and 22 GPa and 1400°C for 3 h, respectively, using Kawai type multi-anvil apparatus installed at Kyushu University (QDES) (Fig. 1.4). Tungsten carbide (WC) anvils with a truncated edge length of 3.0 mm (Fujiloy F08) were used. The sample assembly is shown in Fig. 1.5. This is composed of a (Mg,Co)O pressure medium and a $LaCrO_3$ heater, MgO spacers. Cylindrical San Carlos Olivine was packed by high purity and fine-grained NaCl powder (99.999%) in the graphite capsule.

The diameter and length of the synthesized wadsleyite are 0.77 ± 0.01 and 1.00 ± 0.01 mm, respectively. Two different sizes of ringwoodite were synthesized in this study. The smaller one is 0.55 ± 0.01 in diameter and 0.74 ± 0.01 mm in height. The larger one is 0.80 ± 0.01 in diameter and 0.99 ± 0.01 mm in height. These starting materials have equigranular texture and the grain size is ~10-30 μm (Fig. 1.6).

Fig. 1.4 Kawai-type multi-anvil apparatus (QDES) installed at Kyushu university.

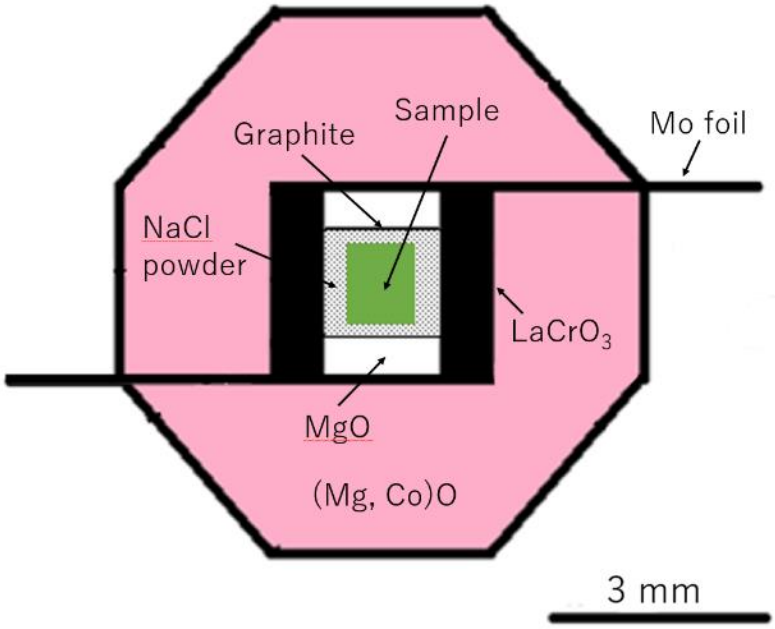

Fig. 1.5 Cross section of the sample assembly used for synthesis of starting materials.

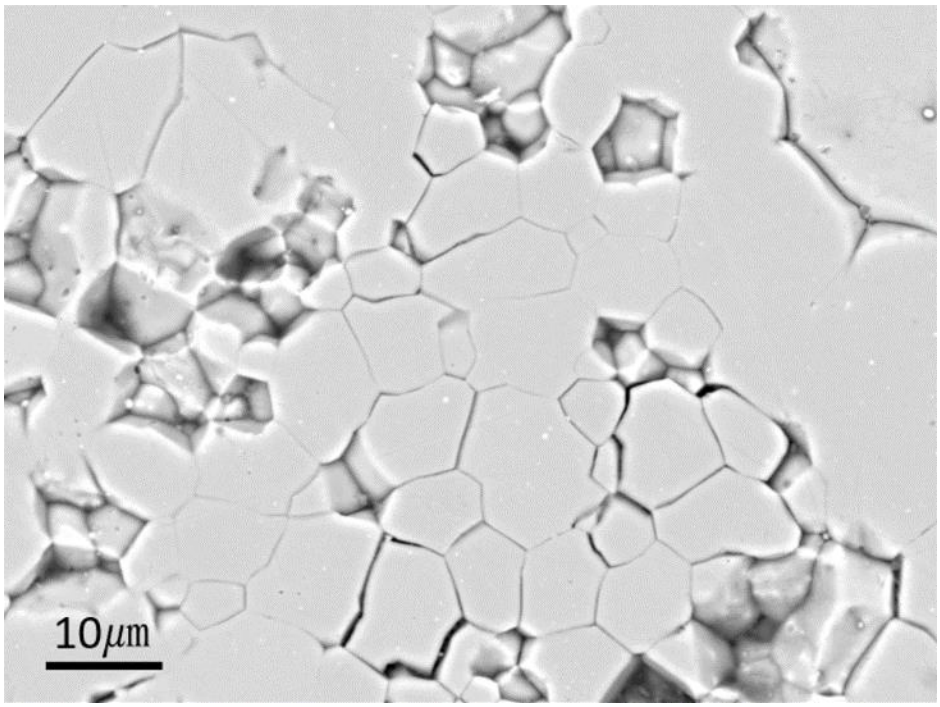

Fig. 1.6 Backscattered electron image of starting material (ringwoodite).

1.2.2. Deformation experiments

Deformation experiments were conducted using two D-DIA apparatuses (MADONNA I and DCAP) installed at BL04B1 beamline of SPring-8 and NE-7 beamline of PFAR in High Energy Accelerator Research Organization (KEK), respectively (e.g., Shiraishi et al., 2011, Fig. 1.7). Fig. 1.8 shows a schematic drawing of the D-DIA apparatus. D-111 type deformation apparatus was also used at the NE7 beamline.

White X-rays from bending magnet source are monochromatized to energies of 50 or 60 keV using Si (111) double-crystal monochromator. Energy of the monochromatic X-ray is calibrated by using double cassette method at NE-7 and/or Ge solid state detector (SSD) at BL04B1. Two-dimensional X-ray diffraction (2D-XRD) pattern was measured by CCD detector, imaging plate (IP), or flat panel detector. X-ray radiography images were taken using a CCD camera installed at downstream of the deformation apparatus. X-ray radiography images and 2D-XRD patterns are taken every 6 minutes during the deformation experiments. Fig. 1.9 shows the schematic figure of the D-DIA system for in-situ X-ray observation. Monochromatic X-ray was collimated to 200 μm × 200 μm and 2 mm ×2 mm when taking 2D-XRD patterns and radiography images, respectively.

Pressure was generated by multi-anvil 6-6 assembly (MA6-6, e.g., Nishiyama et al., 2008) in D-DIA deformation experiments (Fig. 1.10). The deformation experiments were conducted at about 7-10 GPa and 11-14 GPa using tungsten carbide anvils with a TEL of 4.0 and 2.5 mm, respectively. Those with a TEL of 3.0 mm were used for the pressure generation test. For acquiring 2D-XRD patterns, conical slotted anvil or cBN anvil were used at the downstream side (Fig. 1.11).

The sample assemblies for deformation experiments using D-DIA apparatus are shown in Fig. 1.12. These are composed of a amorphous boron + epoxy pressure medium, a graphite heater, a MgO insulator, dense Al_2O_3 pistons, porous Al_2O_3 backup rods, and Cu ring electrodes. Temperature is measured using a W3%Re-W25%Re thermocouple. Fig. 1.13 shows the relationship between temperature and supplied electric power. The ends of the thermocouple are grounded on a secondary anvil in MA6. Teflon spacers were used for the experiments using tungsten carbide anvils with a TEL of 4.0 and 3.0 mm. On the other hand, the pyrophyllite gaskets fired at 700°C for 30 minutes were used for the deformation experiments using tungsten carbide anvils with a TEL of 2.5 mm.

A D-111 apparatus was newly installed at NE7 beamline at March, 2017 (Nishihara et al., 2017, Fig. 1.14). The Kawai-type multi-anvil 8 (MA-8) assembly is set

at the center of D-111 type guide block (Fig. 1.15). Tungsten carbide anvils with a TEL of 2.0 mm were used for the MA-8 assembly. The relationship between loads and pressure was shown in Fig. 1.16. The method of the pressure measurement was described in a section 1.2.3. The spear-shaped anvils were set at the top and the bottom of the MA-8 assembly, and were independently moved by differential hydraulic rams at high pressure and temperatures (Fig. 1.17). Two kinds of slotted anvils were used for X-ray observation in the D-111 experiments (Fig. 1.18). Two anvils slotted rectangularly with a width of 0.80 mm and a depth of 0.20 mm were used for the incident X-ray. The anvil set at downstream side was slotted rectangularly and conically to take 2D-XRD patterns (Fig. 1.19).

The sample assembly for the D-111 apparatus is shown in Fig. 1.20. This is composed of a (Mg,Co)O pressure medium and a cylindrical $LaCrO_3$ heater. The cylindrical polycrystal ringwoodite was put in a graphite cylindrical capsule and sandwiched by dense Al_2O_3 pistons. To increase X-ray transmission, MgO rods and graphite disks are used in the X-ray path. W3%Re-W25%Re thermocouple is used for temperature measurements. Fig. 1.21 shows the relationship between temperature and supplied electric power.

In both experiments using D-DIA and D-111, starting materials were

compressed at room temperature and heated to desired values of 200-1000°C. Then, the sample was uniaxially deformed with a constant displacement rate of top and bottom anvils.

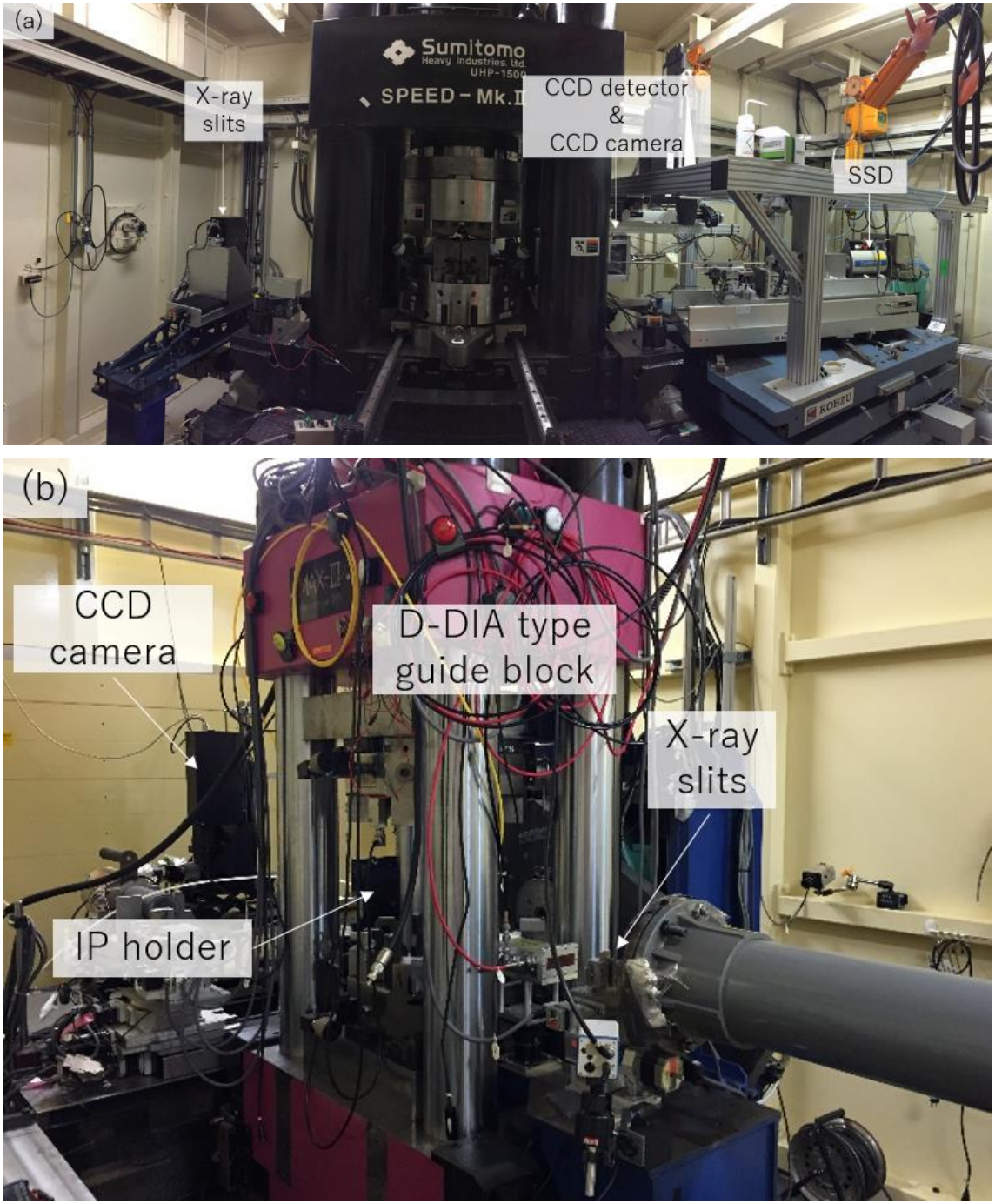

Fig. 1.7 D-DIA apparatus and experimental set up in the synchrotron beamlines of BL04B1 at SPring-8 (a) and NE-7 at PFAR (b).

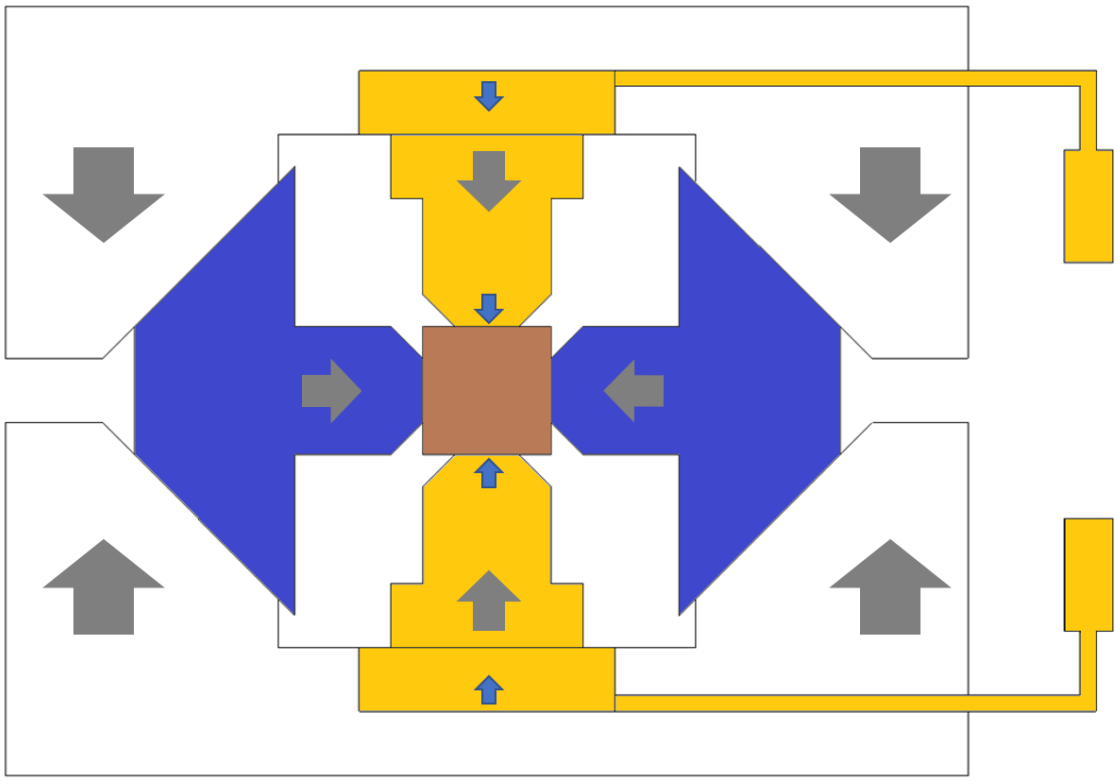

Fig. 1.8 Schematic figure showing the D-DIA apparatus. The MA6-6 assembly is compressed by the main hydraulic ram to generate the hydrostatic pressure (gray arrows). In the deformation stage, two second stage anvils at the top and the bottom independently moved with a constant speed by the differential hydraulic ram (blue arrows).

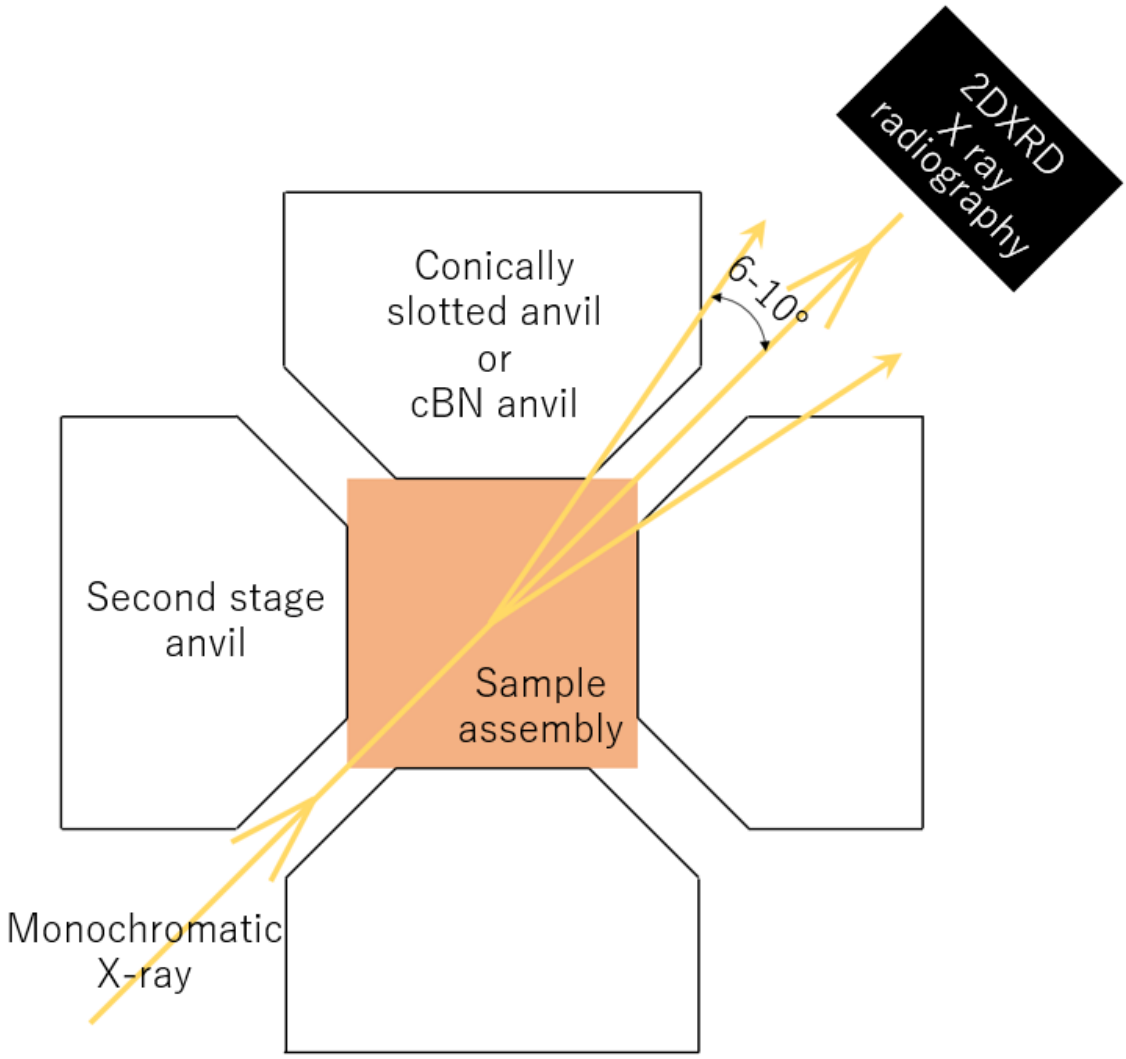

Fig. 1.9 Schematic figure showing the MA6-6 system for in-situ X-ray observation. High energy (50-60 keV) monochromatic X-ray was used as incident X-ray beam to acquire the 2D-XRD patterns and X-ray radiography images. We used only one conically slotted WC anvil or cBN anvil to avoid blowouts, resulting that half of the whole Debye ring was obtained.

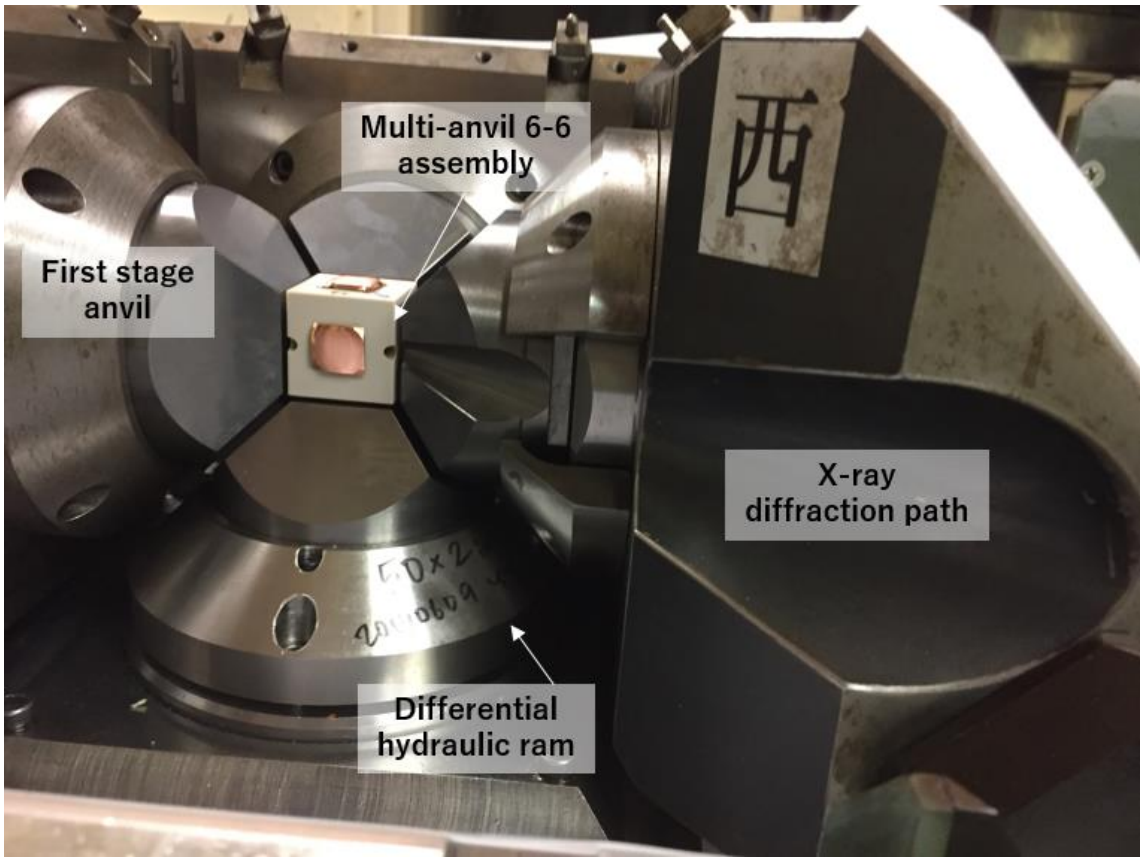

Fig. 1.10 Multi-anvil 6-6 assembly inside the D-DIA apparatus. The first stage anvil and the sliding block at the downstream side were conically slotted to take the X-ray diffraction data.

(a)

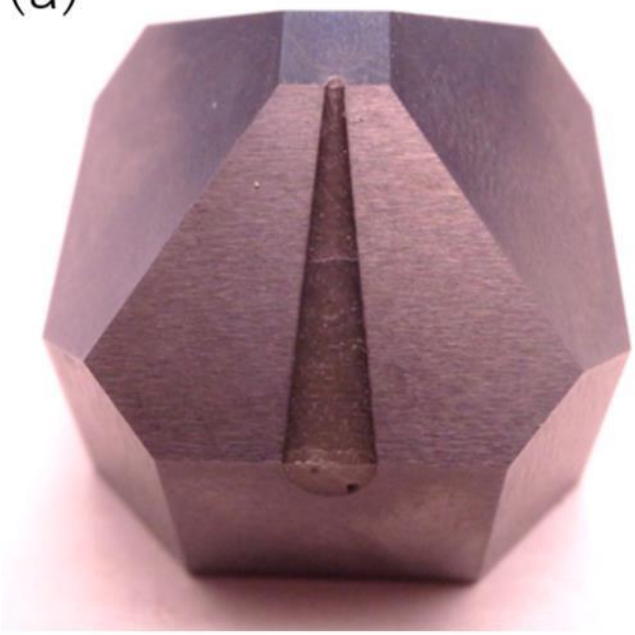

(b)

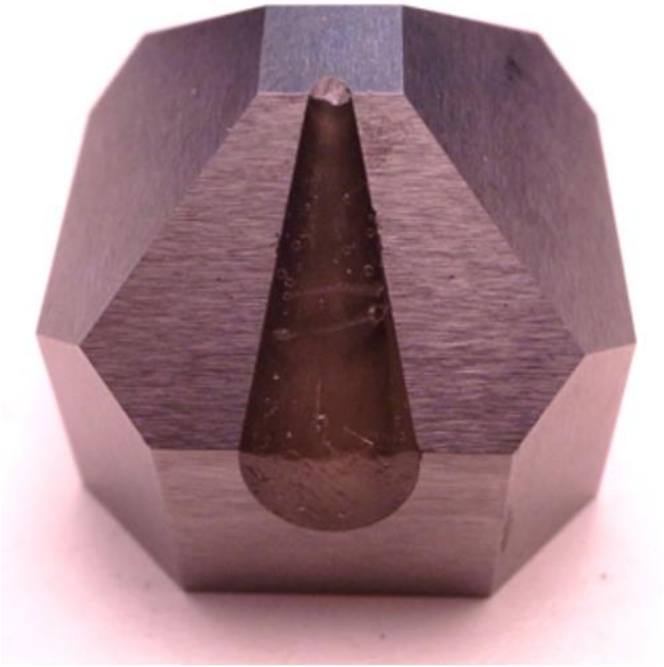

(c)

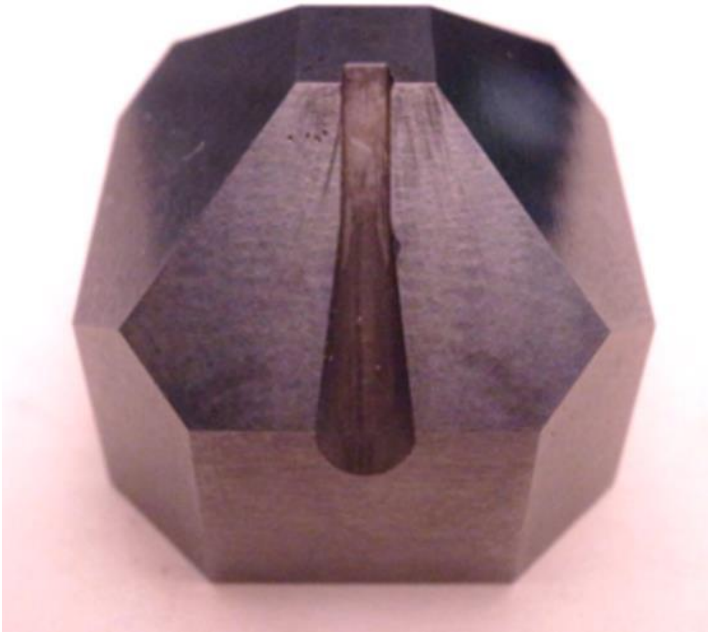

Fig. 1.11 Tungsten carbide anvils with a TEL of 4.0 mm are conically slotted by 6 or 11 degrees ((a): 6 degrees, (b): 11 degrees). The anvil with a TEL of 2.5 mm is cut with a rectangular shape in 1.4 mm width and 0.65 mm depth, and is conically slotted by 6 degrees (c).

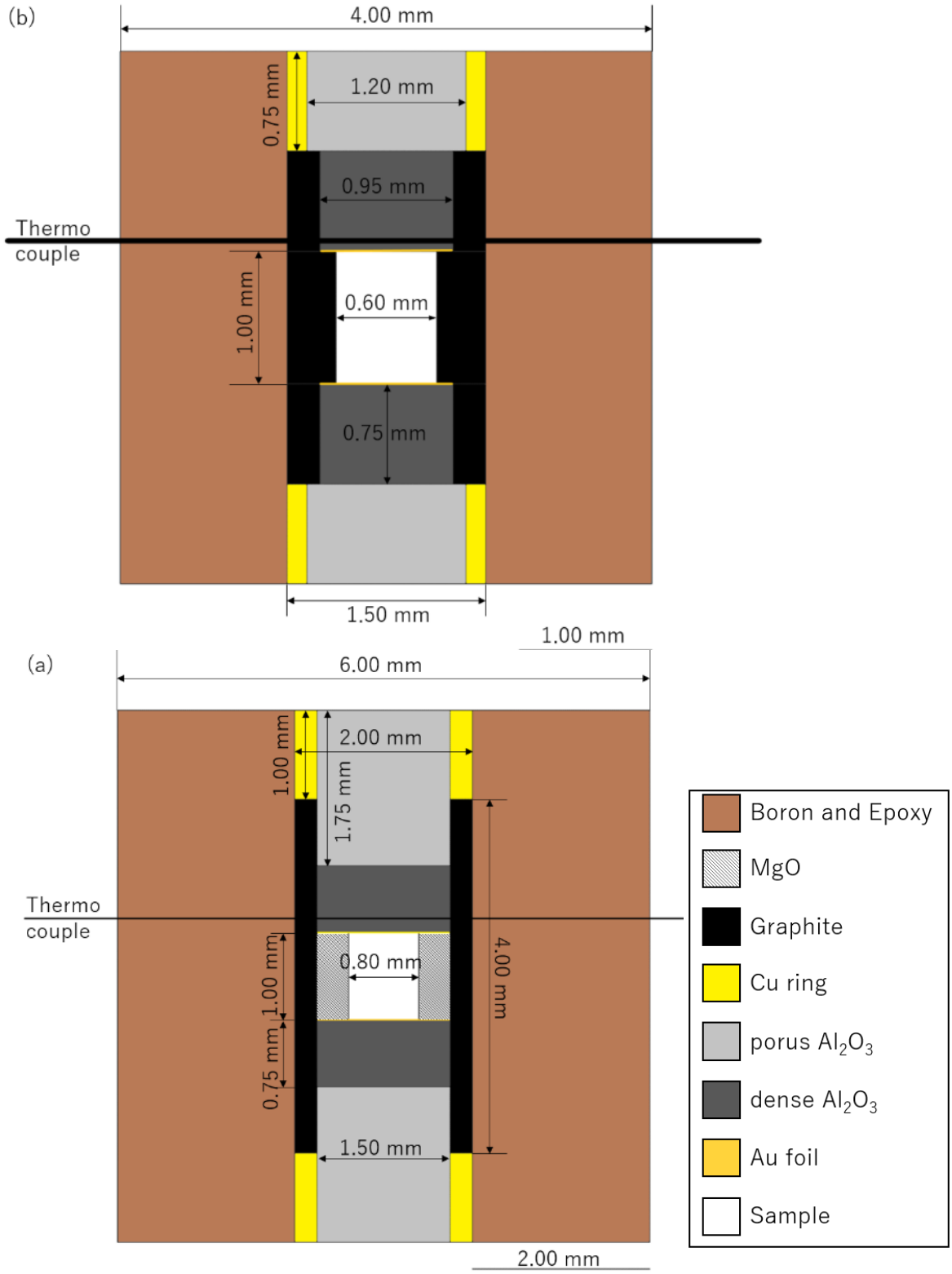

Fig. 1.12 Cross section of sample assembly for deformation experiments using D-DIA apparatus and tungsten carbide anvils with a TEL of 4.0 mm (a) and 2.5 mm (b).

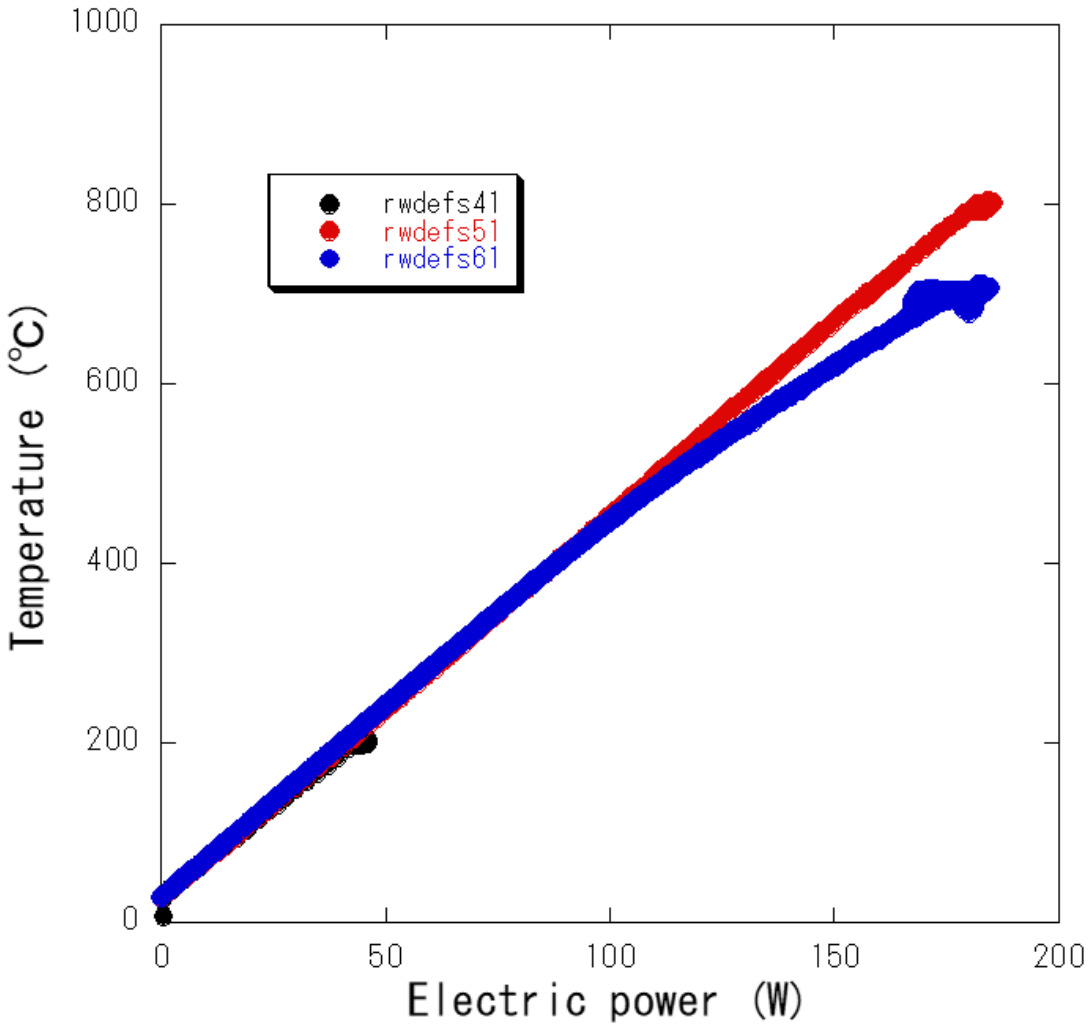

Fig. 1.13 The relationship between temperature and supplied electric power in the D-DIA system at 75 tons with a TEL of 4.0 mm (black and red), and at 60 tons with a TEL of 2.5 mm (blue).

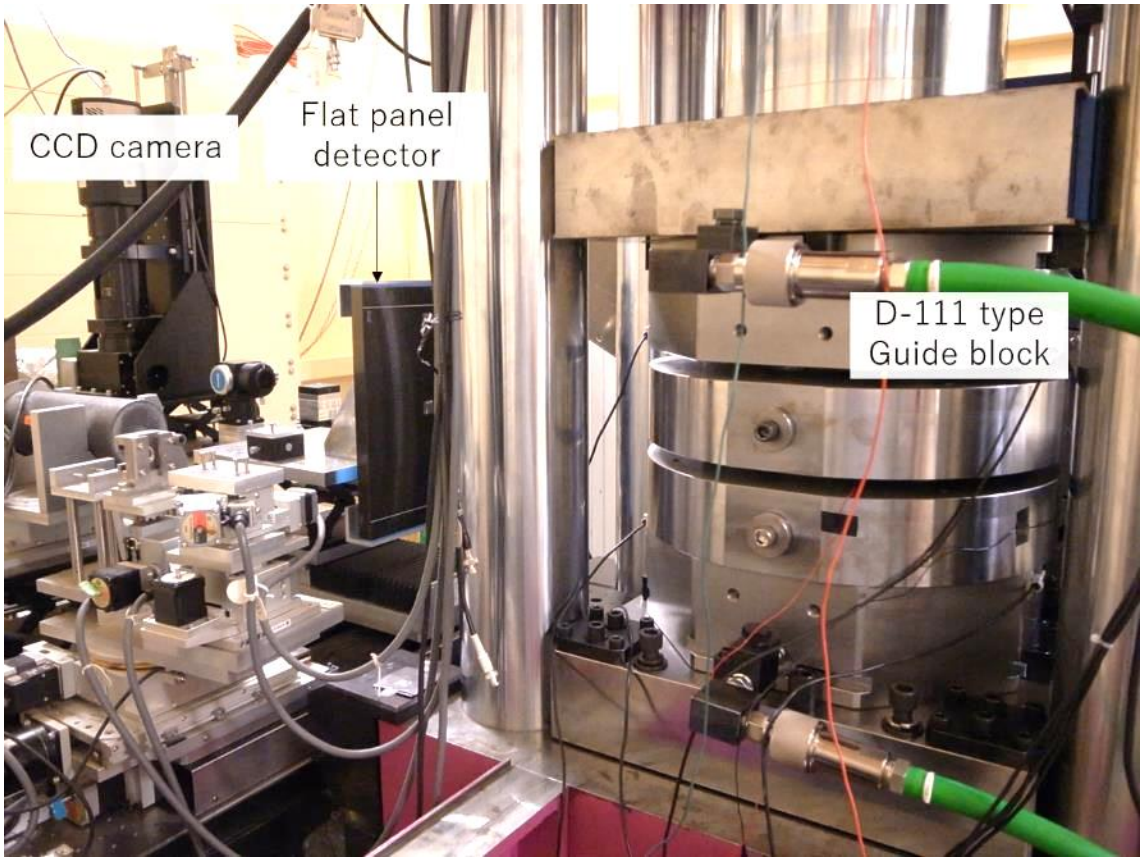

Fig. 1.14 D-111 apparatus and experimental setup at NE-7 beamline of PFAR.

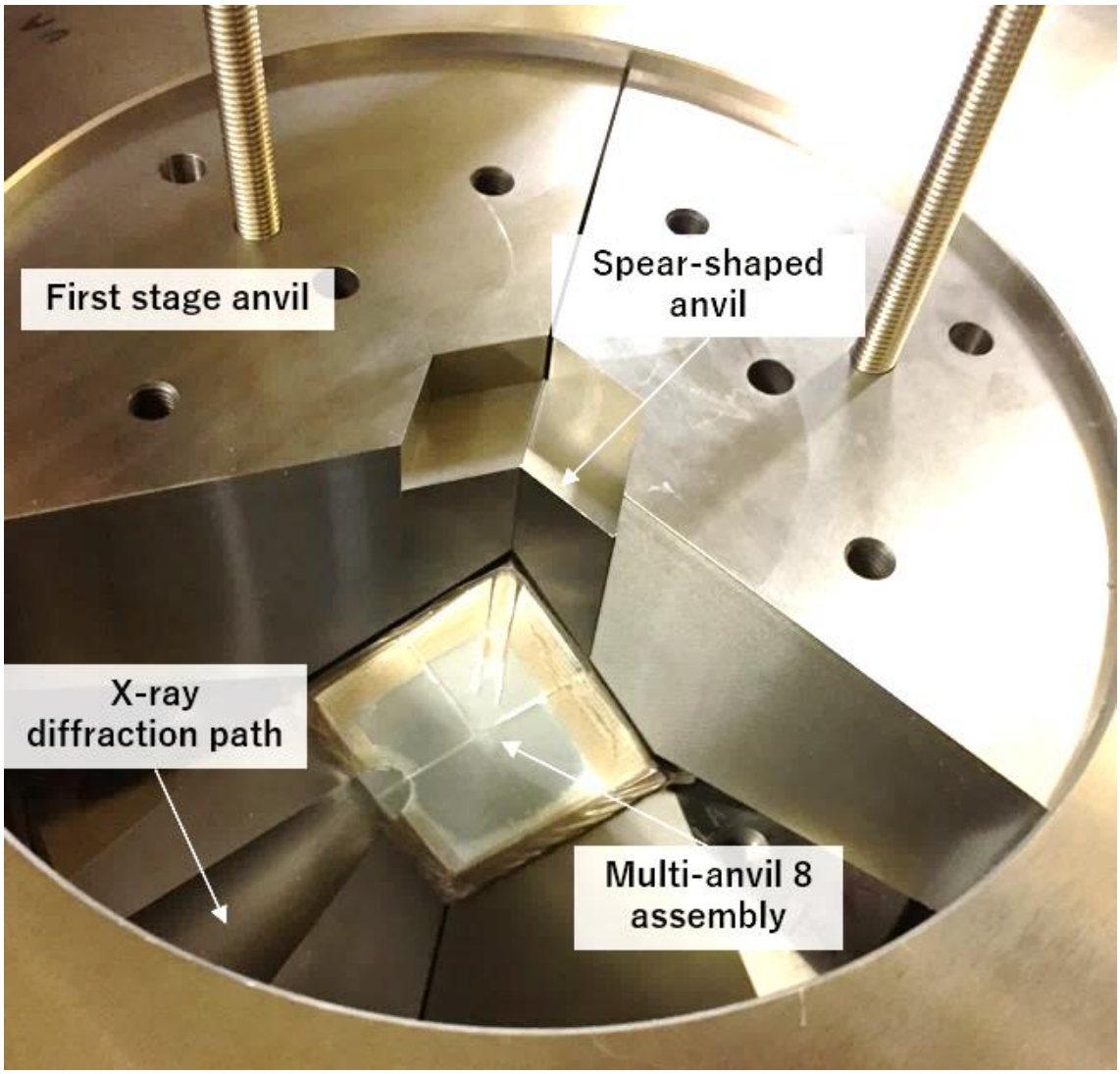

Fig. 1.15 Inside the D-111 apparatus. Spear-shaped anvils are independently moved with a constant speed at high pressures during the deformation stage.

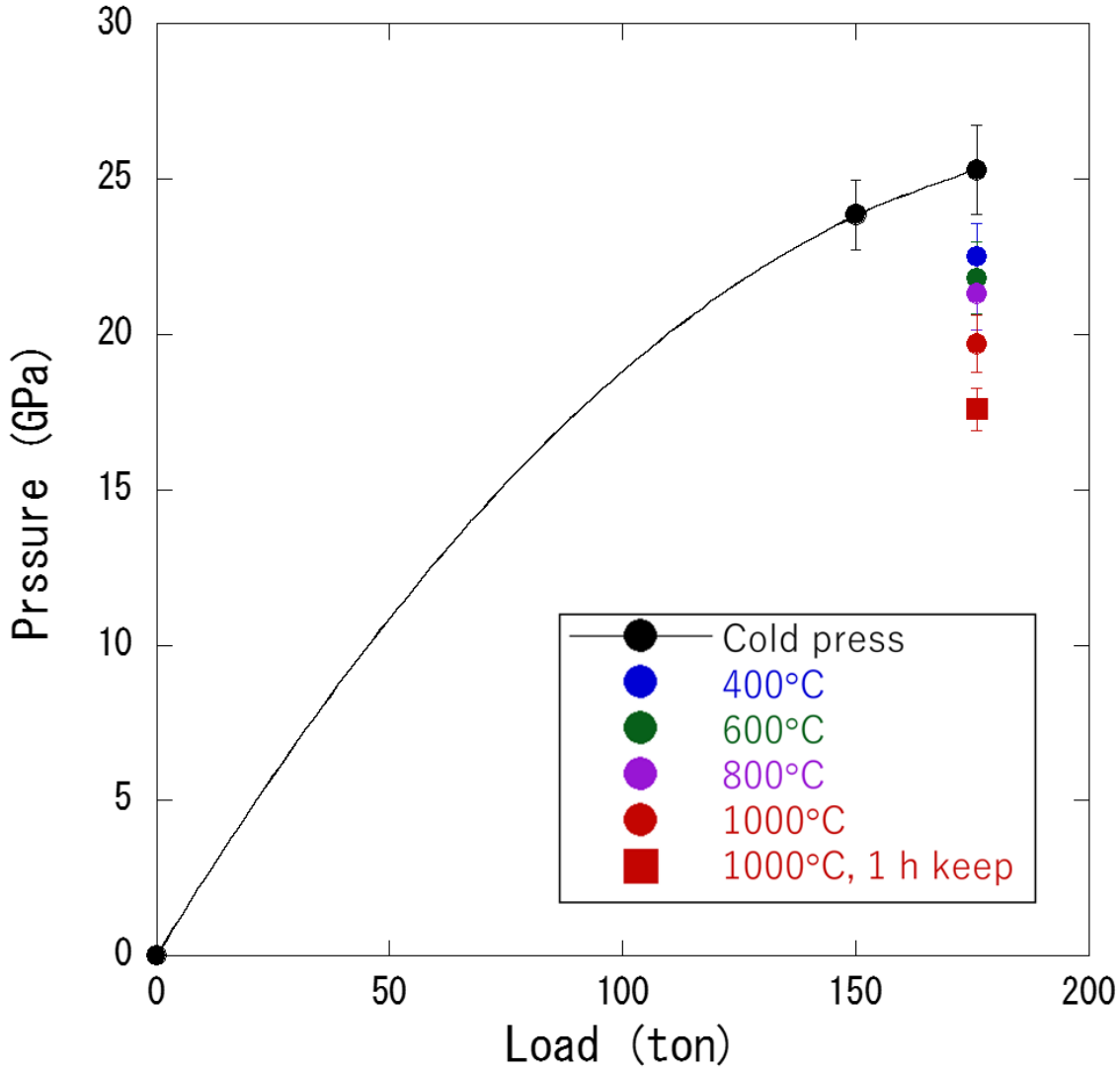

Fig. 1.16 Plots of generated pressures with the applied load at several temperatures.

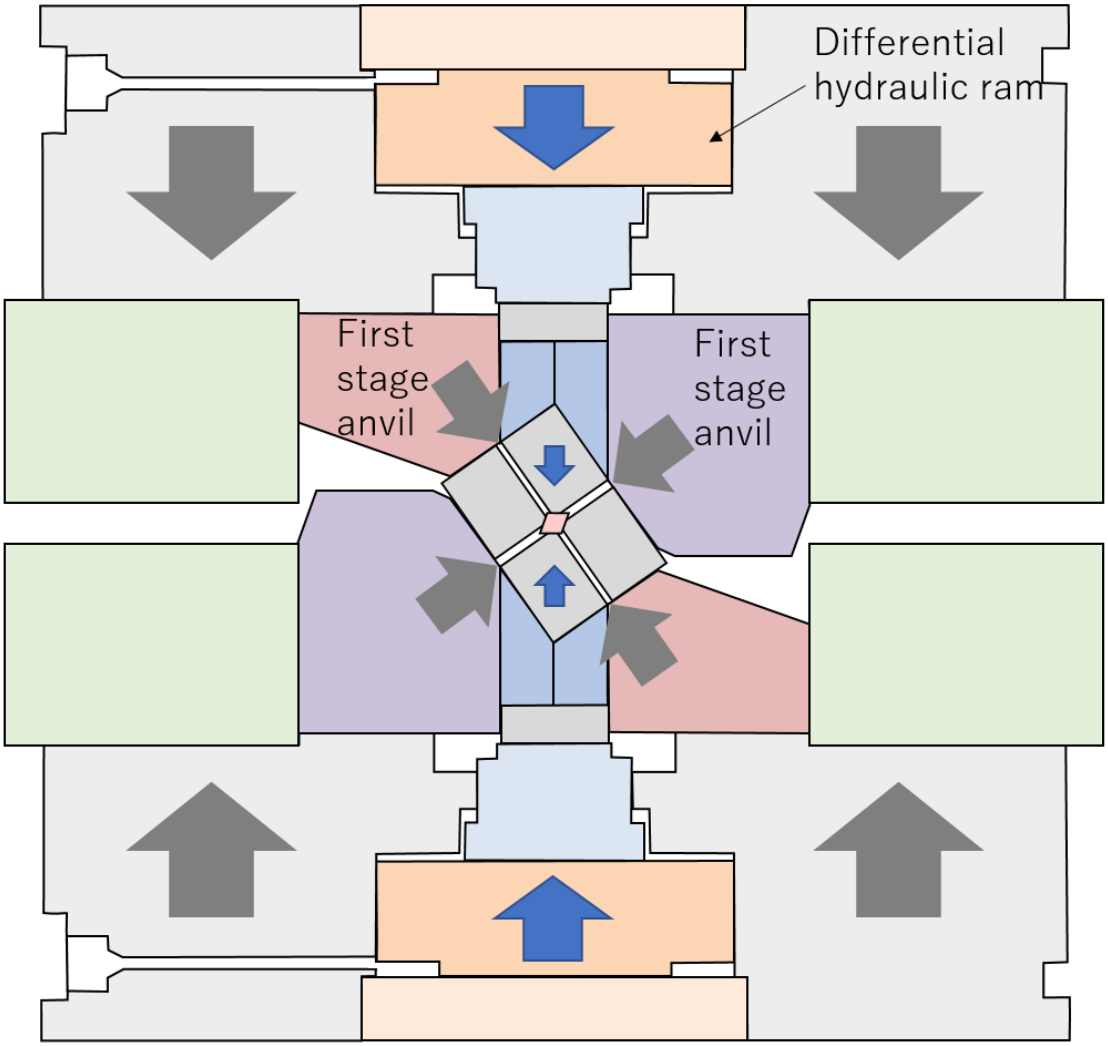

Fig. 1.17 Schematic figure showing the D-111 apparatus. The MA8 assembly is compressed by hydraulic ram to generate confining pressure. Two second-stage anvils at the top and the bottom is moved independently by the differential hydraulic rams at high pressures (blue arrows).

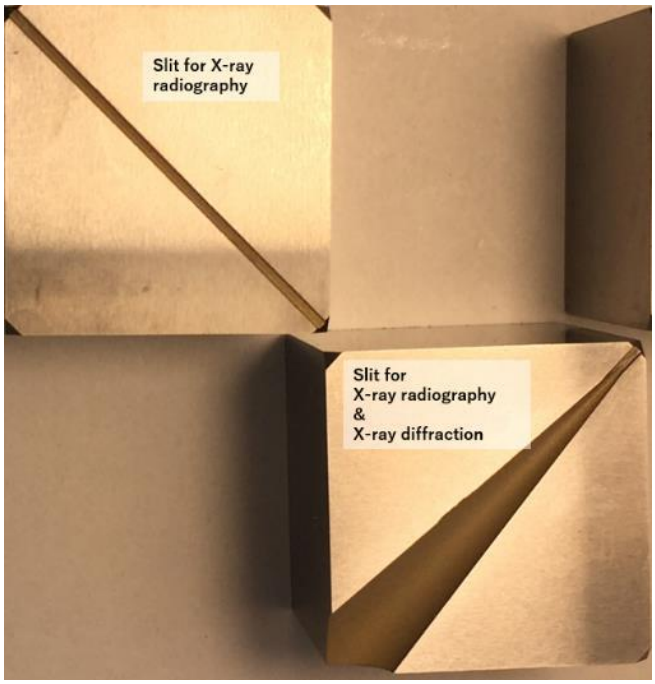

Fig. 1.18 Two types of slotted anvils used for the D-111 apparatus. The rectangular slotted anvils (upper left) and the rectangular and conically slotted anvils (lower right) are used at the upstream and downstream sides of the sample assembly, respectively.

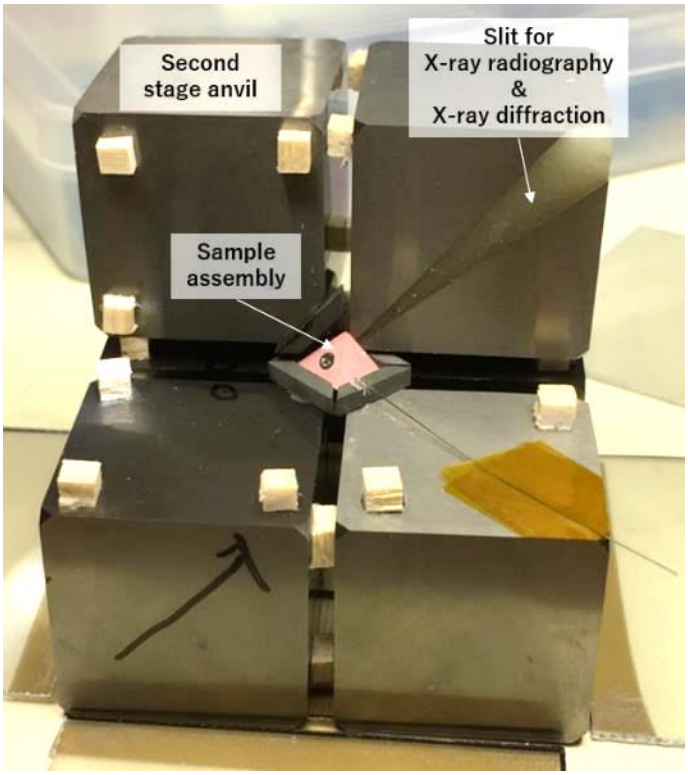

Fig. 1.19 MA-8 assembly used for the D-111 apparatus.

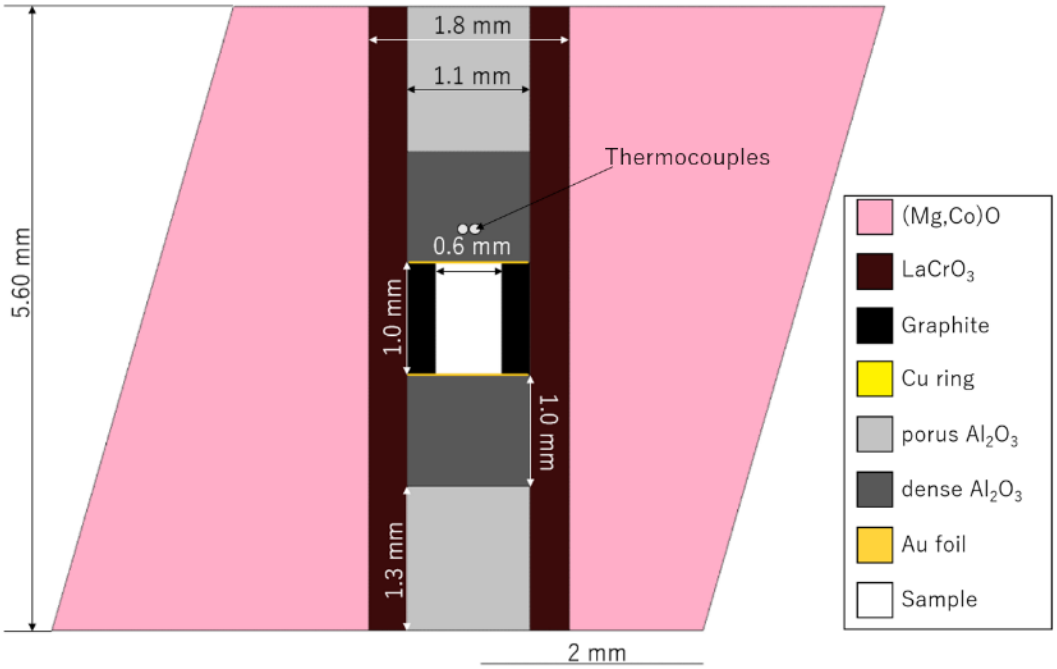

Fig. 1.20 Cross section of the sample assembly used for deformation experiments with D-111 apparatus.

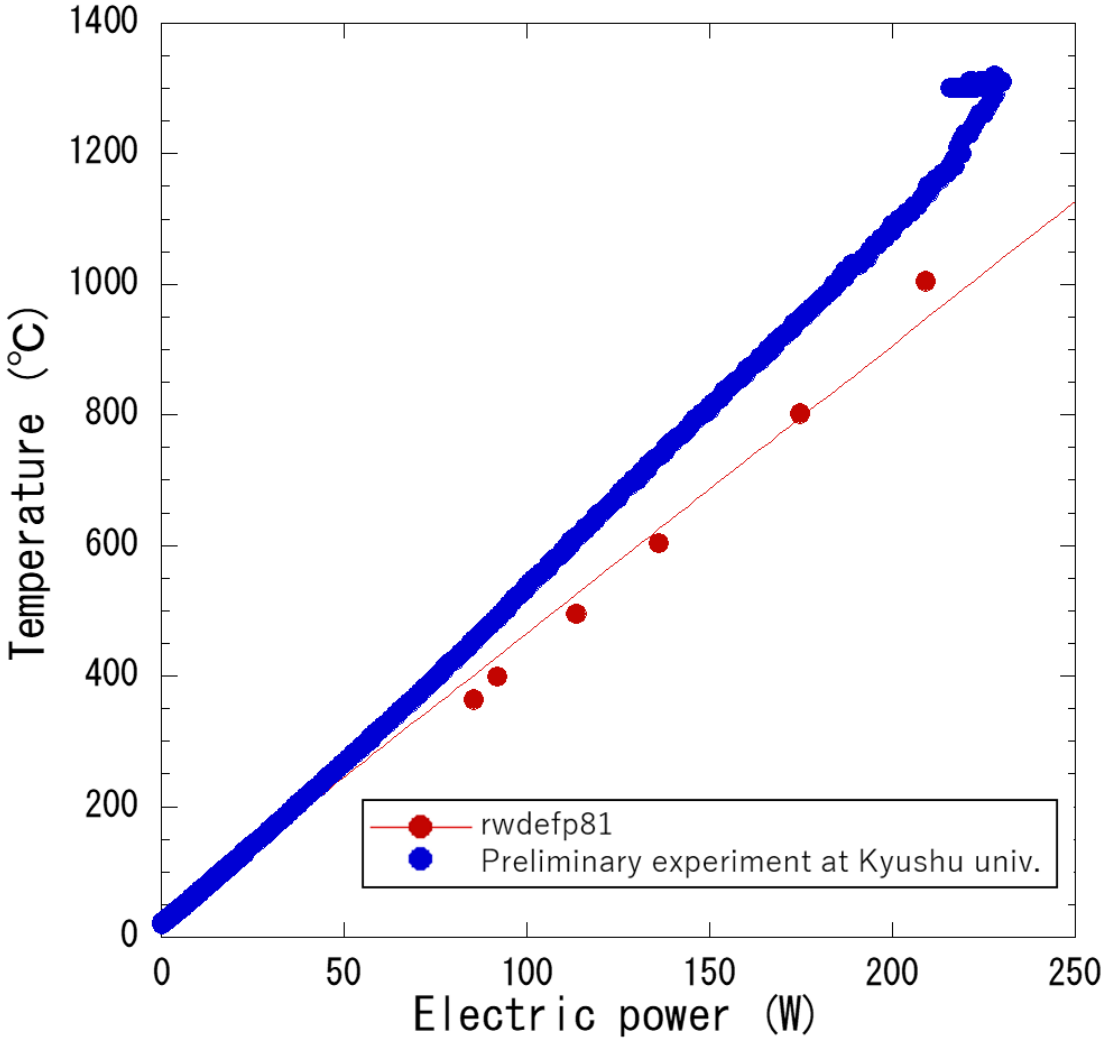

Fig. 1.21 Relationship between temperature and supplied electric power at several pressures. The preliminary experiment was conducted at 150 tons by using KAWAI-type apparatus (QDES) (blue). The deformation experiment was conducted at 176 tons using the D-111 apparatus at NE-7 beamline of PFAR (red).

1.2.3. Pressure, stress and strain measurements

The methods of the pressure, stress, and strain rate measurements are same in the different deformation apparatuses used in this study. These are based on the previous studies (e.g., Uchida et al., 2004).

Two anvils are necessary for X-ray windows to obtain a full circle of Debye ring. However, because only one conically slotted WC anvil or cBN anvil was used to avoid the blowouts in the case of the D-DIA experiment, only a half of the 2D-XRD pattern was obtained (Fig. 1.22a). Under high-pressure conditions, the anvil gap of MA6-6 became narrow, so the shaded area in the 2D-XRD pattern became large (Fig. 1.22b). Diffraction peaks of (220), (311) and (400) in ringwoodite were clearly observed in the D-DIA experiments with 50 keV monochromatic X-ray when using cBN anvil for X-ray window (Fig. 1.22). The diffraction peak of (400) could not be observed when using a conically slotted anvil for X-ray window, and not used for the estimate of pressure and differential stress. In the case of wadsleyite, diffraction peaks of wadsleyite (112), (114) and (240) were clearly observed and used for the analysis.

In the case of the D-111 apparatus, we used two rectangularly and conically slotted anvils with monochromatic X-ray of 60 keV. A whole Debye ring (Fig. 1.23) was observed, in which diffraction peaks of (220), (311), and (400) in ringwoodite were

observed. However, the diffraction peaks of MgO, which is used for the X-ray window, were very strong, and therefore the diffraction peak of ringwoodite (220) became very weak especially at high pressures. Therefore, peaks of (311) and (400) in ringwoodite were used for the analysis.

Variations of d-spacing with azimuth angles are obtained from the 2D-XRD pattern, and analyzed by the strain equation proposed by Singh (1993) and Singh et al. (1998) to estimate pressure and differential stress. We used softwares of IPanalyzer and PDindexer developed by Dr. Seto for these analyses.

The strain equation was briefly described below. The stress tensor in the deformation stage is given by

$$\sigma_{ij} = \begin{pmatrix} \sigma_{11} & 0 & 0 \\ 0 & \sigma_{22} & 0 \\ 0 & 0 & \sigma_{33} \end{pmatrix} = \begin{pmatrix} \sigma_p & 0 & 0 \\ 0 & \sigma_p & 0 \\ 0 & 0 & \sigma_p \end{pmatrix} + \begin{pmatrix} {}^{2t}/_{3} & 0 & 0 \\ 0 & {}^{-t}/_{3} & 0 \\ 0 & 0 & {}^{-t}/_{3} \end{pmatrix} \quad (1.3)$$

, where σ_p is the stress in hydrostatic pressure, t is the differential stress. The σ_{22} and σ_{33} is the same value in this study, so the σ_p and t can be described below.

$$\sigma_p = \frac{\sigma_{11} + 2\sigma_{33}}{3} \quad (1.4)$$

$$t = \sigma_{11} - \sigma_{33} \quad (1.5)$$

The relationship between the differential stress and d-value is described by the strain equation as follows:

$$d_m(hkl) = d_p(\text{hkl})[1 + (1 - 3cos^2\chi)Q(hkl)] \quad (1.6)$$

, where $d_p(hkl)$ is the d-spacing in hydrostatic pressure, $d_m(hkl)$ is the measured d-spacing in the deformation stage. The angle χ is given by

$$cos\chi = cos\theta \times cos(\varphi - \varphi_{\max}) \quad (1.7)$$

, where θ is the diffraction angle and φ is the azimuth angle. The $\varphi_{\max}$ is the azimuth angle when the d_m (hkl) is the maximum value. Q(hkl) in equation (1.6) is given by

$$Q(hkl) = (^t/_3)\{\alpha[2G_R(hkl)]^{-1} + (1 - \alpha)(2G_v(hkl))^{-1}\} \quad (1.8)$$

, where $G_R(hkl)$ is the shear modulus in Reuss (iso-stress) condition, $G_V(hkl)$ is the shear modulus in Voigt (iso-strain) condition, α is the relative weight of the strains calculated under Reuss an Voigt conditions. In this study, the α value is assumed to be 1. G_R value will change by crystal system.

Wadsleyite is orthorhombic crystal, in which the G_R of wadsleyite is described as follows:

$$\begin{aligned}[2G_R(hkl)]^{-1} = \frac{1}{2}\{&-(S_{12} + S_{13} + S_{23}) + {l_1}^2(S_{23} - S_{11}) + {l_2}^2(S_{13} - S_{22}) \\ &+ {l_3}^2(S_{12} - S_{33}) \\ &+ 3\big[{l_1}^4 S_{11} + {l_2}^4 S_{22} + {l_3}^4 S_{33} + {l_1}^2{l_2}^2(2S_{12} + S_{66}) \\ &+ {l_2}^2{l_3}^2(2S_{23} + S_{44}) + {l_3}^2{l_1}^2(2S_{13} + S_{55})\big]\}\end{aligned}$$

$$l_1 = {hd(hkl)}/{a}$$

$$l_2 = {kd(hkl)}/{b}$$

$$l_3 = {ld(hkl)}/{c} \quad (1.9)$$

The S_{ij} value is calculated from the elastic constants (C_{ij}) for wadsleyite (Wang et al., 2014) ignoring the temperature effect.

On the other hand, the crystal system of ringwoodite is cubic, so the G_R of ringwoodite is described as follows.

$$[2G_R(hkl)]^{-1} = \left[S_{11} - S_{12} - 3(S_{11} - S_{12} - \frac{1}{2}S_{44})\Gamma(hkl)\right] \quad (1.10)$$

$$\Gamma(hkl) = {(h^2k^2 + k^2l^2 + l^2h^2)}\Big/{(h^2 + k^2 + l^2)^2} \quad (1.11)$$

The S_{ij} value is calculated from the elastic constants (C_{ij}) for ringwoodite reported by Shinogeikin and Bass (2001).

In this way, we fitted the data set of the measured d-values $d_m(hkl)$ as a function of the azimuth angle φ to the strain equation (eq. 1.6) to optimize the *d*-value in hydrostatic pressure $d_p(hkl)$, and the differential stress *t*. The $d_p(hkl)$ values are used to estimate hydrostatic pressure of wadsleyite and ringwoodite using the equation of state of each phase (Wd: Fei et al., 1992, Rw: Nishihara et al., 2004).

The sample strain was calculated from the sample length which was measured from the distance between the Au foils in X-ray radiography image (Fig. 1.24). Fig. 1.24a shows X-ray radiography images in deformation experiments using D-DIA

apparatus at BL04B1 beamline of SPring-8, in which strain markers are clearly observed. In contrast, the radiography image was not clear in the case of the experiment using D-111 at NE-7 of Photon Factory mainly because the distance between camera and sample is large (Fig. 1.24b). The sample strain ε and the strain rate $\dot{\varepsilon}$ are calculated from the equations below.

$$\varepsilon = \frac{l - l_0}{l_0} \tag{1.12}$$

$$\dot{\varepsilon} = {}^{\varepsilon}/_{t} \tag{1.13}$$

, where l_0 is the initial length of the sample, l is the sample length, and t is time

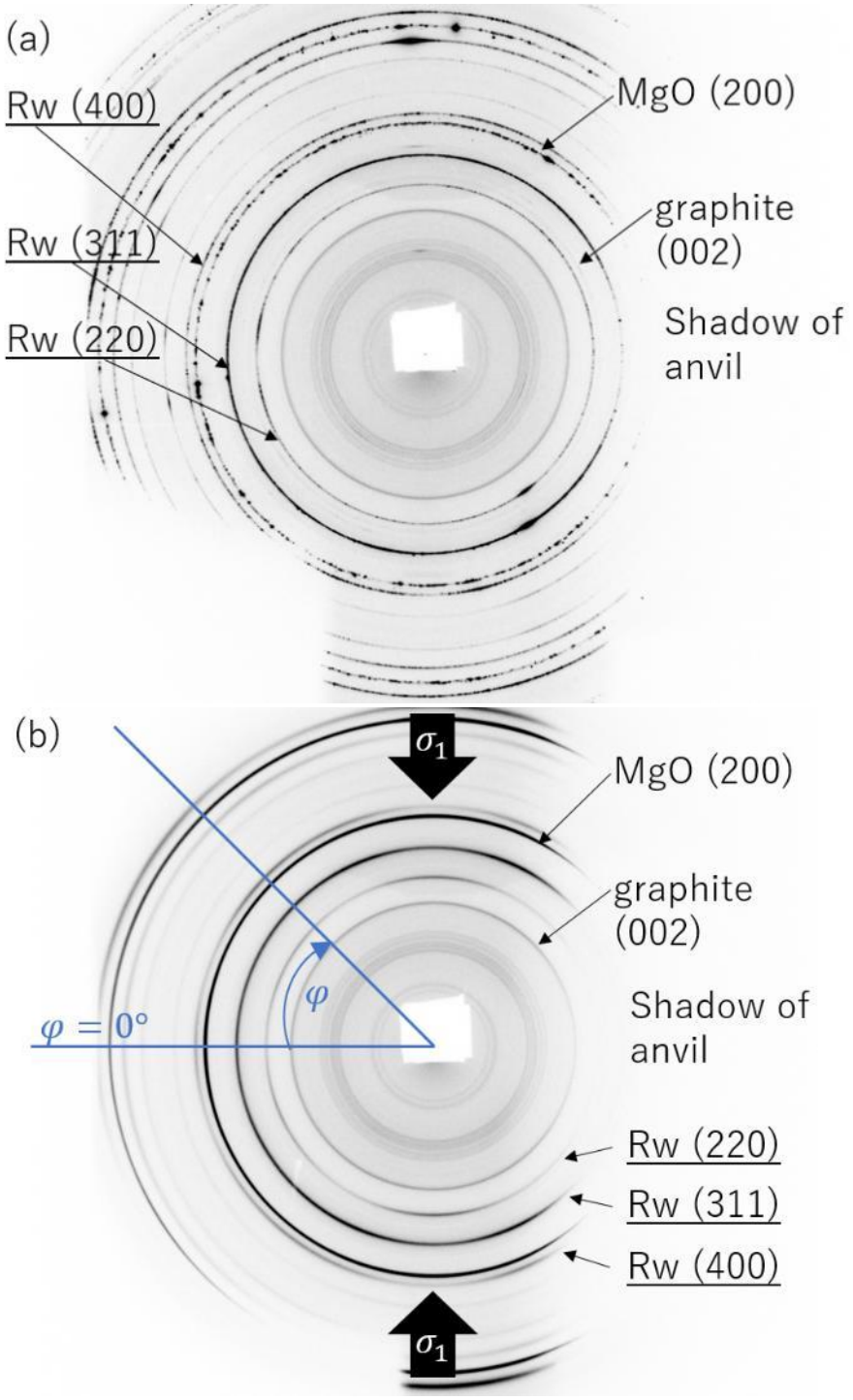

Fig. 1.22 2D-XRD patterns at ambient condition (a) and during deformation at high pressure (b) (Run rwdefp31). This experiment was performed using D-DIA apparatus at BL04B1 beamline of SPring-8. σ_1 direction is indicated by bold arrows in (b).

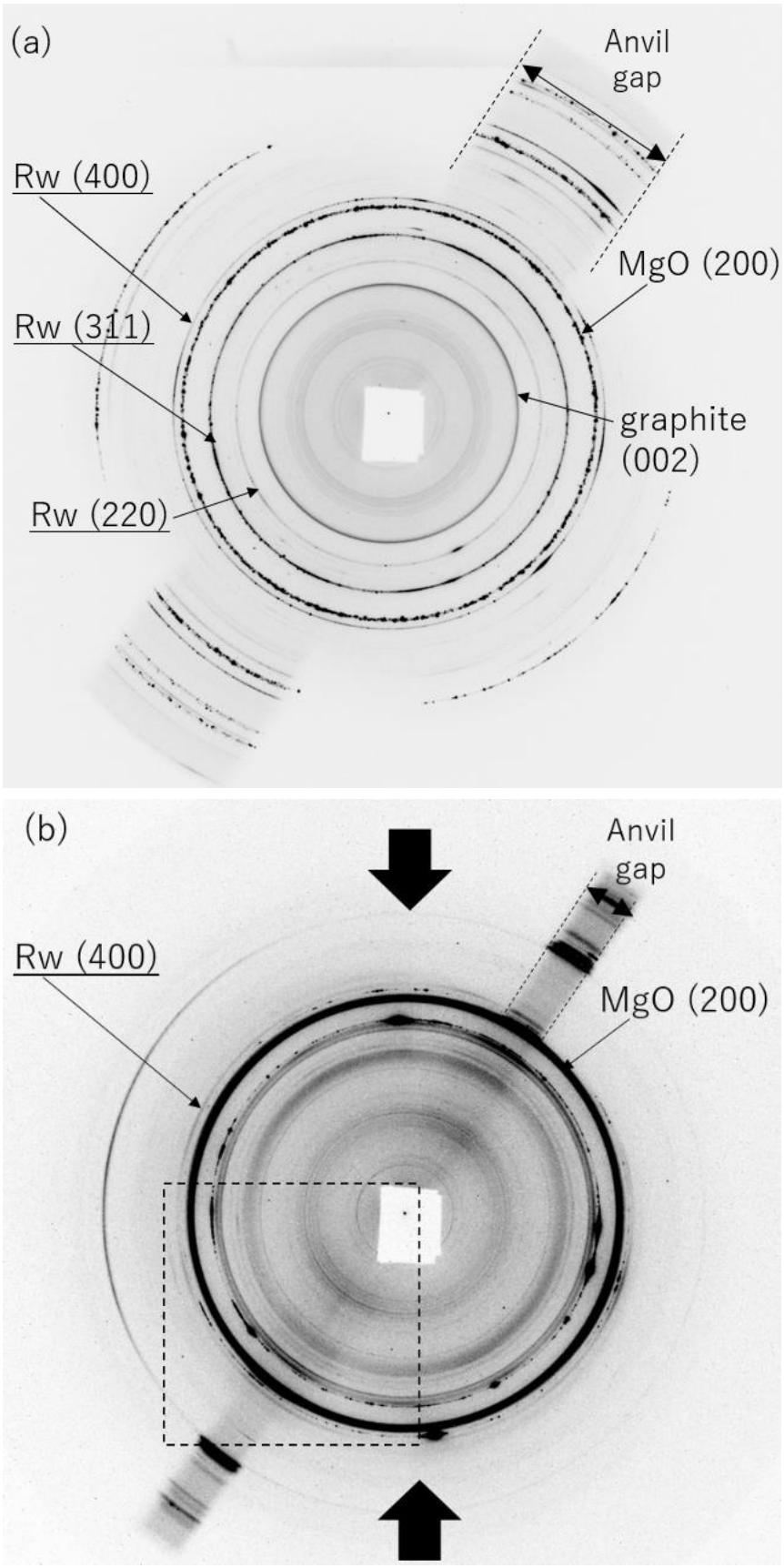
(a)
Anvil
gap
Rw (400)
MgO (200)
Rw (311)
graphite
(002)
Rw (220)
(b)
Anvil
gap
Rw (400)
MgO (200)

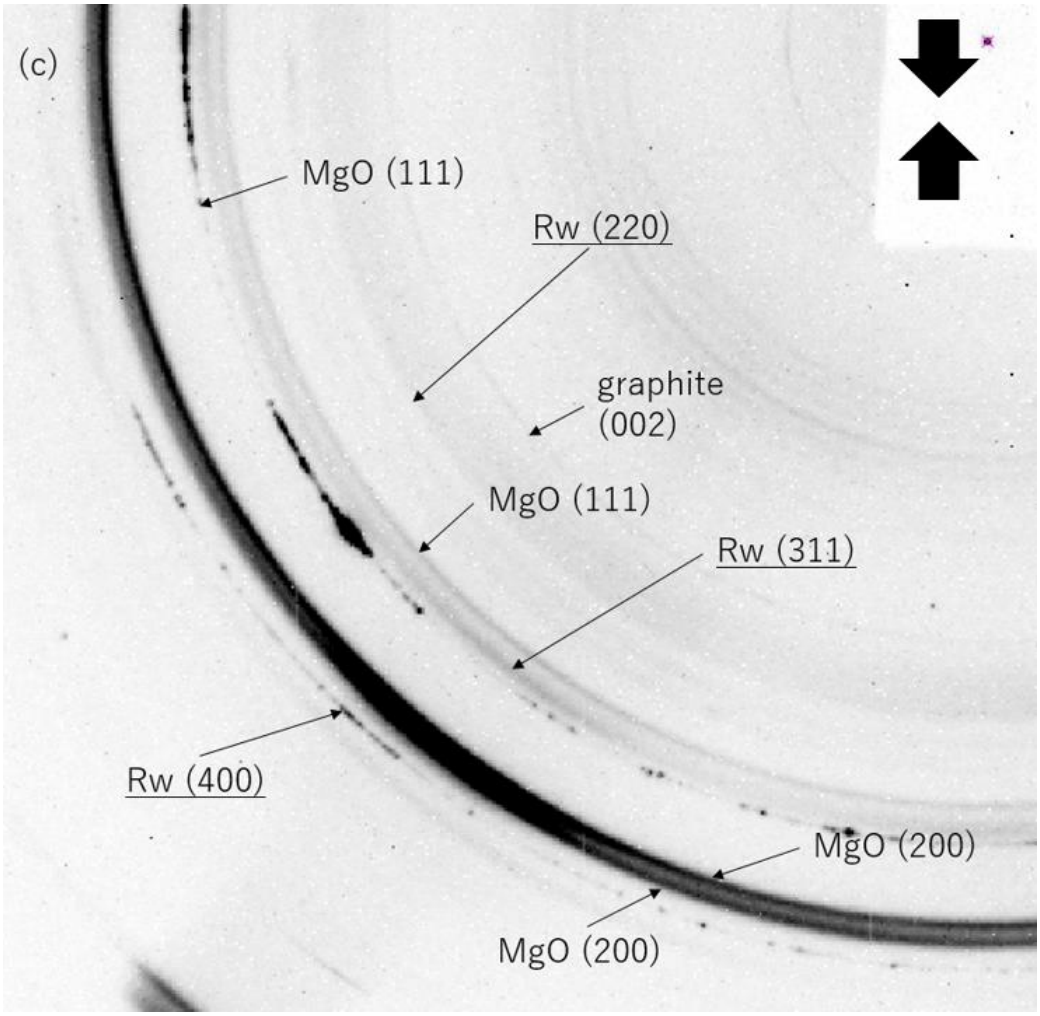

Fig. 1.23 2D-XRD patterns at ambient condition (a) and during deformation at high pressure (b, c) using D-111 apparatus at NE7 beamline of PFAR. (c) is a magnified image of the square area in (b). σ_1 direction is indicated by bold arrows in (b) and (c).

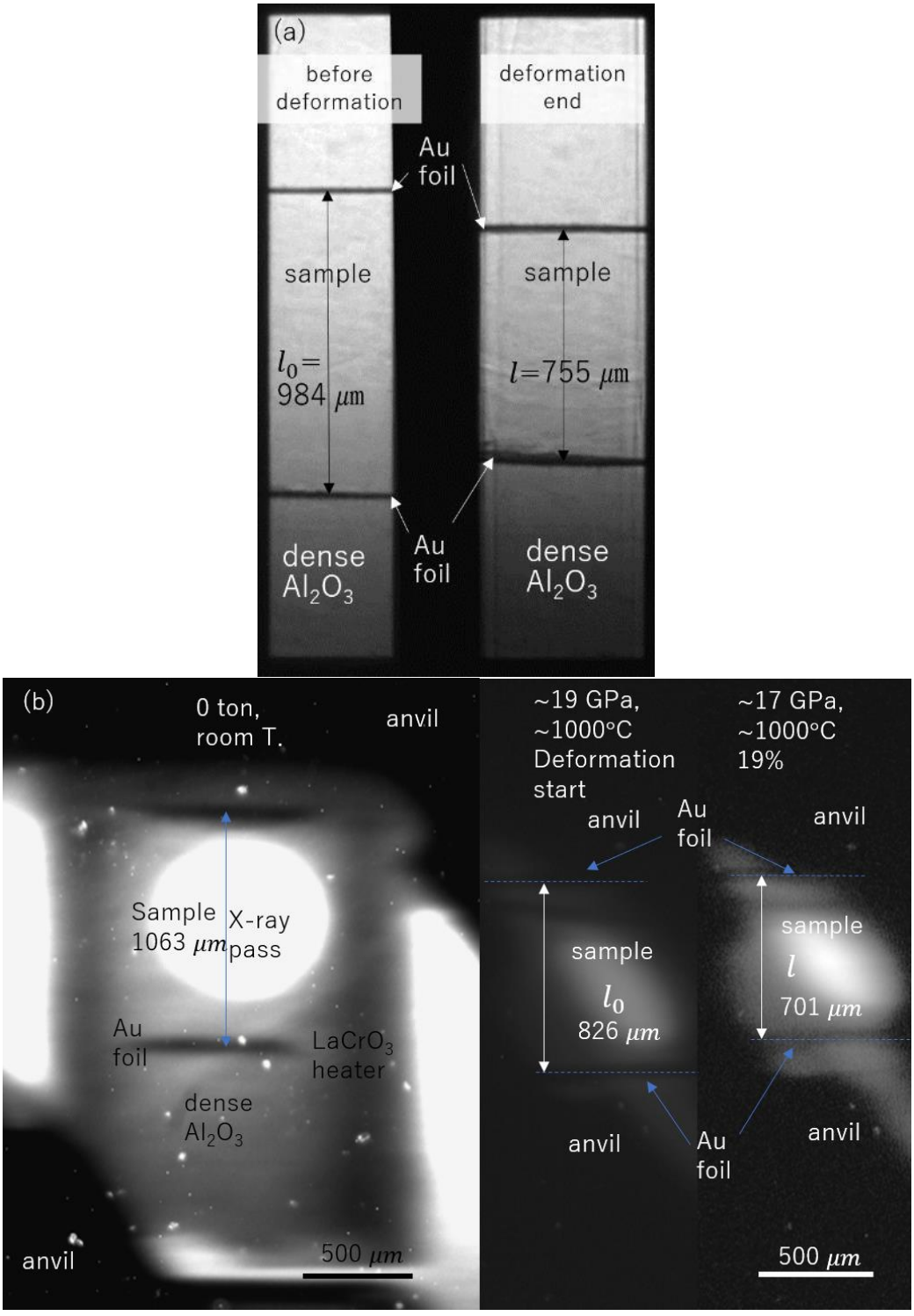

Fig. 1.24 Radiography images of samples observed during deformation at high pressures in D-DIA apparatus at BL04B1 beamline of SPring-8 (a) and D-111 apparatus at NE-7 beamline of PFAR (b).

1.2.4. Analysis of recovered samples

The recovered samples were cut into two fractions. One of them was used for the water content measurements. Another part was polished into thin section using a diamond paste to examine the deformation microstructures.

Infrared spectra of recovered samples were measured using micro FT-IR spectrometer (FT/IR-4100 and IRT-3000, JASCO Co., Ltd.). The water contents were estimated based on the calibration (Paterson, 1982) as follows:

$$C_{OH} = \frac{X}{150\zeta} \int \frac{K(\upsilon)}{(3780 - \upsilon)}\, d\upsilon \qquad (1.14)$$

, where C_{OH} is the molar concentration of hydroxyl, ζ is an orientation factor which is 1/3, υ is the wavenumber, $K(\upsilon)$ is the absorption coefficient, X is an average density factor (Bolfan-Casanova et al., 2000).

We observed grain-growth microstructure using FE-SEM (JSM-7001F, JEOL Co., Ltd.) installed at Kyushu University. The analytical condition was 0.50-5.00 nA probe current, 10-15 kV accelerating voltage and 10.0 mm working distance.

1.3. Results

1.3.1. Deformation experiments using slotted anvils as X-ray window

Slotted WC anvils or cBN anvils were used at the downstream side of the sample assembly to observe 2D-XRD patterns (Fig. 1.9). To generate higher pressure, several types of slotted WC anvils were tested for D-DIA experiments. Table 1.1 summarizes the types of the slotted anvil and experimental results. When WC anvils conically slotted by 11 degrees and filled up with Petropoxy (Petropoxy 154; Maruto Co. Ltd.) (Fig. 1.11b) were used, blowouts frequently happened during cold compression and deformation stages. Next, we tried the tungsten carbide anvils cut by rectangular slots in 1.40 mm width and 0.65 mm depth, and conically slotted by 6 degrees and filled up with Araldite (Fig. 1.11c). This type of slotted anvils was used in the previous study for Kawai-type multi-anvil apparatus (Dobson et al., 2012). However, blowouts easily occur during cold compression. It is thought that these frequent blowouts occurred because the slotted volume was large.

To avoid the blowout, WC anvils conically slotted by 6 degrees and filled up with the Araldite were finally used (Fig. 1.11a). In this case, we successfully conducted the deformation experiments at about 10 GPa (75 tons) and 700°C with the total strain of ~25% using anvils with a TEL of 4.0 mm. However, the blowouts occurred again

using anvils with a TEL of 2.5 mm and 3.0 mm to generate higher pressure. We also tried the anvils conically slotted by 5 degrees with a TEL of 2.5 mm, but it failed. Therefore, we used D-111 type deformation apparatus for higher-pressure deformation experiments than about 10 GPa.

Table 1.1 Types of slotted anvils and experimental results

Run No.	Anvil size (mm)	TEL (mm)	Window		Load (ton)	Temp. (°C)	strain (%)	Blowout
			D-DIA apparatus					
e.g. rwdefp32	12	4	cBN		75	200-540	~25	No
rwdefs11	18	4	11° cone	petropoxy	100	450*	3	Yes
rwdefs33	18	4	slot+6° cone	araldite	100	270*	-	Yes
rwdefs34	18	4	slot+6° cone	araldite	60	-	-	Yes
rwdefs42	18	4	6° cone	araldite	75	700	-	Yes
rwdefp44	18	4	6° cone	araldite	75	700	19	No
rwdefs21	18	3	11° cone	petropoxy	75	450*	-	Yes
rwdefs31	18	3	slot+6° cone	araldite	60	-	-	Yes
rwdefs43	18	3	6° cone	araldite	75	180	5	Yes
rwdefs75	18	2.5	5° cone	araldite	30	-	-	Yes
rwdefs61	18	2.5	12 mm cBN anvil	araldite	60	700	18	No
			D-111 apparatus					
rwdefp81	26	2	slot+6° cone	araldite	176	1000	19	No

*: Temperature was calculated from electric power.

1.3.2. Experimental conditions and back transformation

Deformation experiments with synchrotron X-ray were conducted at ~6.6-17.5 GPa and 200-1000°C with a constant strain rate (0.96-9.1$\times 10^{-5}\ s^{-1}$) (Table 1.2, Fig. 1.25). We used D-DIA and D-111 type apparatus to construct the flow law of ringwoodite and wadsleyite under low-temperature conditions. In the case of D-DIA deformation experiments, we measured creep data at one condition in one run (single-step experiments), or at two conditions in one run (two-step experiments) to collect creep data effectively. In the latter case, we changed the temperature or the strain rate condition at about 10 % strain. The D-111 apparatus was used to measure the creep data at the higher pressure condition.

The creep data of ringwoodite was obtained less than 700°C at about 10 GPa because the back transformation from ringwoodite to olivine occurred at this temperature (Run rwdefs51, a in Fig. 1.25 and Fig. 1.26). To avoid the back transformation, we conducted the deformation experiments at around ~ 14 GPa with a TEL of 2.5 mm, however the back transformation from ringwoodite to wadsleyite was observed at 800°C (Run rwdefs62, b in Fig. 1.25). On the other hand, the back transformation from wadsleyite to olivine occurred at about 9 GPa and 700°C (Run wddefs21, c in Fig. 1.25). Thus, we could collect creep data of wadsleyite and ringwoodite up to 700°C outside their stability fields.

In order to obtain creep data of ringwoodite at higher temperature of 1000°C, we conducted a deformation experiment of ringwoodite in its stability field at ~18 GPa by using D-111 apparatus (Run rwdefp81, d in Fig. 1.25)

Table 1.2 Experimental condition and results

Run No.	Deformation apparatus	Anvil size (mm)	TEL (mm)	window	Step	Load (ton)	Pressure at ~10% strain (GPa)	Pressure at ~15% strain (GPa)	Temp. (°C)	Strain rate ($\times10^{-5}$) (s^{-1})	Total strain (%)	Stress at ~10% strain (GPa)	Stress at ~15% strain (GPa)	Water content (wt. ppm H_2O)
Ringwoodite deformation														
rwdefs41	D-DIA	18	4.0	6° cone	1	75	-		200	2.5	7	-		
							10.9 (0.4)	11.0 (0.4)	200	6.3	23	3.8 (0.6)	3.6 (0.6)	
rwdefp32	D-DIA	12	4.0	cBN	1	75	-		270*	1.1	8	-		1860 (195)
					2		14.4 (0.3)	14.6 (0.3)	270*	7.8	23	4.1 (0.2)	3.9 (0.2)	
rwdefp21	D-DIA	12	4.0	cBN	1	50	-		450*	1.2	6	-		1004 (258)
					2		8.7 (0.4)	8.7 (0.4)	450*	5.9	22	4.4 (0.6)	4.4 (0.6)	
rwdefp12	D-DIA	12	4.0	cBN	1	75	12.4 (0.2)		450*	2.5	12	3.7 (0.5)		
					2		-		450*	4.5	17	-		
rwdefs32	D-DIA	12	4.0	cBN	1	75	-		450*	1.9	7	-		855 (82)
					2		12.4 (0.1)	12.2 (0.2)	450*	5.2	21	4.8 (0.1)	3.6 (0.6)	
rwdefp33	D-DIA	12	4.0	cBN	1	75	-		540*	0.96	8	-		
					2		12.6 (0.2)	12.7 (0.3)	540*	9.1	23	4.4 (0.3)	4.2 (0.3)	
rwdefp44	D-DIA	18	4.0	6° cone	1	75	10.3 (0.2)	10.2 (0.2)	700	3.3	19	2.9 (0.5)	3.9 (0.6)	1062 (90)
rwdefs51	D-DIA	12	4.0	cBN	1	75	~9-11		700		Back transformation to olivine			
rwdefs61	D-DIA	18	2.5	cBN	1	60	14.1 (0.2)	13.8 (0.3)	700	4.3	19	2.5 (0.2)	2.6 (0.3)	204 (22)
rwdefs62	D-DIA	18	2.5	cBN	1	60	~13-15		800		Back transformation to wadsleyite			
rwdefp81	D-111	26	2.0	Slot+ 6° cone	1	176	17.5 (0.4)	17.0 (1.3)	1000	3	19	1.4 (0.2)	1.5 (0.3)	230 (136)
Wadsleyite deformation														
wddefs13	D-DIA	12	4.0	cBN	1	75	10.4 (0.1)		300	4.3	17	2.1 (1.0)		
wddefs22	D-DIA	18	4.0	6° cone	1	75	8.6 (0.1)	8.5 (0.2)	400	5.3	17	2.0 (0.9)	2.1 (1.0)	
wddefs11	D-DIA	12	4.0	cBN	1	75	8.8 (0.1)		500	4.6	15	1.9 (0.5)		232 (51)
wddefs21	D-DIA	12	4.0	cBN	1	75	~8-10		700		Back transformation to olivine			

*: Temperature was calculated from the electric power.

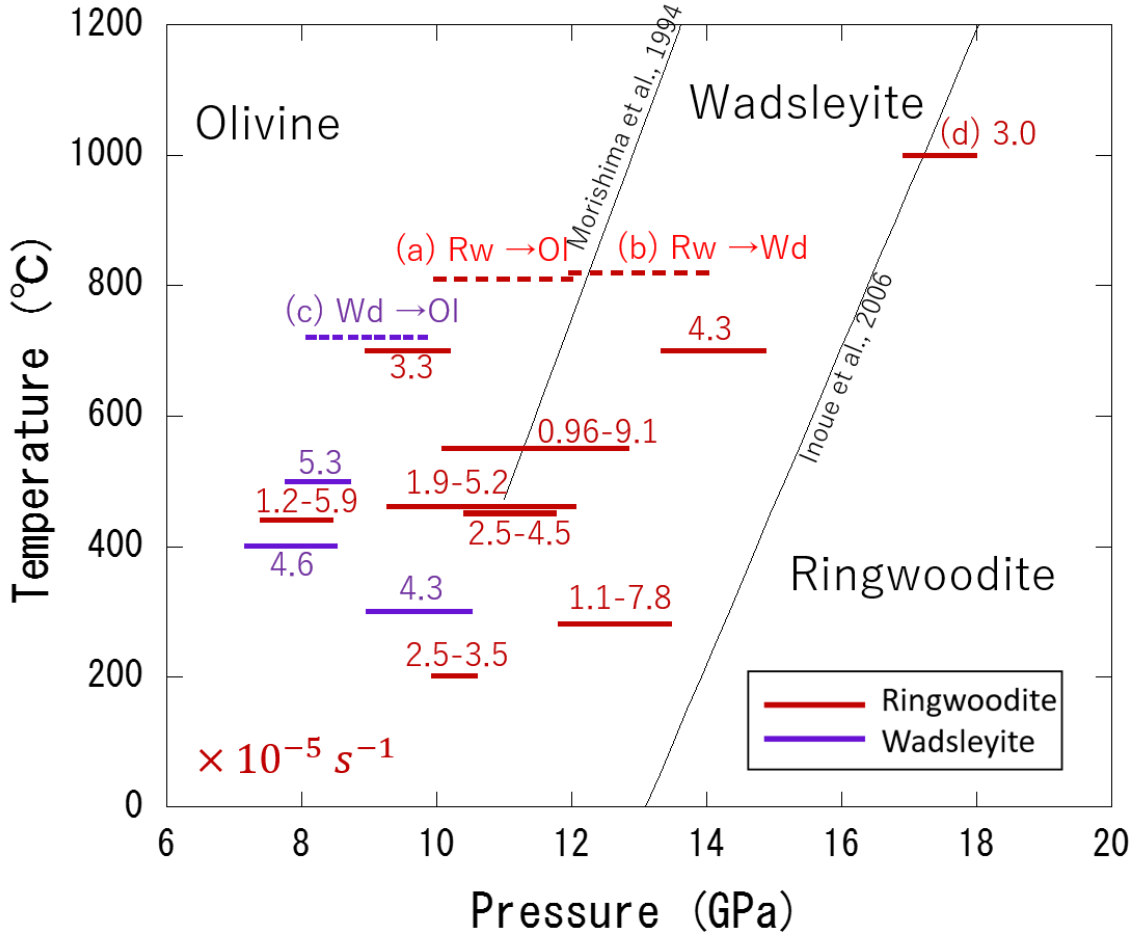

Fig. 1.25 Experimental conditions in our study (purple: wadsleyite, red: ringwoodite) and the phase boundary of olivine-wadsleyite and wadsleyite-ringwoodite transformations (Morishima et al., 1994; Inoue et al., 2006). Most of the deformation experiments were conducted at less than 700°C to avoid the back transformation (solid lines). The back transformation occurred at 700-800°C outside the stability field (dashed line; (a) ringwoodite to olivine, (b) ringwoodite to wadsleyite, (c) wadsleyite to olivine). A deformation experiment of ringwoodite was performed in the stability field of ringwoodite by using D-111 apparatus (d).

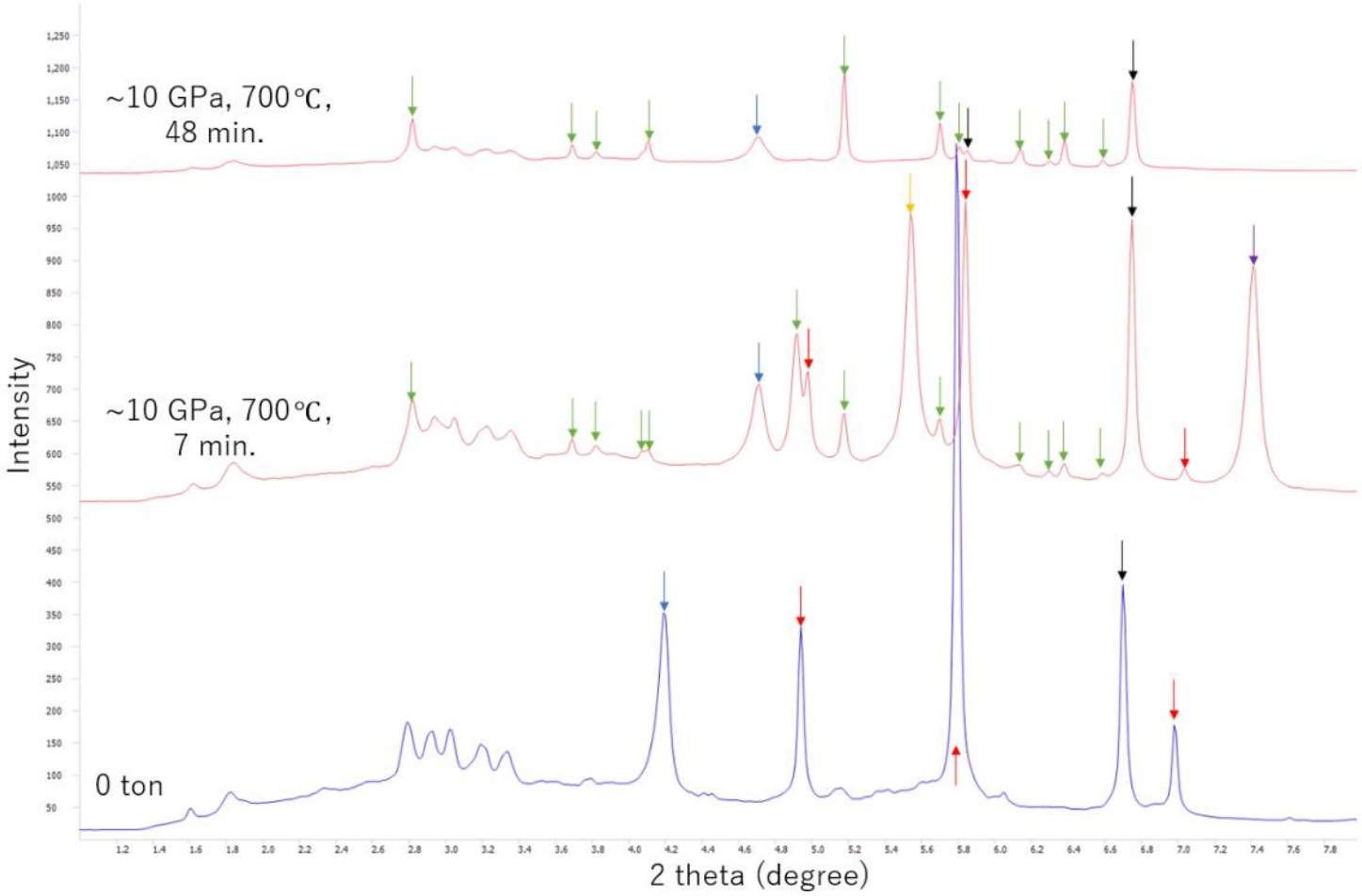

Fig. 1.26 Changes of 1D-XRD patterns during the back transformation from ringwoodite to olivine at about 10 GPa and 700°C (Run rwdefs51, blue: graphite, red: ringwoodite, black: MgO).

1.3.3. Deformation microstructures and water contents

Microstructures of the starting ringwoodite and those after the deformation experiment were shown in Fig. 1.6 and Fig. 1.27, respectively. These images suggest that the grain size does not change during deformation. Ringwoodite grains in the recovered samples from the deformation experiments is flatly deformed perpendicular to the σ_1-axis. These microstructures were different from those of the previous study deformed at 1027-1427°C (Kawazoe et al., 2016), in which the dynamic recrystallization was observed, suggesting that dislocation creep at higher temperatures. The microstructures observed in this study imply that Peierls mechanism was dominated at lower temperatures (200-1000°C).

It has been reported that, in the Peierls mechanism of olivine, the flow strength was smaller under wet condition (about 49.6-74.7 wt. ppm H_2O) than those obtained in dry conditions (Katayama and Karato, 2008). Therefore, it is necessary to measure the water contents of ringwoodite. IR spectra of recovered samples are shown in Fig. 1.28. The broad absorption peak was observed at ~ 3400 cm^{-1}. The water content of the starting ringwoodite is about 1420 $\pm$ 180 wt. ppm H_2O. Those of recovered samples were about 1900, 1000 and 200 ppm H_2O at 270, 450-700 and 1000°C, respectively (Table 1.2), suggesting that the water contents decreased with temperature.

Although the broad absorption peak of polycrystalline ringwoodite were also reported in previous studies, the peak position was different. In the study of Pearson et al. (2014), the broad absorption bands were observed at about 3150 cm^{-1} from natural ringwoodite in diamond. The water content was estimated to be about 1.5 wt. % H_2O. Similar broad absorption peak at ~3150 cm^{-1} was also observed in other previous studies for synthesized hydrous $(Mg, Fe)_2SiO_4$ ringwoodite (e.g., Bolfan-Casanova et al., 2003; 2113 wt. ppm H_2O), Jacobson et al., 2004; 9960 wt. ppm H_2O). On the other hand, in the study of Kawazoe et al. (2016) for ringwoodite with smaller amounts of water (~300-1000 wt. ppm H_2O), the broad absorption band was observed at ~ 3500 cm^{-1}. The water contents and the peak positions are both similar to those in this study. Thus, the difference in the peak position may be originated from the difference in the water content.

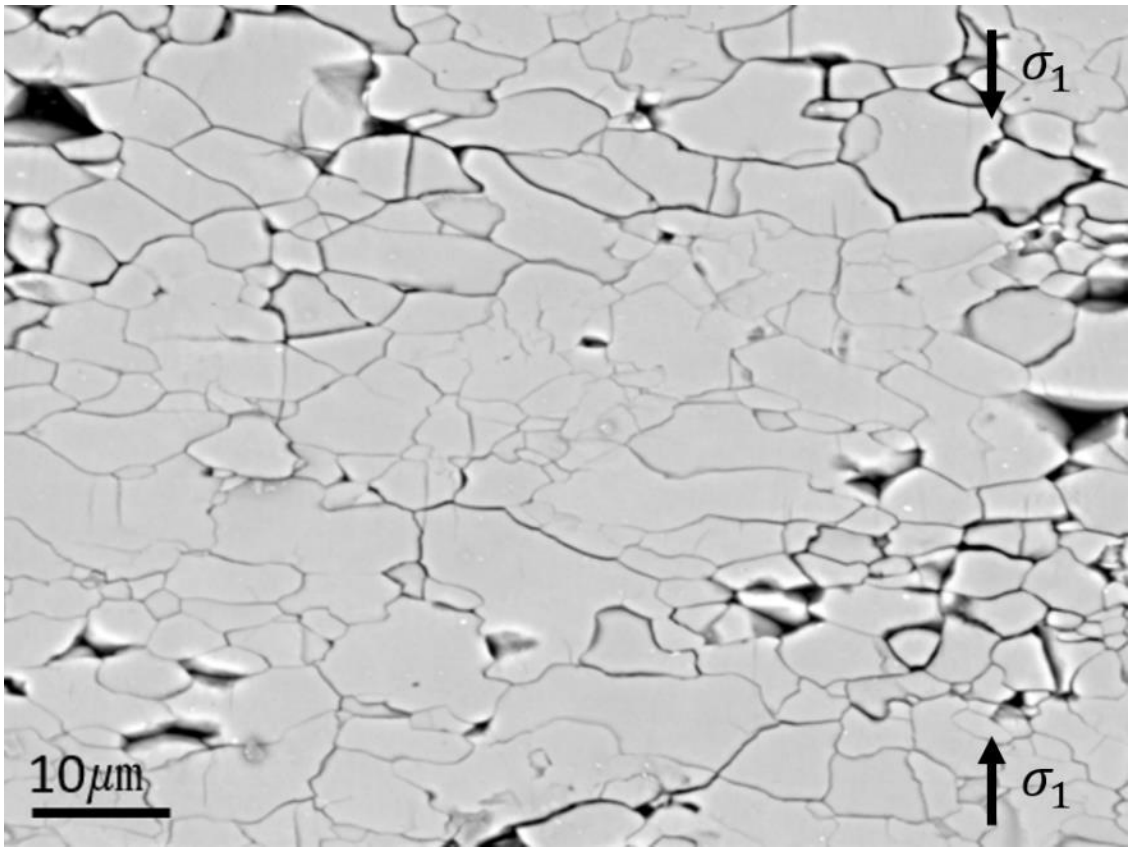

Fig. 1.27 Backscattered electron image of recovered samples (Run rwdefp31).

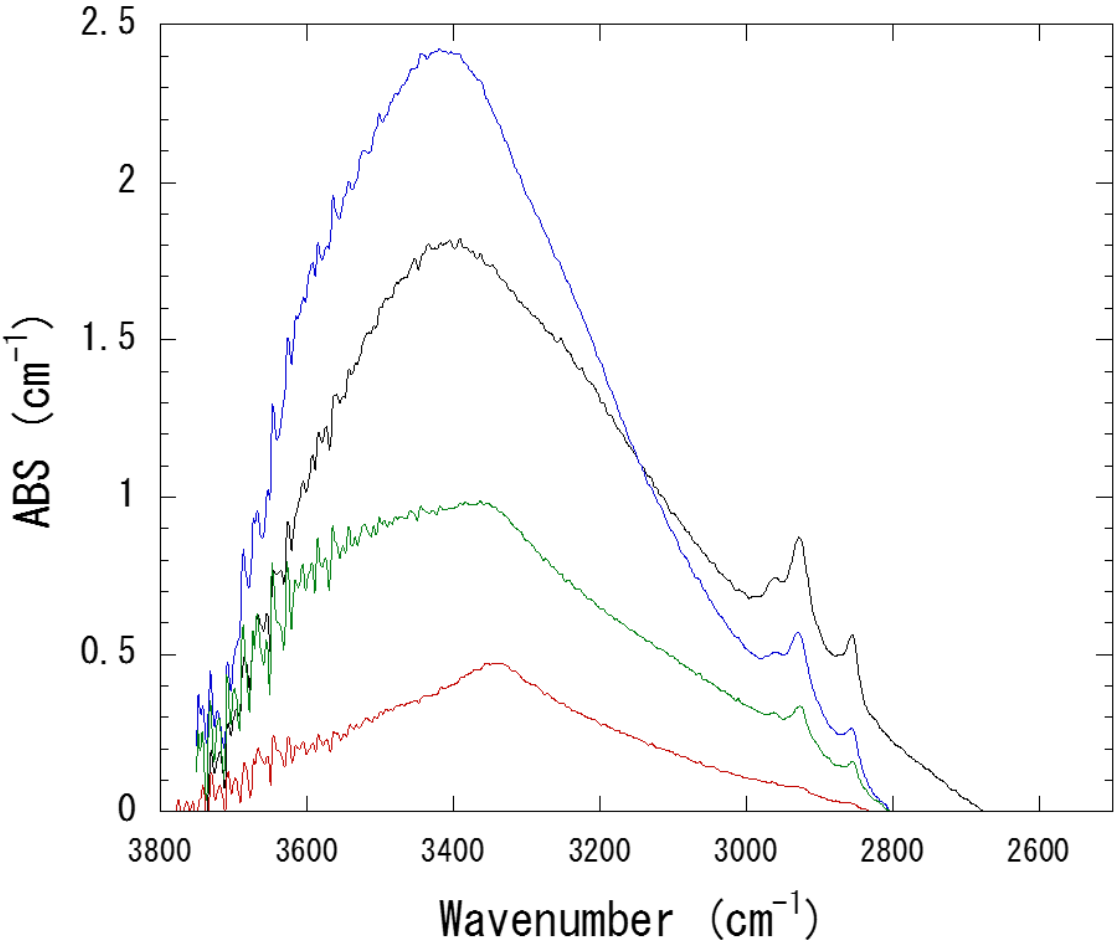

Fig. 1.28 IR spectra of polycrystalline ringwoodite (black: starting material, blue: Run rwdefp32 at 270°C, green: Run rwdefp21 at 450°C, red: Run rwdefp81 at 1000°C).

1.3.4. Mechanical data of wadsleyite and ringwoodite

Strain rate was calculated from the relationship between the strain and time (eq. 1.12 and 1.13, Fig. 1.29). Fig. 1.29 shows the sample strain with time in Runs of rwdefp32 and rwdefp81. In Run rwdefp81, the deformation experiments were performed at the constant displacement speed of 200 μm/h, resulting in almost constant strain rate of 3.0×10^{-5} s^{-1} (red line in Fig. 1.29). In Run rwdefp32, the anvil displacement rate changed from 100 μm/h (blue solid line in Fig. 1.29) to 400 μm/h (blue dashed line in Fig. 1.29), resulting in the change of the strain rate from 1.1×10^{-5} s^{-1} to 7.8×10^{-5}. As seen above, the deformation experiments were conducted at constant strain rates by keeping the anvil displacement rate constant (Table 1.2).

Pressure and differential stress were measured from the X-ray diffraction patterns. The pressure was roughly constant during the deformation stage (Fig. 1.30). The obtained 2D-XRD pattern was subdivided into 15 sectors with azimuth angle of 12° in D-DIA deformation experiments of ringwoodite. Fig. 1.31 shows the subdivided 1D-XRD patterns obtained in Run rwdefs32. We observed sharp diffraction in ringwoodite at ambient condition and the d-spacing is almost constant with azimuth angle (Fig. 1.31a). On the other hand, d-spacing takes the minimum value at $\varphi = \pm 90°$ in the σ_3 direction and the maximum value at $\varphi = 0°$ in the σ_1 direction (Fig. 1.31b).

These peaks became broad during the deformation stage at high pressure. These undulations of d-spacing in ringwoodite are shown in the plots of the d/d_p values against the azimuth angle in Fig. 1.32. The undulation was already present at high pressure and high temperature before the deformation stage. The stress value was estimated by the fitting of eq. 1.6 to the undulation data (Fig. 1.32).

It is known that the stress value varies with the lattice planes. In the case of ringwoodite, the differential stress from (220) is larger than those of (311) and (400) (Nishiyama et al., 2005, Kawazoe et al., 2016). The stress value in wadsleyite also changes with crystal planes (e.g., Kawazoe et al., 2011; Hustoft et al., 2013; Farla et al., 2015). D-DIA apparatus and a rotational Drickamer apparatus was used for the deformation experiments of wadsleyite in Kawazoe et al. (2011), and Hustoft et al. (2013) and Farla et al. (2015), respectively. The stress was calculated from (040), (141), (240), and (013) in the studies of Hustoft et al. (2013) and Farla et al. (2015), and (112), (013), (211), (132), (103), and (231) in Kawazoe et al. (2011). The differential stress calculated from (112) is larger than those of other crystal plane.

In this study, the differential stress was estimated from ringwoodite (220), (311), and (400), and from wadsleyite (112), (141), and (240). Examples of stress-strain curves in each crystal plane are shown in Fig. 1.33. These flow data suggest that the

flow stress is larger, and the strain hardening is more significant in ringwoodite compared to wadsleyite.

In the two-step deformation experiments, we change the anvil displacement rate at about 10 % strain to collect creep data efficiently. However, because of the strain hardening in ringwoodite, effects of temperature and strain rate on the flow stress were not clear (Fig. 1.34). The effects of temperature on the stress-strain curve in the single-step experiment of ringwoodite are shown in Fig. 1.35. The strain hardening continued over 20 % strain at relatively low temperatures (200-450°C), and finally disappeared at 700°C. We could not conduct the deformation experiments at higher temperature than 700°C using D-DIA apparatus because of the back transformation at low pressures outside the stability field.

One experiment was conducted at about 18 GPa and 1000°C by using D-111 apparatus to deform the ringwoodite in the stability field (d in Fig. 1.25). The subdivided 1D-XRD patterns of the sample are shown in Fig. 1.36. The diffraction peaks of ringwoodite were not clearly observed because the peak intensities in MgO were very strong (Fig. 1.23c). Because of this, the undulation of the ringwoodite (220) could not be measured (Fig. 1.36b), and the differential stress was calculated only from the ringwoodite (311) and (400) in this run. The plots of d/d_p values against azimuth

angle are shown in Fig. 1.37. The d-spacing was constant with the azimuth angle at ambient condition, however it became large at 90 and 270 degrees, and small at 0 and 180 degrees just after the cold compression stage, suggesting that tensional stress was generated in the sample. At the last part of the deformation stage, the undulation pattern showed compressional stress.

The stress-strain curves of the ringwoodite (311) and (400) are shown in Fig. 1.38b. The pressure was almost constant during the deformation (Fig. 1.38a). The tensional stress at the starting point changed to the compressional stress at about 5 % strain. The differential stress became the roughly constant from 8 % strain. Strain hardening was not significant at this temperature.

On the other hand, the deformation experiments of wadsleyite were conducted at 8-10 GPa and 300-500°C using D-DIA apparatus and WC anvils with a TEL of 4.0 mm (Table 1.2). Fig. 1.39 shows the subdivided 1D-XRD patterns into 10 sectors by 18 degrees. The pressure and differential stress were calculated using the diffraction peaks of wadsleyite (112), (141) and (240). The undulations of wadsleyite (112) along azimuth angle were shown in Fig. 1.39b. These undulations of d-spacing in wadsleyite are shown in the plots of the d/d_p values against the azimuth angle in Fig. 1.40. Relatively large differential stress was already present before the deformation (black line in Fig.

1.40). The pressure value was almost constant during the deformation stage (Fig. 1.41a). Fig. 1.41b shows stress-strain curves in wadsleyite. The strain hardening was not significant compared to the ringwoodite deformation. The deformation experiment at more than 700°C was difficult because of the back transformation to olivine (c in Fig. 1.25).

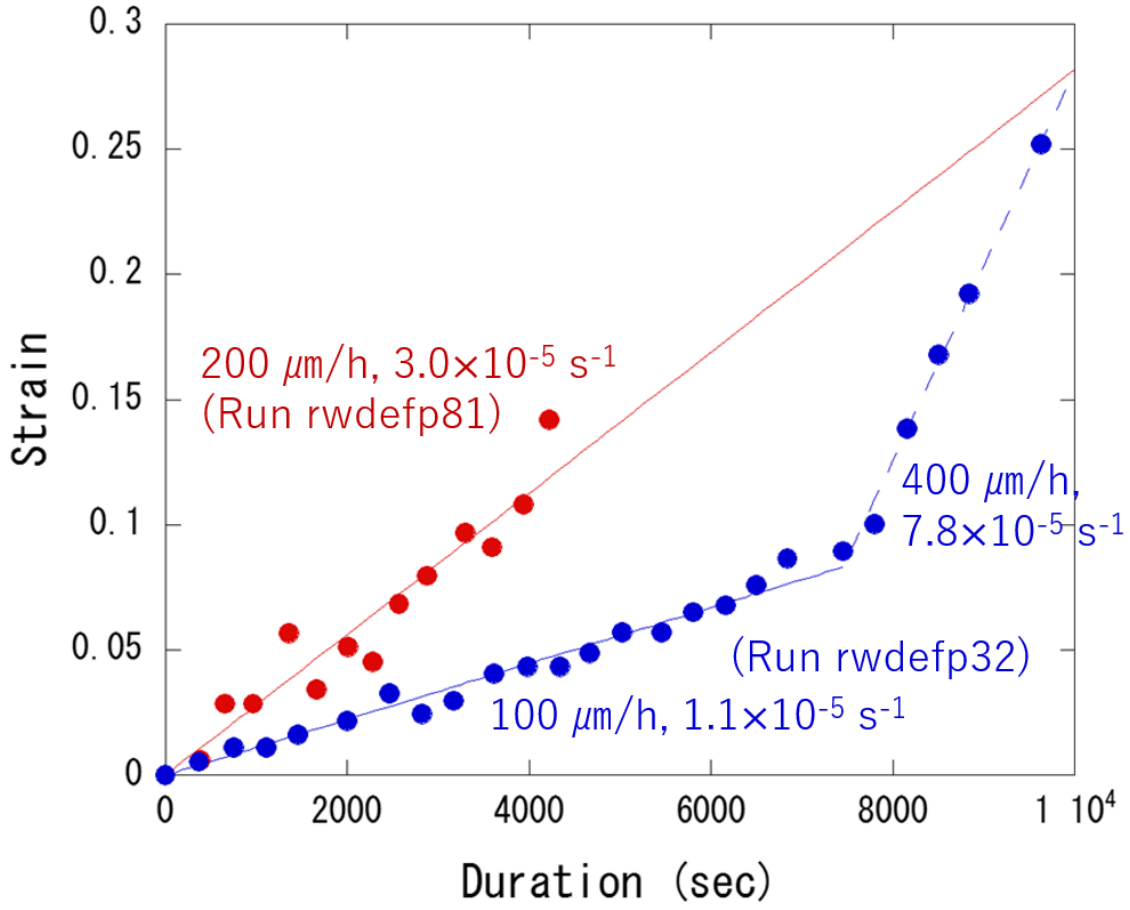

Fig. 1.29 Changes of the sample strain with time. The movement speed of the top and bottom anvils was constant at 200 μm/h (red: rwdefp81). In run rwdefp32 (blue), the anvil displacement speed was changed from 100 μm/h (solid line) to 400 μm/h (dashed line).

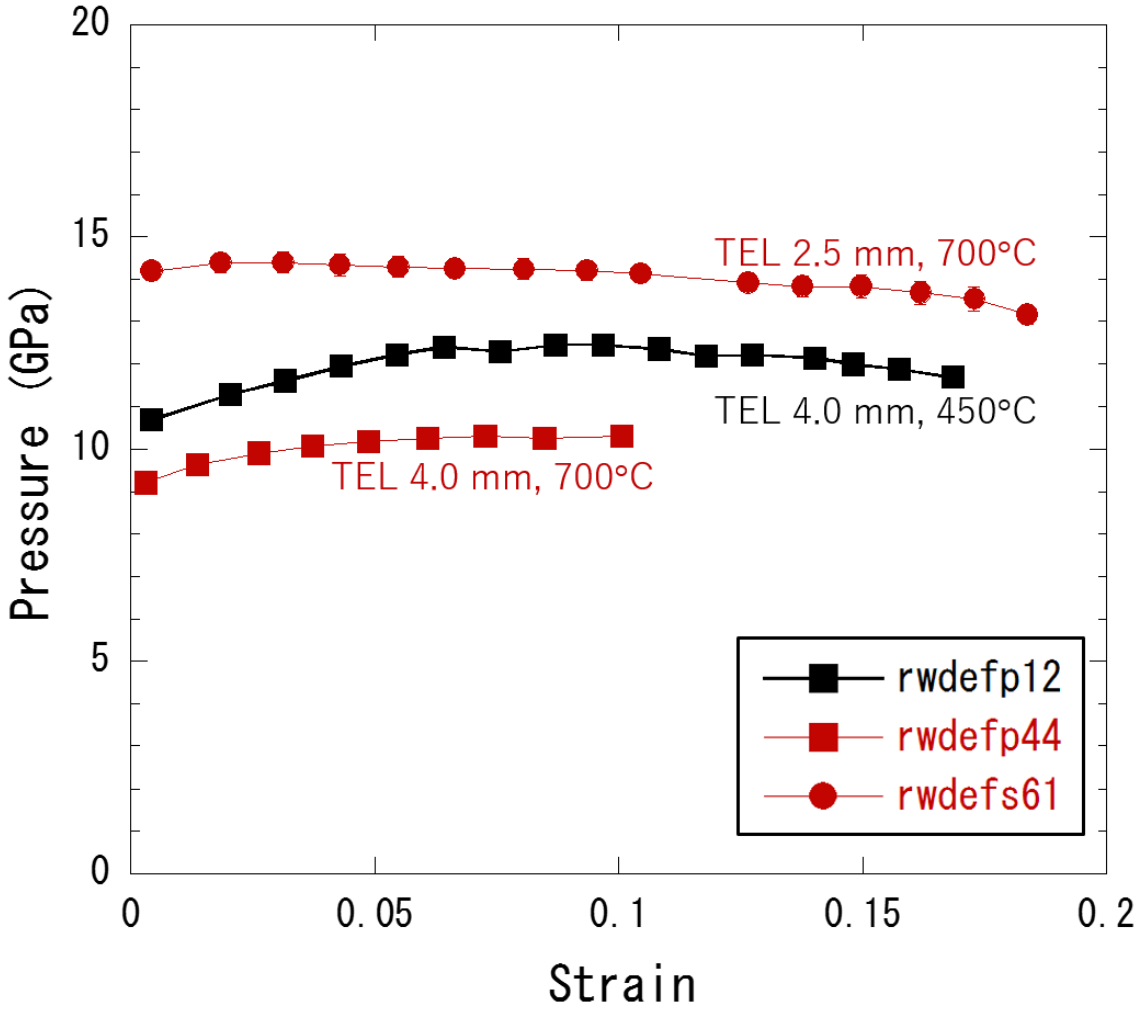

Fig. 1.30 Changes of pressure with sample strain.

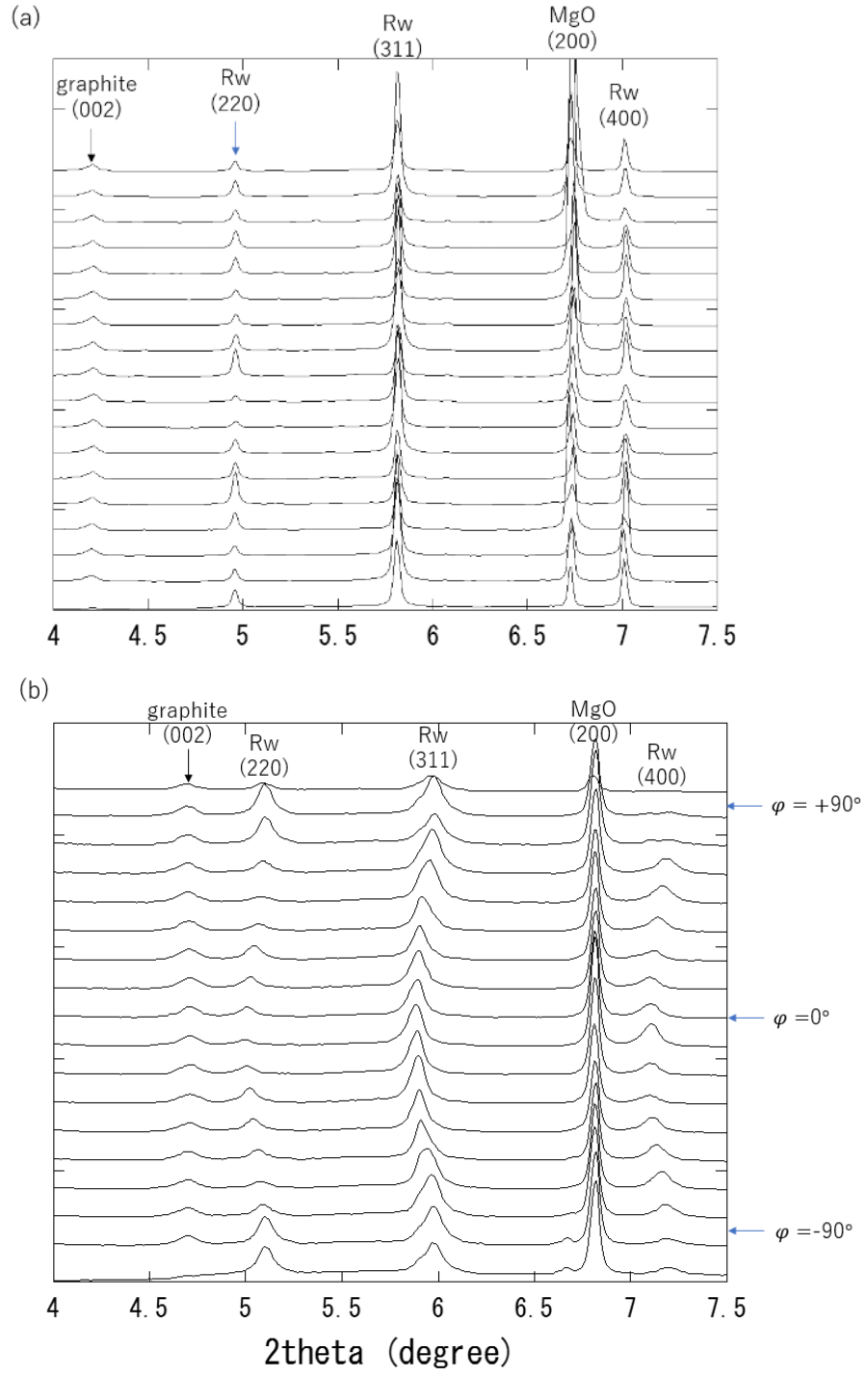

Fig. 1.31 1D-XRD patterns subdivided by 15 sectors from half circle of the 2D-XRD pattern at room temperature (Run rwdefs32). (a) ambient condition. (b) During deformation at 20% strain.

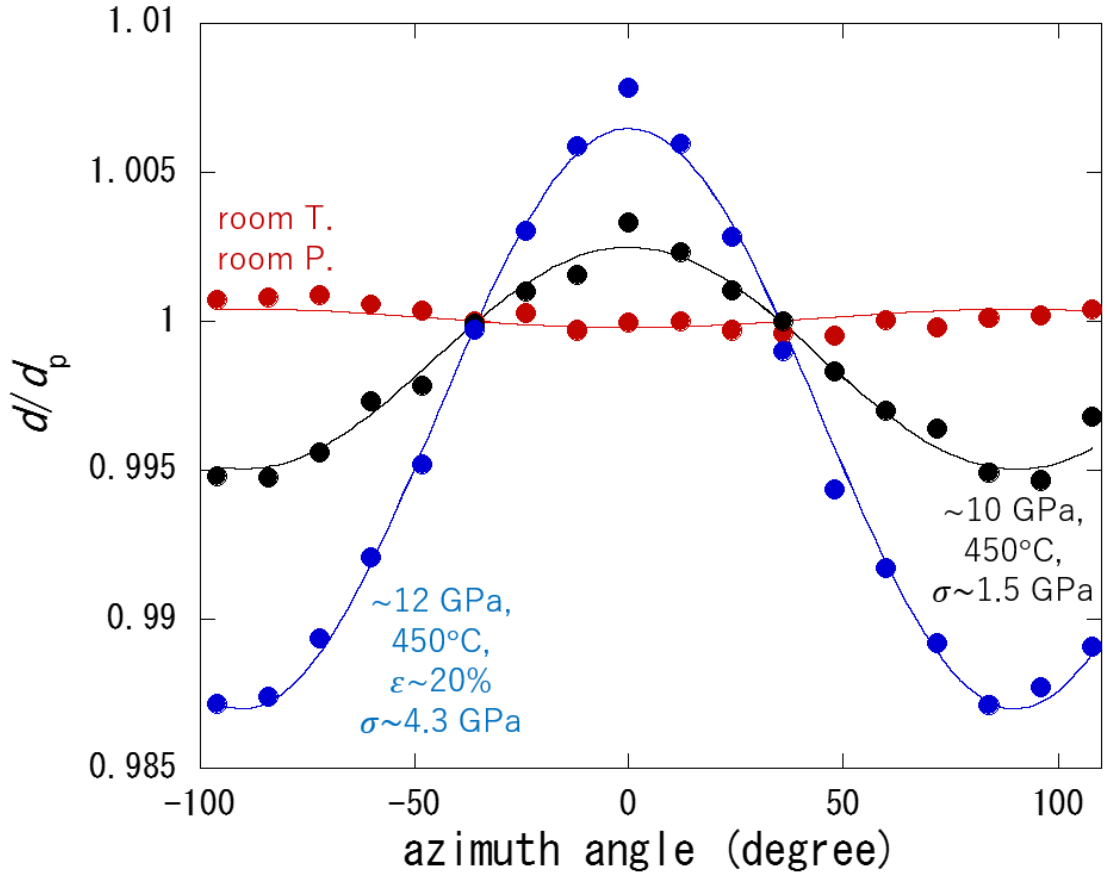

Fig. 1.32 Plots of d/d_p with azimuth angle (rwdefs32). The data was fitted by the strain equation (eq. 1.6). The estimated stress values are also shown.

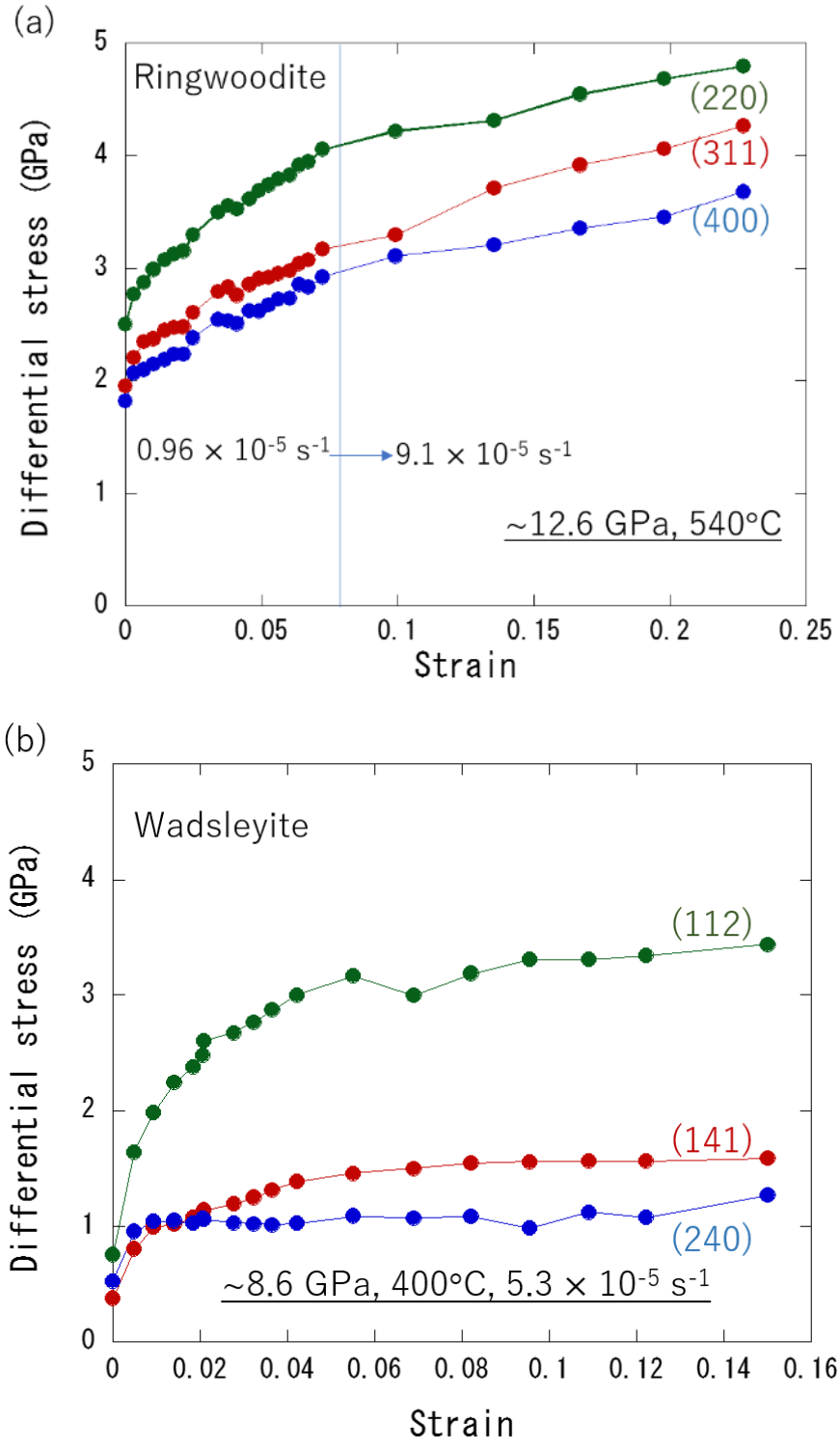

Fig. 1.33 Stress-strain curves in ringwoodite (a, Run rwdefp33) and wadsleyite (b, Run wddefs22) showing changes of differential stress with lattice planes.

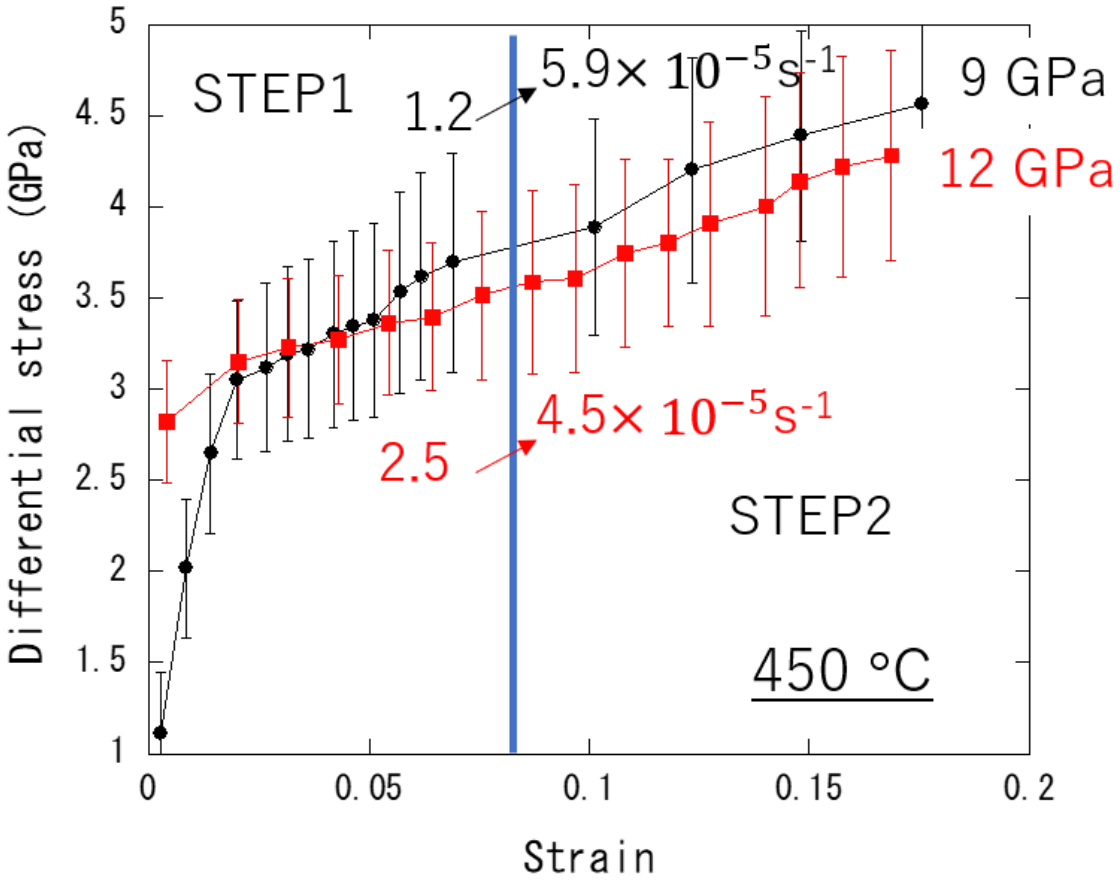

Fig. 1.34 Stress-strain curves of ringwoodite obtained in the two-step deformation experiments using the D-DIA apparatus.

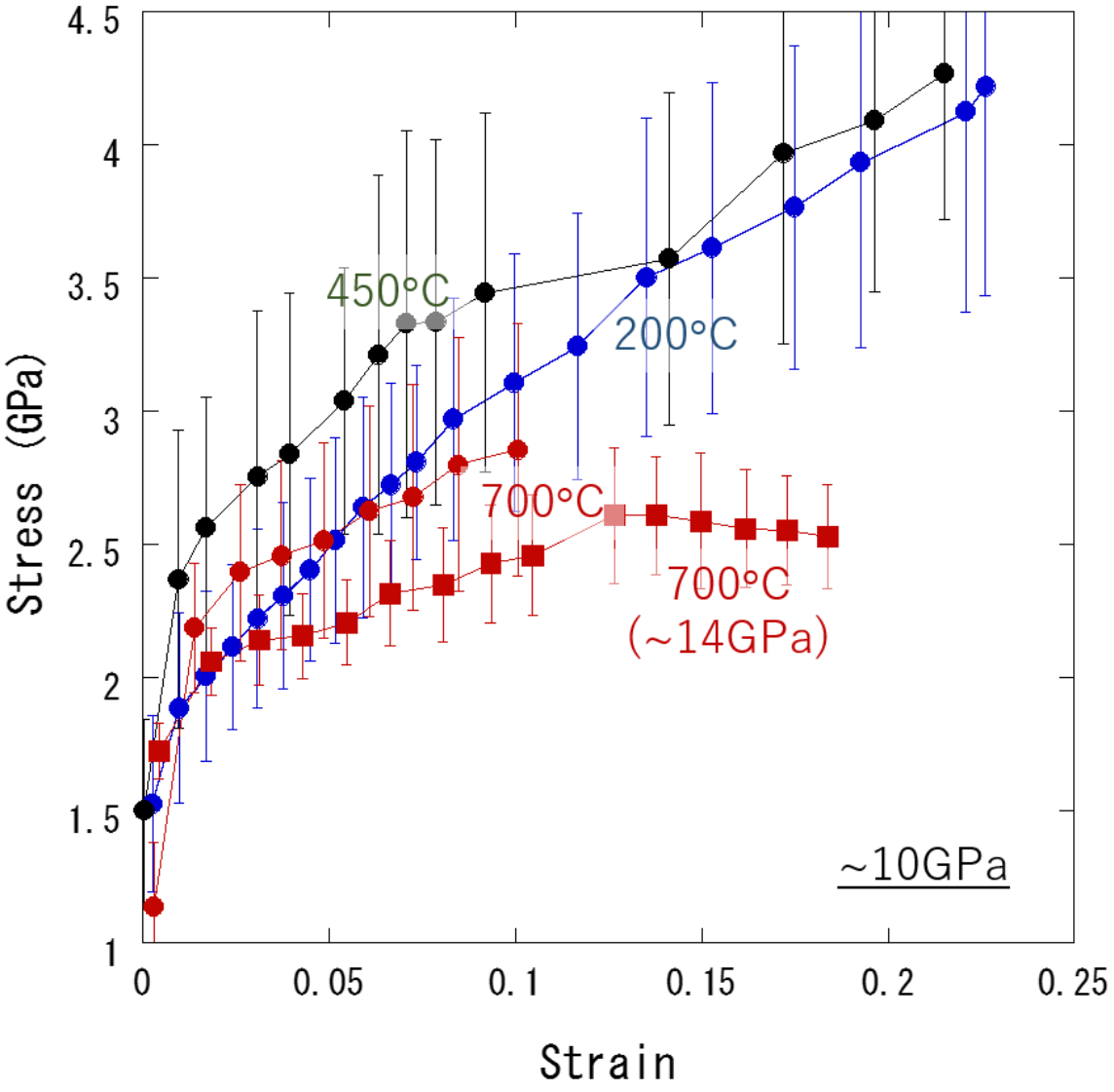

Fig. 1.35 Effects of temperature on the stress-strain curves in ringwoodite obtained from the D-DIA experiments.

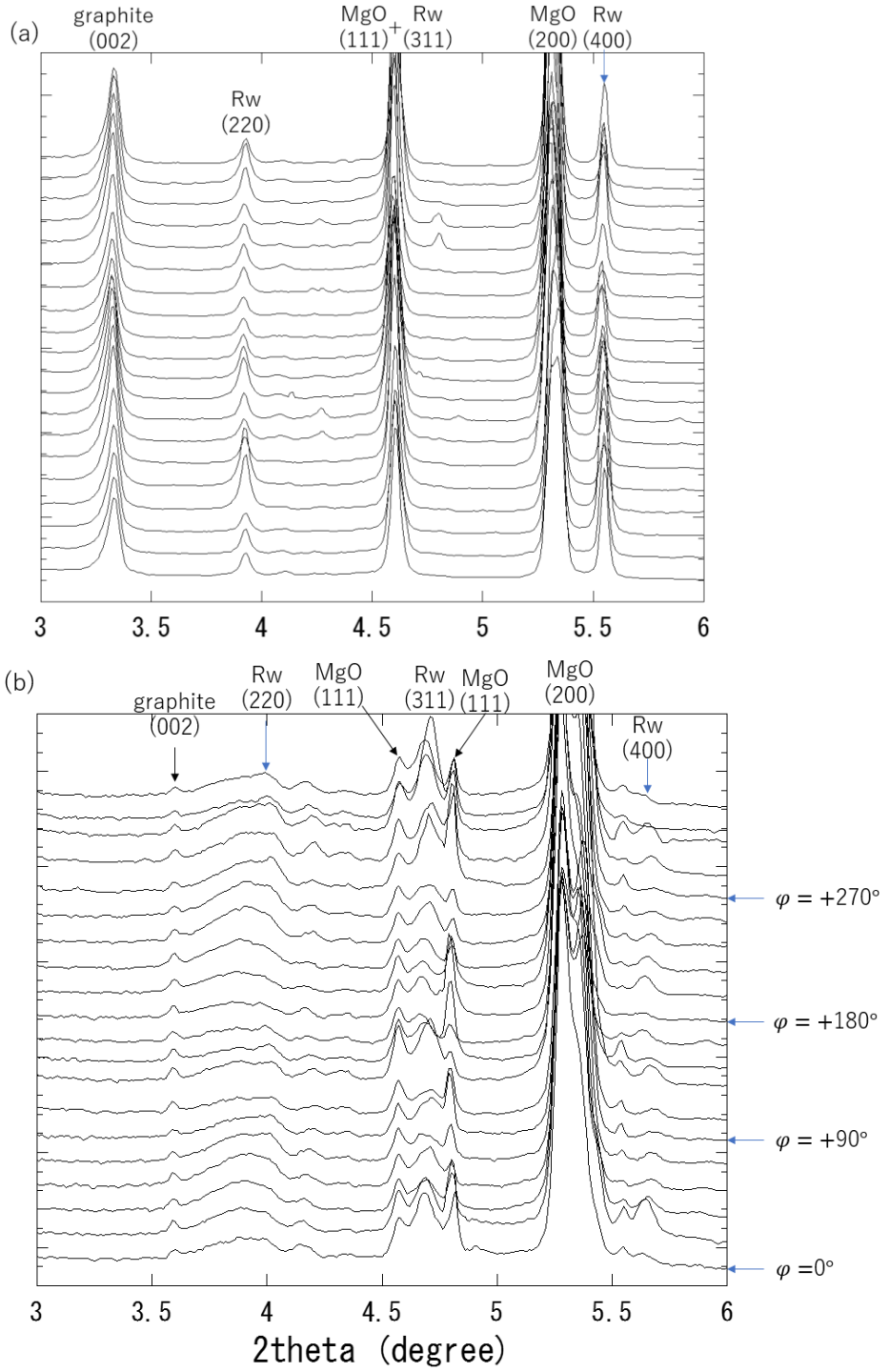

Fig. 1.36 1D-XRD patterns of ringwoodite subdivided into 20 sectors from Debye ring in the D-111 experiment (Run rwdefp81). (a) ambient condition. (b) 18 GPa, 1000°C and 15 % strain.

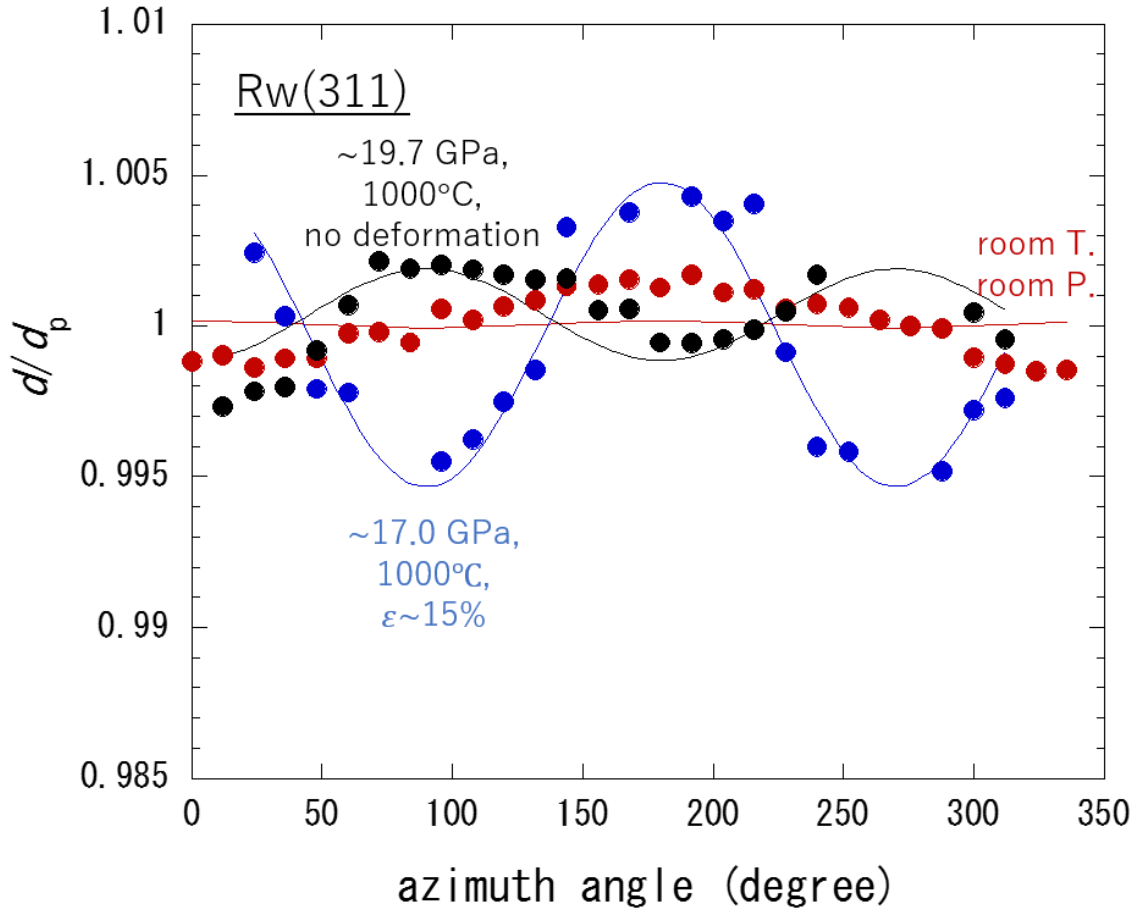

Fig. 1.37 Plots of d/d_p values of ringwoodite (311) with azimuth angle in the D-111 deformation experiment. Results of the fitting of the strain equation (eq. 1.6) to the data are also shown in solid lines.

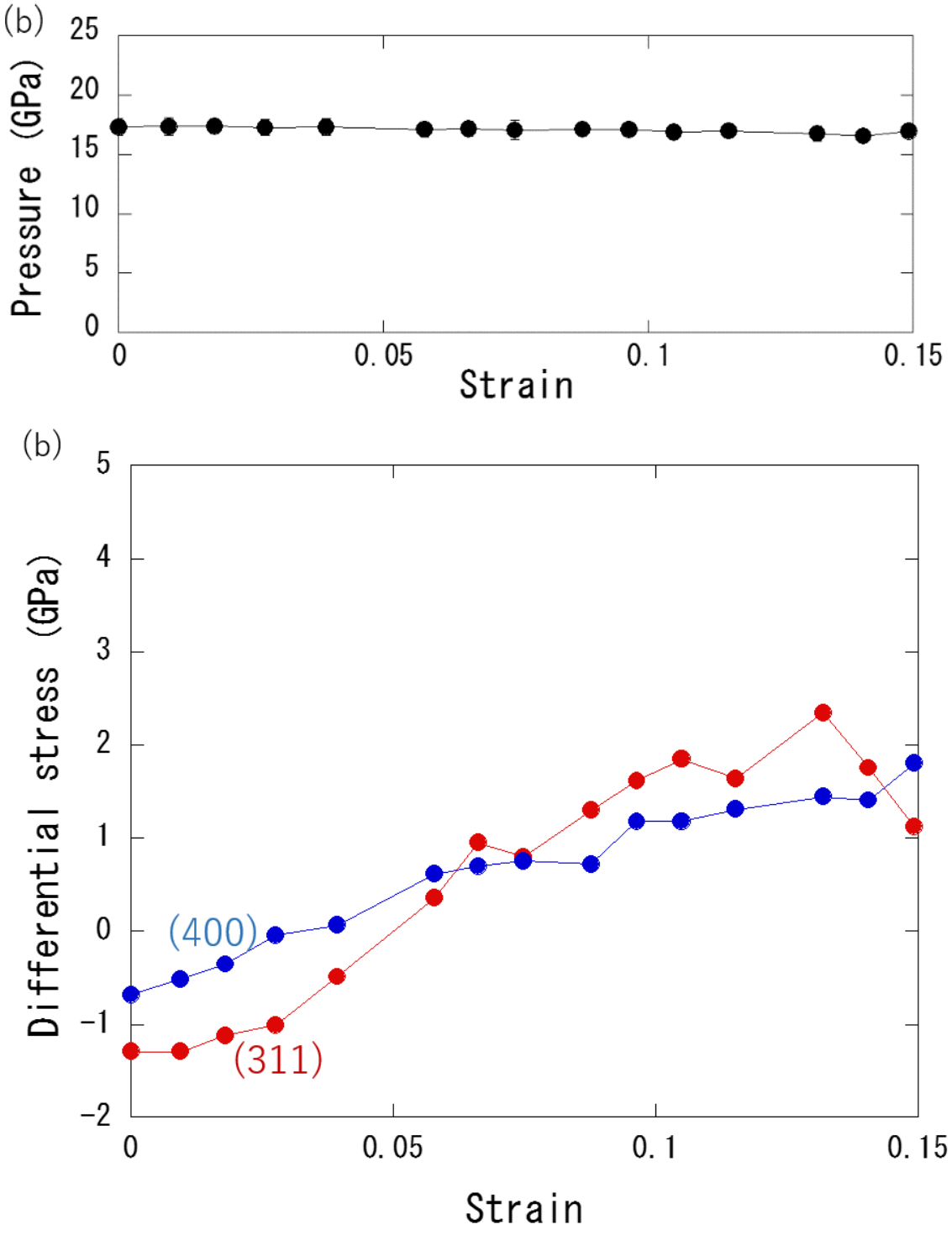

Fig. 1.38 Plots of pressure (a) and differential stress (b) with strain in a single-step deformation experiment using D-111 apparatus (Run rwdefp81).

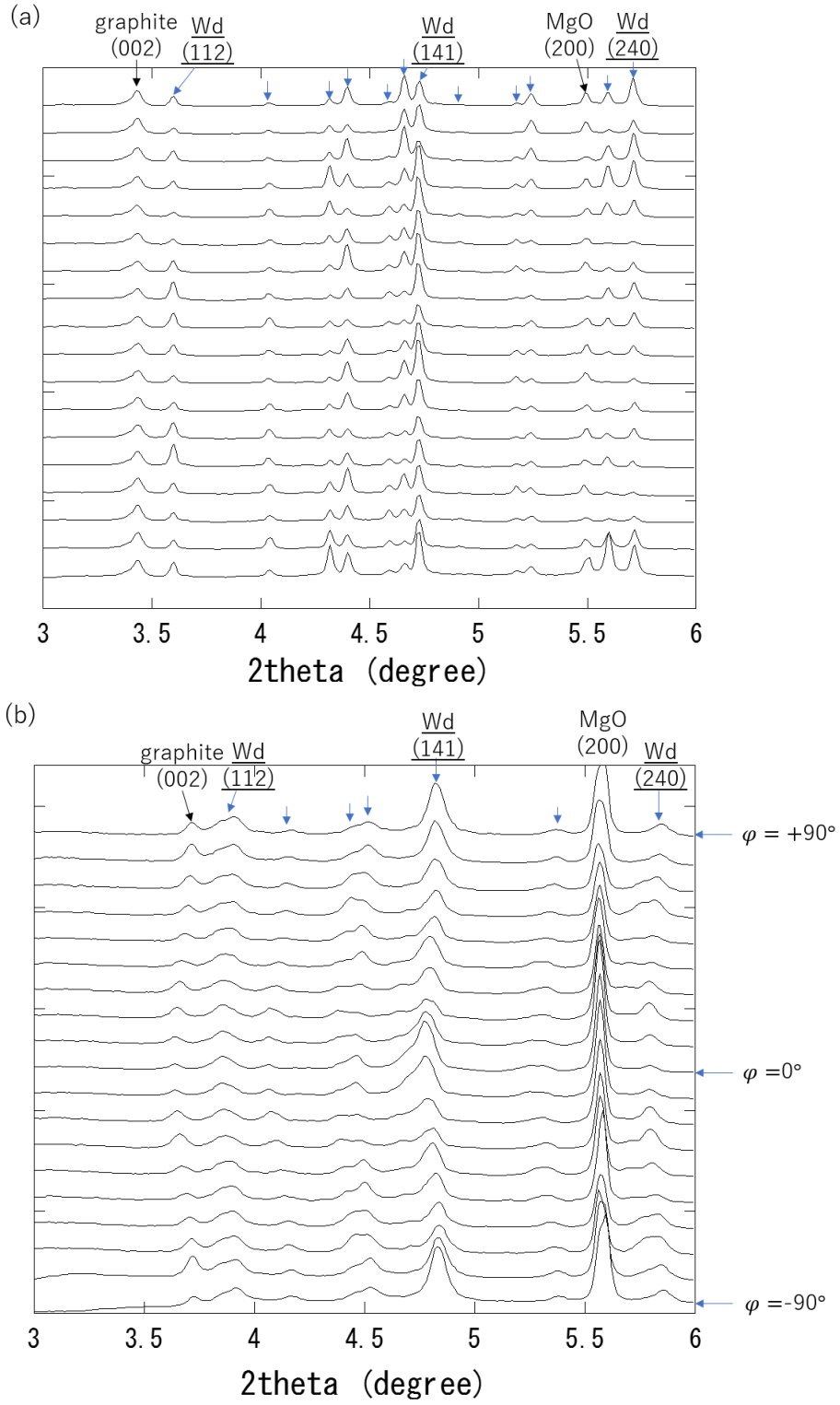

Fig. 1.39 1D-XRD patterns of wadsleyite subdivided into 20 sectors from Debye ring in Run wddefs11. (a) ambient condition. (b) 8.7 GPa, 500°C and 14 % strain.

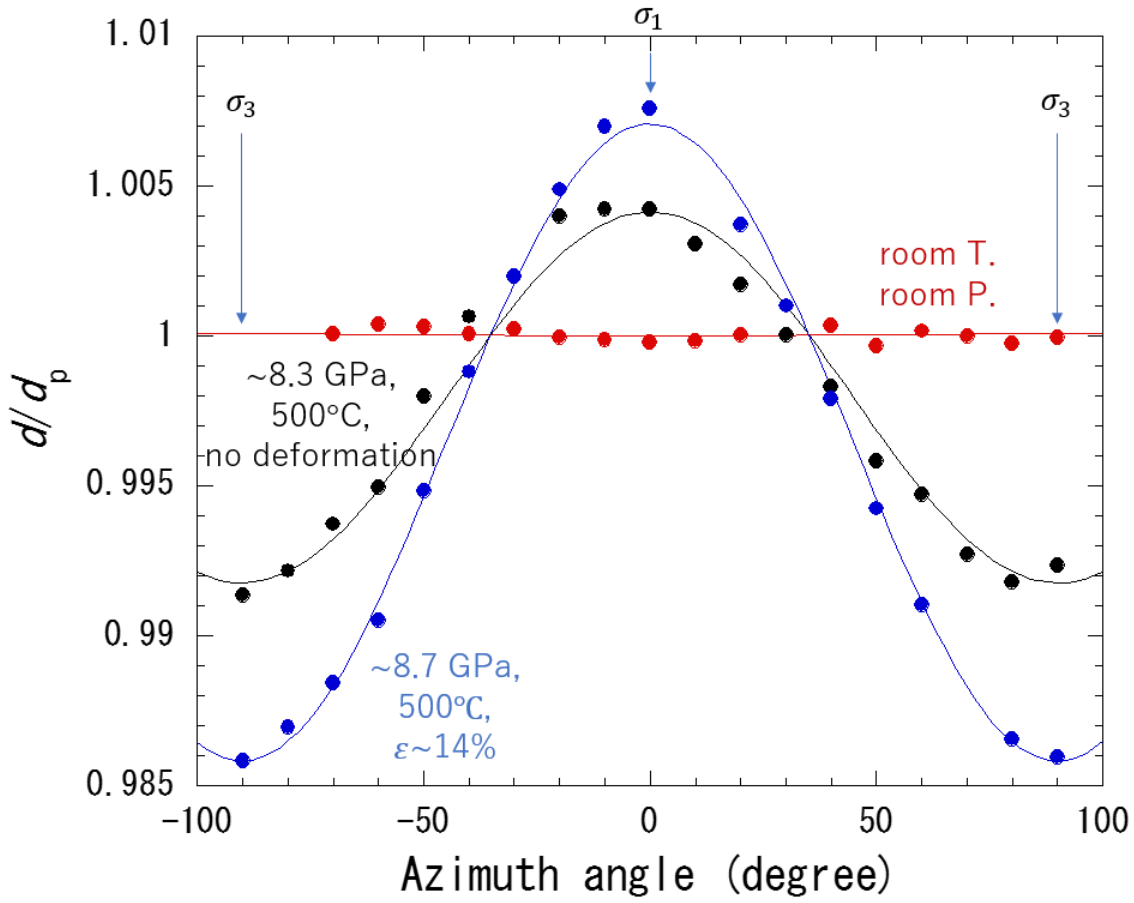

Fig. 1.40 Plots of *d*/*d*p of wadsleyite (112) with azimuth angle (Run wddefs11). Results of the fitting of the strain equation (eq. 1.6) to the data are also shown in solid lines.

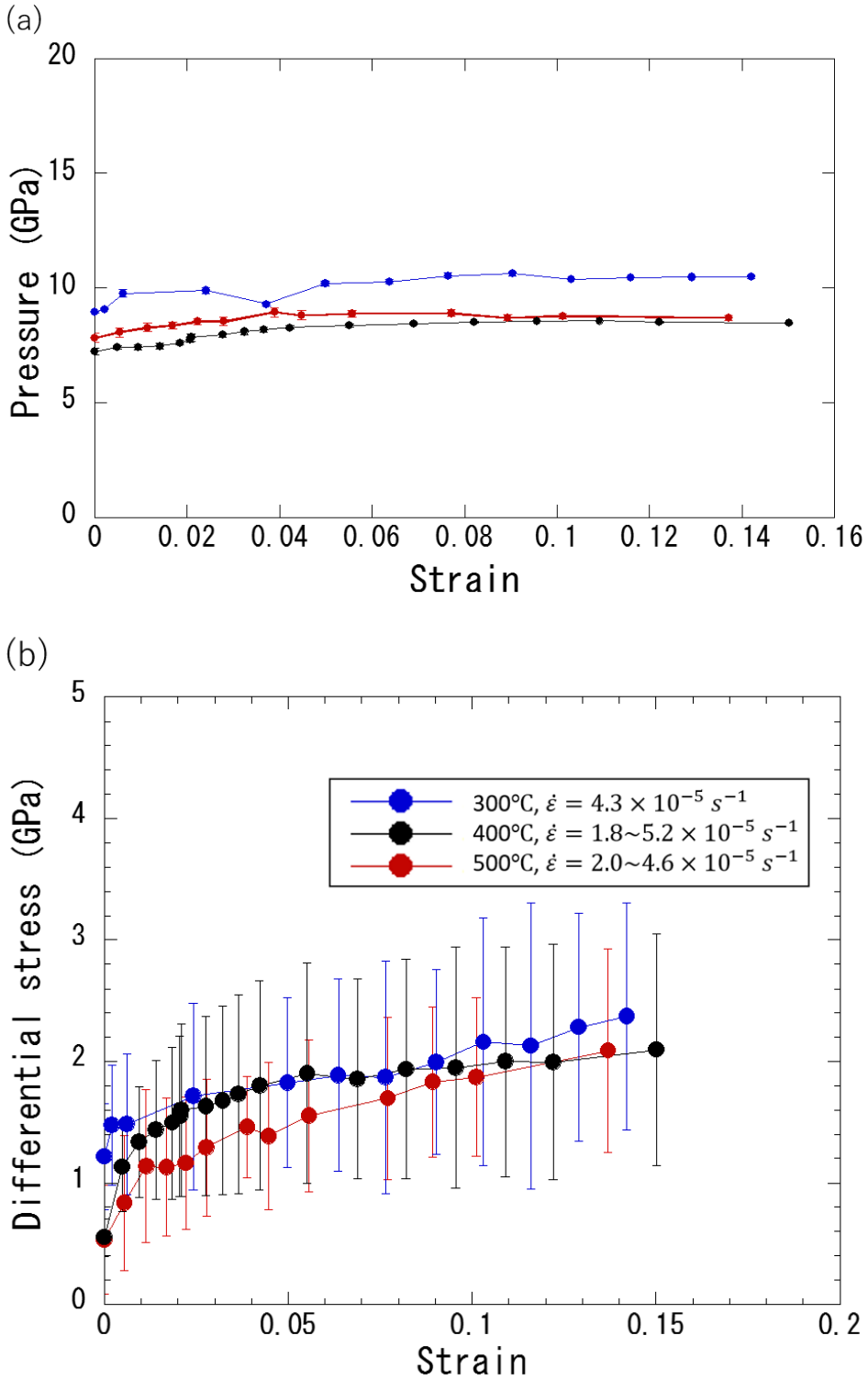

Fig. 1.41 Changes of pressure with strain (a) and the stress-strain curves (b) in the wadsleyite deformation experiments using D-DIA apparatus.

1.4. Discussion

1.4.1. Flow law of Peierls mechanism of ringwoodite

Creep strength of ringwoodite measured in this study is plotted as a function of temperature in Fig. 1.42. Because the strain hardening was observed especially at lower temperatures, the stress value at the 10 % strain was plotted in this figure. There have been few quantitative deformation experiments on ringwoodite so far. Shimojuku et al. (2009) have examined the diffusivity of the rate-controlling species Si in ringwoodite at 1400-1600°C, and constructed the flow laws of the dislocation and diffusion creep based on the Si diffusivity. Kawazoe et al. (2016) conducted the deformation experiments of ringwoodite in a similar way to the present study, and proposed the flow law of high-temperature dislocation creep from the creep data obtained at 1227°C-1427°C. Creep strength estimated from these previous studies are also shown in Fig. 1.42.

Fig. 1.42 indicated that the creep strength directly obtained at low temperatures in this study is much smaller than that estimated by the extrapolations of the flow laws of the dislocation and diffusion creep mechanisms to low temperatures in the previous studies (Shimojuku et al., 2009; Kawazoe et al., 2016). This suggests that Peierls mechanism is dominant at low-temperature conditions of our study at least with the

strain rate of ~10^{-5} s^{-1}. This is also supported by the fact that we did not observe any evidences for dynamic recrystallization in the recovered samples in contrast with the results of the high-temperature deformation experiment of Kawazoe et al. (2016). Our creep data is also in good agreement with the critical resolved shear stress for a dislocation glide in ringwoodite examined by the first principle study (Ritterbex et al., 2015).

The creep data obtained in this study was fitted by the flow law of the Peierls mechanism (eq. 1.2) to optimize the flow law parameters of ringwoodite. As in the case of olivine in some previous studies (e.g., Katayama and Karato, 2008; Mei et al., 2010), it was difficult to estimate Peierls parameters (p and q values in eq. 1.2) and the zero-stress activation enthalpy H_0 directly by the fitting. Therefore, the parameters of A and σ_p values were optimized with several sets of Peierls parameters (p=1, q=1; p=0.5, q=1; p=1, q=2). We also used the activation enthalpy obtained for the dislocation creep in Kawazoe et al. (2016) as the H_0 value in the fitting. The optimized parameters are summarized in Table 1.3, and the results of the fitting are also shown in red lines in Fig. 1.42.

The fitting curves approximately reproduce the obtained creep data including the room temperature data in the previous study (Nishiyama et al., 2005) although the

deviation becomes large at higher temperatures. The Peierls stress σ_p is estimated to be 6.4-8.3 GPa. These values are similar to those estimated based on the first principle study (σ_p=7-9 GPa, Ritterbex et al., 2015). On the other hand, Mei et al. (2010) conducted the D-DIA deformation experiments of olivine using the similar method to our study. Experimental conditions are also similar at ~4.5-9.5 GPa and 400-1000°C with the constant strain rates of 0.1-3.1×10^{-5} s^{-1}. They estimated the Peierls stress of olivine to be 5.9 ± 0.2 GPa with the Peierls parameters of p = 1/2, q = 1, that is slightly smaller than our estimated value of 6.8 ± 0.2 GPa with the same Peierls parameters (Table 1.3).

Katayama and Karato (2008) have shown that water weakens the olivine strength in Peierls mechanism by reducing the Peierls stress. Water contents in ringwoodite systematically decrease with increasing temperatures in this study (Table 1.2). This may result in underestimating the temperature effect on the creep strength if the similar water weakening also works in ringwoodite, which is not clear at the present stage. In order to assess this issue, it is necessary to better control the water content of the ringwoodite sample.

We also obtained some results on the creep strength in wadsleyite that is also shown in Fig. 1.42. The strength of wadsleyite is smaller than that of ringwoodite in this

study. Water contents of a recovered wadsleyite sample deformed at ~9 GPa and 500°C was estimated to be about 230 wt. ppm H_2O. This is smaller than that of ringwoodite recovered at ~10 GPa and 450-540°C (~1000 wt. ppm H_2O). Thus, the water weakening could not explain the difference in creep strength between wadsleyite and ringwoodite. Previous studies have shown that the wadsleyite strength was roughly close to that of ringwoodite at the higher temperature of 1423°C (Kawazoe et al., 2011; 2016). This may suggest that the rheology contrast between wadsleyite and ringwoodite changes with temperatures, however further deformation experiments are needed to evaluate this point.

.

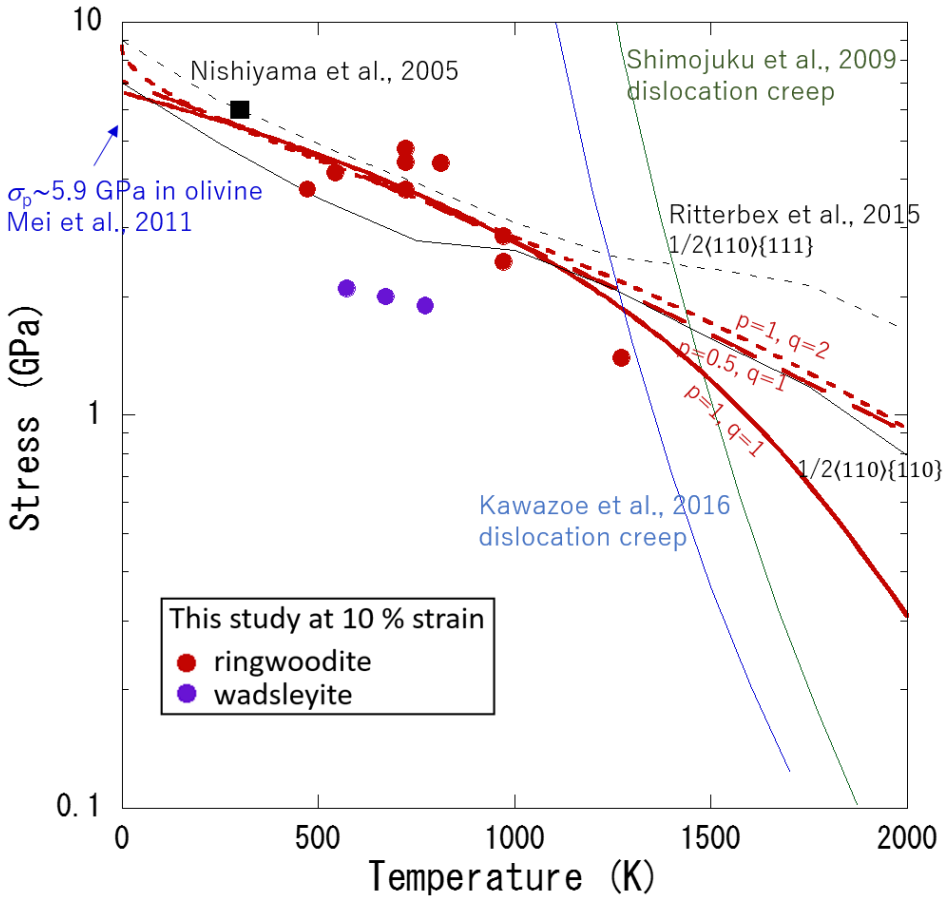

Fig. 1.42 Plots of creep strength of ringwoodite (red circles) and wadsleyite (purple circles) with temperature. Results of the fitting to the flow law of Peierls mechanism are shown in red lines (solid: p=1, q=1; dashed: p=0.5, q=1; dotted: p=1, q=2). The flow strength obtained at room temperature is shown by black square (Nishiyama et al., 2005). Creep strength in the dislocation creep regime estimated in previous studies was also shown in blue (from deformation experiment in Kawazoe et al., 2016) and green (from the Si diffusivity in Shimojuku et al., 2009) lines. Black lines indicate critical resolved shear stress of a dislocation glide in ringwoodite calculated by the first principle study (Ritterdex et al., 2015; solid: 1/2⟨110⟩{110}; dotted: 1/2⟨110⟩{111})

Table 1.3 Fitting results on the flow law (eq. 1.2) with representative Peierls parameters. Activation energy obtained in the high temperature deformation study (H_0 = 345 kJ/mol, Kawazoe et al., 2016) was used.

Peierls parameter	ln(A) ($s^{-1}GPa^{-2}$)	Peierls stress (GPa)
p=1, q=1	10.9 (9.5)	6.4 (0.2)
p=0.5, q=1	2.5 (10.1)	6.8 (0.2)
p=1, q=2	5.4 (10.1)	8.3 (1.0)

1.4.2. Deformation mechanism of ringwoodite under subduction zone conditions

Strain rates in laboratory deformation experiments are much larger than those in the Earth. In order to discuss the dominant deformation mechanism under subduction zone conditions, the flow laws of ringwoodite in several deformation mechanisms obtained in this study and previous studies are extrapolated to the low strain rate condition of 1×10^{-14} s^{-1} in Fig. 1.43. The flow stress based on the flow law of the Peierls mechanism (red lines) is smaller than those calculated from the diffusion and dislocation creep based on the Si diffusivity in ringwoodite (green lines, Shimojuku et al., 2009) at less than ~1000 K. And, it is also smaller than that estimated in the deformation study on the dislocation creep (blue dotted line, Kawazoe et al., 2016) at less than ~800 K. Thus, it seems to be a delicate issue which deformation mechanism is actually dominant under subduction zone conditions.

It is noteworthy that the extrapolations of the flow laws to subduction zone conditions are done in different ways among these deformation mechanisms. Both dislocation and diffusion creep mechanisms require large extrapolations in temperature because these flow laws were estimated based on the data obtained at high temperature conditions of 1227°C-1600°C. Because the activation enthalpy has relatively large uncertainties in previous studies, large errors are actually present in the estimate of the

creep strength at slab temperatures in Fig. 1.43. On the contrary, the creep strength in the Peierls mechanism depends on which Peierls parameters are used in the extrapolations.

In addition, water contents are also different among the data source in Fig. 1.43. The water contents in the ringwoodite sample of the previous studies are ~200 and ~600-1100 ppm H_2O in Shimojuku et al. (2009) and Kawazoe et al. (2016), respectively. The larger creep strength in the dislocation creep regime estimated in Shimojuku et al. (2009) compared to that in Kawazoe et al. (2016) might be originated from the difference in the water content. As mentioned in the previous section, the water contents in this study change with temperature, and its variation (~200-1900 wt. ppm H_2O) covers those reported in previous studies.

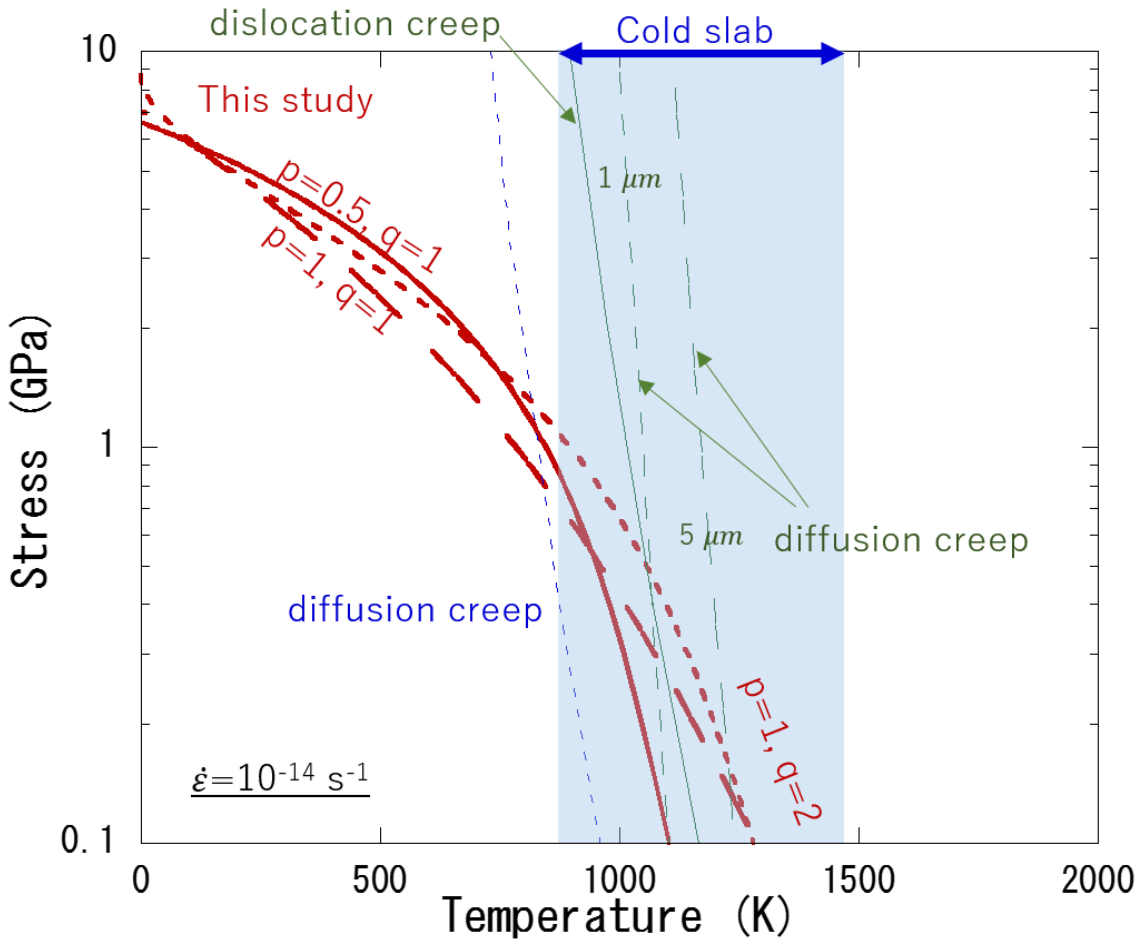

Fig. 1.43 Comparison of creep strength among several deformation mechanisms at the strain rate in the Earth (10^{-14} s^{-1}). Peierls mechanism from this study is shown in red lines (solid: p=1, q=1; dashed: p=0.5, q=1; dotted: p=1, q=2). Blue dotted line is for the dislocation creep in Kawazoe et al. (2016). Green lines are estimated from the Si diffusivity (solid line: dislocation creep; short and long dashed line: diffusion creep with the grain size of 1 μm and 5 μm).

1.4.3. Strength of subducting slabs in the mantle transition zone

Strength of subducting slabs in mantle transition zone conditions have been estimated in indirect ways based on results of analogue materials at lower pressures (e.g., Karato et al., 2001) and the Si diffusivity in wadsleyite and ringwoodite (e.g., Kubo et al., 2009; Kaneshima and Yoshioka, 2014) considering the grain-size evolution due to non-equilibrium transformations. In this study, the creep strength of ringwoodite in Peierls mechanism was directly measured from deformation experiments. Although we have not obtained conclusive results on the dominant deformation mechanism under subduction zone conditions, it has been suggested that the Peierls mechanism would be dominant at low temperatures in the cold center of subducting slabs (e.g., Karato et al., 2001; Kubo et al., 2009). Here we calculated strength of the cold subducting slabs in mantle transition zone on the basis of the flow law for the Peierls mechanism of ringwoodite determined in this study. Fig. 1.44 shows horizontal profiles of the slab strength along the temperatures estimated for the Tonga slab. The maximum strengths are estimated to be ~250-600 MPa at the cold slab core (~700°C) depending on the Peierls parameters used.

Fig.1.45 shows the effects of temperatures on the flow strength of subducting slabs with the Peierls parameter of p=1 and q=2, in which the temperature is varied by

±130°C relative to the Tonga slab. The maximum strength of the colder slab like Mariana slab (blue line) and the warmer slab (red line) is estimated to be ~900 MPa and ~200 MPa, respectively.

It has been suggested that the strength of subducting slabs in mantle transition zone is one of the important factors controlling the slab behavior around the 660 km discontinuity. In order to reproduce the slab behaviors in numerical simulation studies, yield strength of 200 MPa has been usually assumed for the slab rheology without any experimental supports (e.g., Nakakuki et al., 2010). Because the yield strength corresponds to a half value of flow strength under the condition of Tresca, the maximum slab strength was set to be 400 MPa in the numerical calculations to simulate various slab behaviors. The flow law of the Peierls mechanism determined in this study may not be far from the slab rheology assumed in the numerical simulation. It is desirable to conduct a numerical study for the slab dynamics taking more realistic rheology such as the Peierls mechanism into considerations.

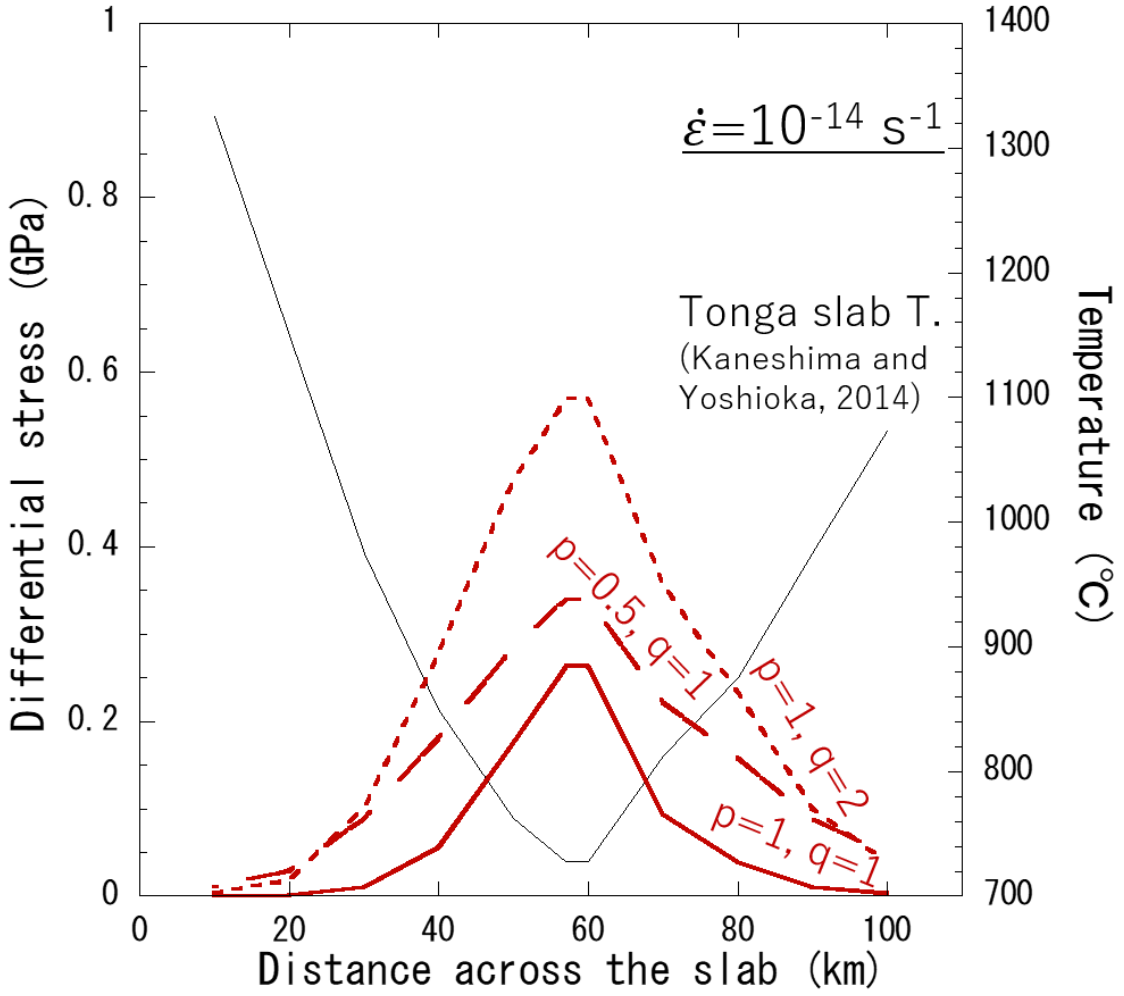

Fig. 1.44 Profiles of flow strength of ringwoodite in the Peierls mechanism at the strain rate of 10^{-14} s^{-1} across the Tonga slab (red lines). Results obtained using three sets of Peierls parameters are shown in red lines. Temperature distribution across the Tonga slab is also shown in black line (Kaneshima and Yoshioka, 2014).

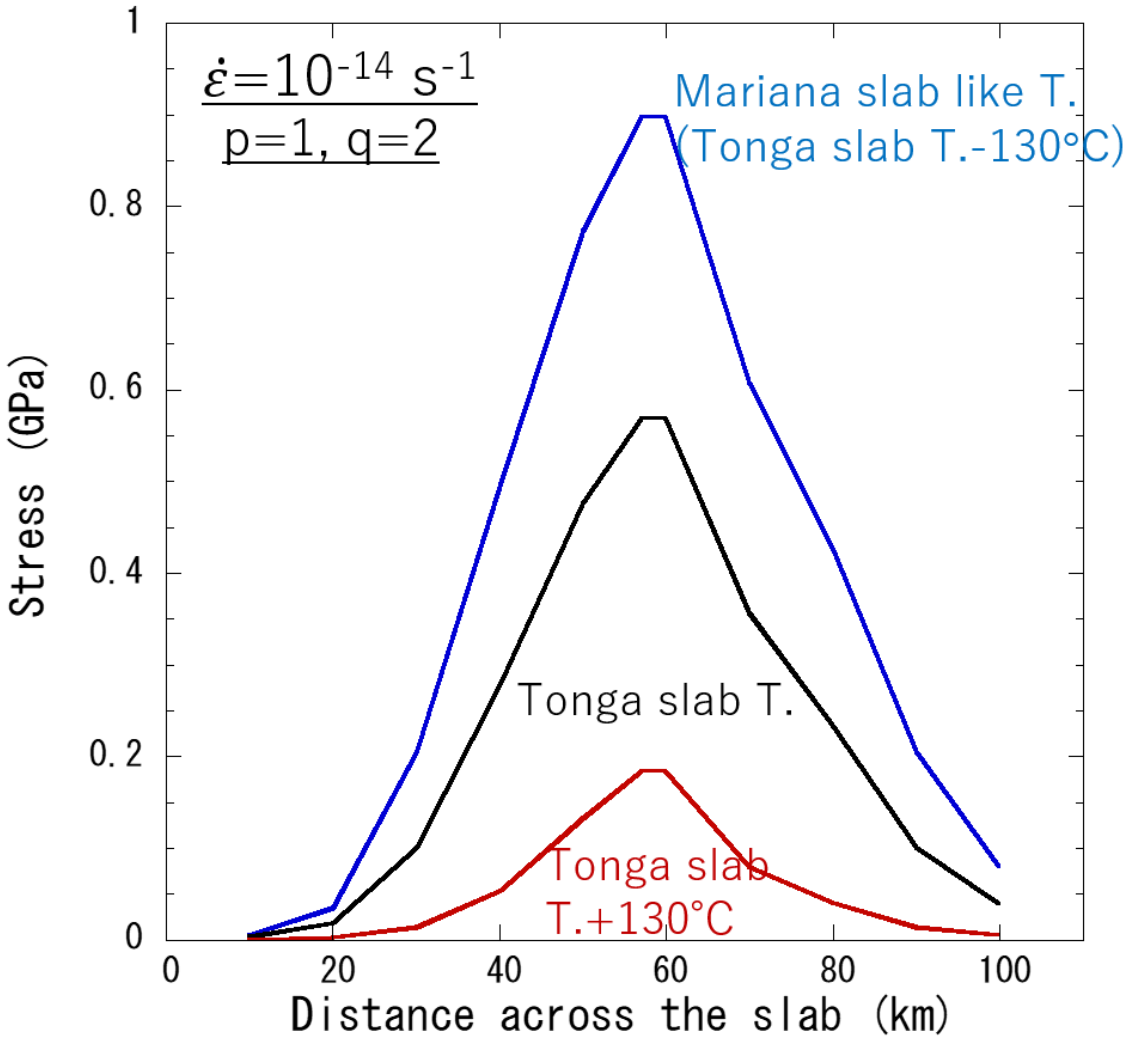

Fig. 1.45 Effect of temperature on the strength of ringwoodite in Peierls mechanism.

1.5. Summary

The deformation experiments of wadsleyite and ringwoodite were conducted at about 7-18 GPa and 200-1000°C with a constant strain (0.96-0.91× 10^{-5} s^{-1}) using the D-DIA and the D-111 apparatuses combined with synchrotron X-ray to construct the flow law of Peierls mechanism and constrain the strength of subducting slab in the mantle transition zone. The several types of slotted anvils were used for the high-pressure deformation experiments to obtain the 2D-XRD data. We could conduct the deformation experiments at about 10 GPa and 200-540°C with about 25% strain using WC anvils conically slotted by 6 degrees with a TEL of 4.0 mm. The D-111 apparatus was used at higher-pressure conditions.

The flow strength and microstructural observations suggest that the Peierls mechanism was dominant in the deformation of ringwoodite in this study. We could construct the flow law parameters for the Peierls mechanism with several sets of Peierls parameters. The estimated Peierls stress in ringwoodite is slightly larger than that of olivine. It is still difficult to constrain the dominant deformation mechanism of subducting slabs in the mantle transition zone partially because of large uncertainties due to the large extrapolations of the flow laws into low temperatures.

Based on the flow law of Peierls mechanism in ringwoodite, we estimated the horizontal profiles of the slab strength in mantle transition zone with the Tonga slab temperatures (Kaneshima and Yoshioka, 2014). The creep strength at the center of the cold slab was estimated to be ~250-600 MPa depending on the Peierls parameters. The maximum strength varies from ~200 MPa to ~900 MPa when changing the temperature by ±130°C relative to the Tonga slab. The slab rheology with the yield strength of 200 MPa (identical to the differential stress of 400 MPa) have been used in the numerical simulation for the deep slab behaviors (e.g., Nakakuki et al., 2010) It is desirable to incorporate more realistic rheology such as the Peierls mechanism in the numerical simulation.

Reference of chapter 1

N. Bolfan-Casanova, H. Keppler, and D. C. Rubie, Water partitioning at 660 km depth and evidence for very low water solubility in magnesium silicate perovskite. *Geophys. Res. Lett.* **30**, doi:10.1029/2003GL017182 (2005).

D. P. Dobson, S. A. Hunt, and H. J. Müller, Slotted carbide anvils: improved X-ray access for synchrotron-based multi-anvil experiments. *High press. Res*. **32**, 532-536 (2012).

R. Farla, G. Amulule, J. Girard, N. Miyajima, and S. Karato, High‐pressure and high‐temperature deformation experiments on polycrystalline wadsleyite using the rotational Drickamer apparatus. *Phys. Chem. Minerals*. **42**, 541-558 (2015)

Y. Fei, H. Mao, and J. Shu, Simultaneous High-P, High-T X-ray Diffraction Study of β-(Mg,Fe)2SiO4 to 26 GPa and 900K. *J. Geophys. Res. Solid Earth*. **97**, 4489–4495 (1992).

Y. Fukao, M. Obayashi, Subducted slabs stagnant above, penetrating through, and trapped below the 660 km discontinuity. *J. Geophys. Res. Solid Earth*. **118**, 5920–5938 (2013).

H. J. Frost, and M. F. Ashby, DEFORMATION-MECHANISM MAPS. *Pergamon Press.* (1982).

S. A. Hunt, D. J. Weidner, R. J.McCormack, M. L. Whitaker, E. Balley, L. Li, M. T. Vaughan, D. P. Dobson, Deformation T-Cup: A new multi-anvil apparatus for controlled strain-rate deformation experiments at pressures above 18 GPa. *Rev. Sci. Instrum.* **85** (2014).

J. Hustoft, G. Amulele, J. Ando, K. Otsuka, Z. Du, Z. Jing, S. Karato, Plastic deformation experiments to high strain on mantle transition zone minerals wadsleyite and ringwoodite in the rotational Drickamer apparatus. *Earth Planet. Sci. Lett.* **361**, 7–15 (2013).

T. Inoue, T. Irifune, Y. Higo, T. Sanehira, Y. Sueda, A. Yamada, T. Shinmei, D. Yamazaki, J. Ando, K. Funakoshi, and W. Utsumi, The phase boundary between wadsleyite and ringwoodite in Mg_2SiO_4 determined by in situ X-ray diffraction. *Phys. Chem. Minerals*. **33**, 106-114 (2006)

S. D. Jacobsen, J. R. Smyth, H. Spetzler, C. M. Holl, and D. J. Frost, Sound velocities and elastic constants of iron-bearing hydrous ringwoodite, *Phys. Earth Planet. Inter.* **143-144**, 47–56 (2004).

S. Kaneshima, and S. Yoshioka, Dominant role of temperature on deep earthquake mechanics for the Tonga slab near the bottom of the upper mantle. *Acad. Psychiatry*. **66**, 1–9 (2014).

S. Karato, M. R. Riedel, D. A. Yuen, Rheological structure and deformation of subducted slabs in the mantle transition zone: Implications for mantle circulation and deep earthquakes. *Phys. Earth Planet. Inter.* **127**, 83–108 (2001).

S. Karato, Deformation of Earthb Materials. *CAMBRIDGE UNIVERSITY PRESS* (2008)

I. Katayama, S. ichiro Karato, Low-temperature, high-stress deformation of olivine under water-saturated conditions. *Phys. Earth Planet. Inter.* **168**, 125–133 (2008).

T. Kawazoe, Y. Nishihara, T. Ohuchi, N. Nishiyama, Y. Higo, K. Funakoshi, and T. Irifune, In situ stress-strain measurements in a deformation-DIA apparatus at *P-T* conditions of the upper part of the mantle transition zone. *American Mineralogist*. **96**, 1665-1672 (2011).

T. Kawazoe, Y. Nishihara, T. Ohuchi, N. Miyajima, G. Maruyama, Y. Higo, K. Funakoshi, T. Irifune, Creep strength of ringwoodite measured at pressure–temperature conditions of the lower part of the mantle transition zone using a deformation–DIA apparatus. *Earth Planet. Sci. Lett.* **454**, 10–19 (2016).

T. Kubo, S. Kaneshima, Y. Torii, S. Yoshioka, Seismological and experimental constraints on metastable phase transformations and rheology of the Mariana slab. *Earth Planet. Sci. Lett.* **287**, 12–23 (2009).

T. Nakakuki, M. Tagawa, Y. Iwase, Dynamical mechanisms controlling formation and avalanche of a stagnant slab. *Phys. Earth Planet. Inter.* **183**, 309–320 (2010).

T. Nakakuki, E. Mura, Dynamics of slab rollback and induced back-arc basin formation. *Earth Planet. Sci. Lett.* **361**, 287–297 (2013).

Y. Nishihara, E. Takahashi, K. N. Matsukage, T. Igushi, K. Nakashima, K. Funakoshi, Thermal equation of state of $(Mg_{0.91}Fe_{0.09})_2SiO_4$ringwoodite. *Phys. Earth Planet. Inter.* **143**, 33–46 (2004).

Y. Nishiharam T. Kubo, T. Yoshino, T. Ohuchi, D. Yamazaki, and N. Tsujino, D111-type guide block for high-pressure deformation experiments, JpGU. S-IT22-P32 (2017).

N. Nishiyama, Y. Wang, T. Uchida, T. Irifune, M. L. Rivers, and S. R. Sutton, Pressure and strain dependence of the strength of sintered polycrystalline Mg_2SiO_4 ringwoodite. *Geophys. Res. Lett.* **32**, 1–4 (2005).

N. Nishiyama, Y. Wang, T. Irifune, and M. L. Rivers, Development of the Multi-anvil Assembly 6-6 for DIA and D-DIA type high-pressure apparatuses. *High press. Res*. **28**, 307-314 (2008)

S. Mei, A. M. Suzuki, D. L. Kohlstedt, N. A. Dixon, and W. B. Durham. Experimental constrains on the strength of the lithospheric mantle. *J. Geophys. Res.* **115**, doi:10.1029/2009JB006873 (2010).

H. Morishima, T. Kato, E. Ohtani, S. Urakawa, W. Utsumi, O. Shimomura, and T. Kikegawa. The Phase Bouondary Between α- and β-Mg_2SiO_4 Determined by the in Situ X-ray Observation. *Science*. **265**, 1202-1203 (1994).

D. G. Pearson, F. E. Brenker, F. Nestola, J. Nasdaka, M. T. Hutchison, S. Matveev, G. Silversmit, S. Schmitz, B. vekemans, and L. Vincze, Hydrous mantle transition zone indicated by ringwoodite included within diamond. *Nature*. **507**, 221-224 (2014).

A. E. Ringwood, Phase transformations and their bearing on the constitution and dynamics of the mantle. *Geochim. Cosmochim. Acta*. **55**, 2083–2110 (1991).

S. Ritterbex, Ph. Carrez, K. Gouriet, P. Cordier, Modeling dislocation glide in Mg_2SiO_4 ringwoodite: Towards rheology under transition zone conditions. *Phys. Earth Planet. Inter.* 1–13 (2015).

A. Shimojuku, T. Kubo, E. Ohtani, T. Nakamura, R. Okazaki, R. Dohmen, S. Chakraborty, Si and O diffusion in $(Mg,Fe)_2SiO_4$ wadsleyite and ringwoodite and

its implications for the rheology of the mantle transition zone. *Earth Planet. Sci. Lett.* **284**, 103–112 (2009).

R. Shiraishi, E. Ohtani, T. Kubo, N. Doi, A. Suzuki, A. Shimojuku, T. Kato, and T. Kikegawa, Deformation cubic anvil press and stress and strain measurements using monochromatic X-rays at high pressure and high temperature. *High. Press. Res*. **31**, 399-406 (2011).

A. K. Singh, The lattice strains in a specimen (cubic system) nonhydrostatically in an opposed anvil device. *J. Appl. Phys.* **2**, 4278–4286 (1993).

A. K. Singh, C. Balasingh, H. K. Mao, R. J. Hemley, J. Shu, Analysis of lattice strains measured under nonhydrostatic pressure. *J. Appl. Phys.* **83**, 7567–7575 (1998).

S. V. Sinogeikin, and J. D. Bass, Single-crystal elasticity of γ-$(Mg_{0.91}Fe_{0.09})_2SiO_4$ to high pressures and to high temperatures. *Geophys. Res. Lett.* **28**, 4335–4338 (2001).

Y. Torii, S. Yoshioka, Physical conditions producing slab stagnation: Constraints of the Clapeyron slope, mantle viscosity, trench retreat, and dip angles. *Tectonophysics*. **445**, 200–209 (2007).

M. C. Tsenn, N. L. Carter, Upper limits of power law creep of rocks. *Tectonophysics*. **136**, 1–26 (1987).

T. Uchida, Y. Wang, M. L. Rivers, S. R. Sutton, Yield strength and strain hardening of MgO up to 8 GPa measured in the deformation-DIA with monochromatic X-ray diffraction. *Earth Planet. Sci. Lett.* **226**, 117–126 (2004).

J. Wang, J. D. Bass, T. Kastura, Elastic properties of iron-bearing wadsleyite to 17.7GPa: Implications for mantle mineral models. *Phys. Earth Planet. Inter.* **228**, 92–96 (2014).

Y. Wang, W. B. Durham, I. C. Getting, D. J. Weidner, The deformation-DIA: A new apparatus for high temperature triaxial deformation to pressures up to 15 GPa. *Rev. Sci. Instrum.* **74**, 3002–3011 (2003).

Y. Xu, D. J. Weidner, J. Chsen, M. T. Vaughan, Y. Wang, T. Uchida, Flow-law for ringwoodite at subduction zone conditions. *Phys. Earth Planet. Inter.* **136**, 3–9 (2003).

Chapter 2:

Grain growth kinetics of pyrolitic materials under the lower mantle conditions: Implications for the grain-size evolution and rheology of the lower mantle and subducting slabs.

2.1. Introduction

Phase equilibrium studies on pyrolitic composition have shown that bridgmanite (Brg) is a major phase and ferropericlase (Fp), Ca-perovskite (Capv), and majoritic garnet (Mjgt) are minor phases in the upper part of lower mantle (<~700 km) (Fig. 2.1 blue line, Irifune, 1994). The volume fractions at 24 GPa are about 70 vol %, 15 vol %, 10 vol % and 5 vol % for bridgmanite, ferropericlase, majoritic garnet, and Ca-perovskite, respectively. The volume fraction of majoritic garnet becomes large at high temperatures (Nishiyama and Yagi, 2003). On the other hand, the three phases without majoritic garnet exist in the deeper lower mantle (e.g., Irifune, 1994; Nishiyama et al., 2004). The volume fractions at 27 GPa are about 80 vol %, 15 vol % and 5 vol % for bridgmanite, ferropericlase, and Ca-perovskite, respectively. These fractions do not change with temperature (Nishiyama and Yagi, 2003).

It has been suggested that the deformation of the lower mantle occurs

dominantly by diffusion creep because seismic anisotropy is not observed in the most parts (e.g., Karato et al., 1995). However, the seismic anisotropy has been locally observed at the strongly deformed regions around the subducting slab and the D" layer (e.g., subducting slab: Wookey et al., 2002; Wookey and Kendall, 2004; Foley and Long, 2011, D" layer: Lay et al., 1998; Moore et al., 2004). In these regions, seismic anisotropy may be originated from lattice preferred orientation of bridgmanite and/or ferropericlase (e.g., bridgmanite: Mainprice et al., 2008; Tsujino et al., 2016, ferropericlase: Yamazaki and Karato, 2002).

The depth profile of the lower-mantle viscosity has been studied based on the post-glacial rebound (e.g., Nakada and Lambeck, 1989; Peltier, 1996, 1998; Mitrovica et al., 2015; Lau et al., 2016; Nakada et al., 2018) and convection related observables such as geoid anomalies and dynamic topography on the core-mantle boundary (e.g., Forte and Mitrovica, 2001; Rudolph et al., 2015). The lower mantle viscosity, that is thought to be larger than the upper mantle, has been estimated to be $10^{21\text{-}23}$ Pas (e.g., Peltier, 1998; Mitrovica and Forte, 2004, Lau et al., 2016).

Grain size is one of the important parameters for the lower mantle rheology and viscosity. Dominant deformation mechanism depends on the grain size. The viscosity also drastically changes with the grain size when the diffusion creep is dominant.

Therefore, it is indispensable to constrain the grain-size evolution in the lower mantle. Grain size will become small due to the post-spinel transformation when the materials are transported into the lower mantle (e.g., Kubo et al., 2000). Grain growth process would control the grain-size evolution after the post-spinel transformation (e.g., Yamazaki et al., 1996; Kubo et al., 2009).

The grain growth kinetics is generally described as follows (e.g., Nishizawa, 1984; Karato, 1989)

$$d^n - {d_0}^n = k_n t \tag{2.1}$$

, where d is the grain size, d_0 is the initial grain size, t is time, n is the grain growth exponent, and k_n is the rate constant. The n value changes by the grain growth mechanism. The rate constant k_n has an Arrhenius-type temperature dependence and is given by

$$k_n = k_{n0}\exp(-\frac{H^*}{RT}) \tag{2.2}$$

, where k_{n0} is pre-exponential factor, H^* is the activation enthalpy, R is the gas constant and T is absolute temperature.

When the normal grain growth occurs in a single-phase system, the grain growth rate can be described below.

$$\frac{dd_s}{dt} = M \times \Delta G \tag{2.3}$$

, where d_s is grain size in a single-phase system, M is mobility, ΔG is the sum of grain-boundary energy of grain growth of major phase (driving force). The driving force ΔG is expressed by the Gibbs-Thomson's equation and is described below (e.g., Nishizawa, 1984).

$$\Delta G = P \times V = \frac{2\gamma V}{d_s} \tag{2.4}$$

, where P is the inner pressure of grain, V is the molar volume, γ is the grain-boundary energy and d_s is the grain size. Then, the grain growth kinetics in the single-phase system can be described by integrating eq. 2.3 and eq. 2.4 as follows:

$$d_s{}^2 - d_{s0}{}^2 = k_2 t \tag{2.5}$$

$$k_2 = 4M\gamma V \tag{2.6}$$

Thus, the n value is 2 in the single-phase system. Actually, the n value estimated from the grain growth experiments in the single-phase system is about 2 (e.g., Karato, 1989, Nishihara et al., 2006, Tsujino and Nishihara, 2009).

On the other hand, the grain growth rate in a multi-phase system is controlled by Zener pinning and Ostwald ripening of the minor phase. The driving force for the grain-boundary migration of the major phase is decreased by the pinning effect of the minor phase (Zener pinning). In this case, the grain size ratio can be summarized in the following equation.

$$\frac{d_I}{d_{II}} = \frac{\beta}{{f_{II}}^z} \tag{2.7}$$

, where d_{I} is the grain size of the major phase, d_{II} is the grain size of the minor phase, f_{II} is the volume fraction of minor phase, β and z is the Zener parameters (e.g., Evans et al., 2001).

The details of the Zener parameters were discussed in Evans et al. (2001). The z value depends on the location of the minor phase. When the grains of minor phase are smaller than those of major phase and are randomly located, the z value is 1. When the grains of minor phase are solely on the grain boundary of major phase and is not included in the grains of major phase, the z value is 0.5. When the particles of minor phase are only located at the corner of major phase, the z value is 1/3. On the other hand, the β value depends on the relative boundary energy. This relationship is described below.

$$\beta = \frac{4\gamma_{\mathrm{GB}}}{3\gamma_{\mathrm{IPB}}} \tag{2.8}$$

, where γ_{GB} is the grain boundary energy, γ_{IPB} is the interphase boundary energy.

The grain growth exponent (n value) in eq. 2.1 changes with the grain growth mechanism in the multi-phase system. When particles of minor phase are randomly located in the major phase, the Ostwald ripening process occurs by the volume diffusion in major phase. In this case, the grain growth rate of minor phase can be described as

follows:

$$\frac{dd_{\mathrm{II}}}{dt} = M_3 \frac{D_{\mathrm{v}}}{d_{\mathrm{II}}} \times \frac{2\gamma V}{d_{\mathrm{II}}} \tag{2.9}$$

, where d_{II} is the grain size of minor phase, M_3 is the mobility in the case of n=3, and D_{v} is the volume diffusion (e.g., Nishizawa, 1984). The grain growth kinetics is obtained by integrating eq. 2.9 as follows:

$$d_{II}{}^3 - d_{II0}{}^3 = k_3 t \tag{2.10}$$

$$k_3 = 6M_3 D_v \gamma V \tag{2.11}$$

Thus, the n value is 3 when the Ostwald ripening process is controlled by the volume diffusion.

On the other hand, the Ostwald ripening of minor phase occurs by the grain boundary diffusion when the grains of minor phase are located at the grain boundary of major phase. In this case, the grain growth rate of minor phase can be described as follows:

$$\frac{dd_{II}}{dt} = M_4 \frac{wD_{gb}}{d_{II}{}^2} \times \frac{2\gamma V}{d_{II}} \tag{2.12}$$

, where M_4 is the mobility in the case of n=4, w is the width of grain boundary, and D_{gb} is the grain-boundary diffusion coefficient (e.g., Nishizawa 1984). The grain growth kinetics is obtained by integrating eq. 2.12 as follows:

$$d_{II}{}^4 - d_{II0}{}^4 = k_4 t \tag{2.13}$$

$$k_4 = 8M_4 w D_{gb} \gamma V \quad (2.14)$$

Thus, the n value is 4 when the Ostwald ripening process is controlled by grain boundary diffusion.

The grain growth kinetics of the major phase is described from the grain growth kinetics of the minor phase and Zener relationship as follows:

$$d_I{}^4 - d_{I_0}{}^4 = \left(\frac{\beta}{f_{II}{}^z}\right)^4 k_4 t \quad (2.15)$$

$$k_4 = \frac{8\gamma c w D_{gb} V^2 \upsilon}{3GRT} \quad (2.16)$$

, where k_4 is the same of that in eq. 2.14, γ is the interphase grain boundary energy, c is the concentration of the rate-controlling species, w is the width of grain boundary, D_{gb} is the grain-boundary diffusion coefficient, υ is the constant which changes by the volume fraction of major phase, G is a geometric constant, R is the gas constant, and T is temperature (e.g., Speight, 1968; Ardell, 1972).

There have been several experimental studies on the grain growth kinetics of silicate minerals in multi-phase system (e.g., Yamazaki et al., 1996, Ohuchi and Nakamura, 2007, Yamazaki et al., 2010, Hiraga et al., 2010, Tasaka and Hiraga, 2013). Hiraga et al. (2010) and Tasaka and Hiraga (2013) conducted the grain growth experiments in the olivine-enstatite system, and successfully analyzed grain growth data on the basis of grain growth kinetics and Zener relationship as mentioned above. They

demonstrated that the grain growth kinetics in the multi-phase system is very important for understanding the grain-size evolution and the viscosity variation in the upper mantle. Because it has been suggested that the grain-size dependent creep is dominant in the lower mantle, it is indispensable to conduct this kind of the grain growth study under the lower mantle conditions.

However, the *n* value obtained in the multi-phase system are not always ~3-4, but sometimes becomes much larger values. For example, Yamazaki et al. (1996) conducted grain growth experiments of $MgSiO_3$ bridgmanite and MgO periclase under lower mantle conditions and reported large *n* values of about 11. These results imply that the grain growth is too slow to explain the lower-mantle viscosity . Solomatov et al. (2001) discussed that the reason for the large *n* value in Yamazaki et al. (1996) may be due to the incorporation of the grain growth data with non-equigranular eutectoid texture at the initial stage. On the other hand, the Si diffusion coefficients of bridgmanite have been measured in the previous studies (e.g., Yamazaki et al., 2000; Xu et al., 2011). To explain the lower-mantle viscosity from the Si diffusivity, relatively large grain size of about 3 mm is required for bridgmanite (e.g., Yamazaki and Karato, 2001). Thus, the grain-size evolution and the viscosity in the lower mantle have not been well understood in terms of the grain growth kinetics of multi-phase system.

In this study, the grain growth experiments of pyrolitic composition in the multi-phases system were conducted under lower mantle conditions. We carefully took the grain growth data from homogeneous and equigranular texture. We also considered Zener pinning and Ostwald ripening process of minor phase. Then, we discussed the grain-size evolution and the viscosity variations in the lower mantle and lower-mantle slabs on the basis of the grain growth kinetics obtained in the multi-phase system of pyrolitic material.

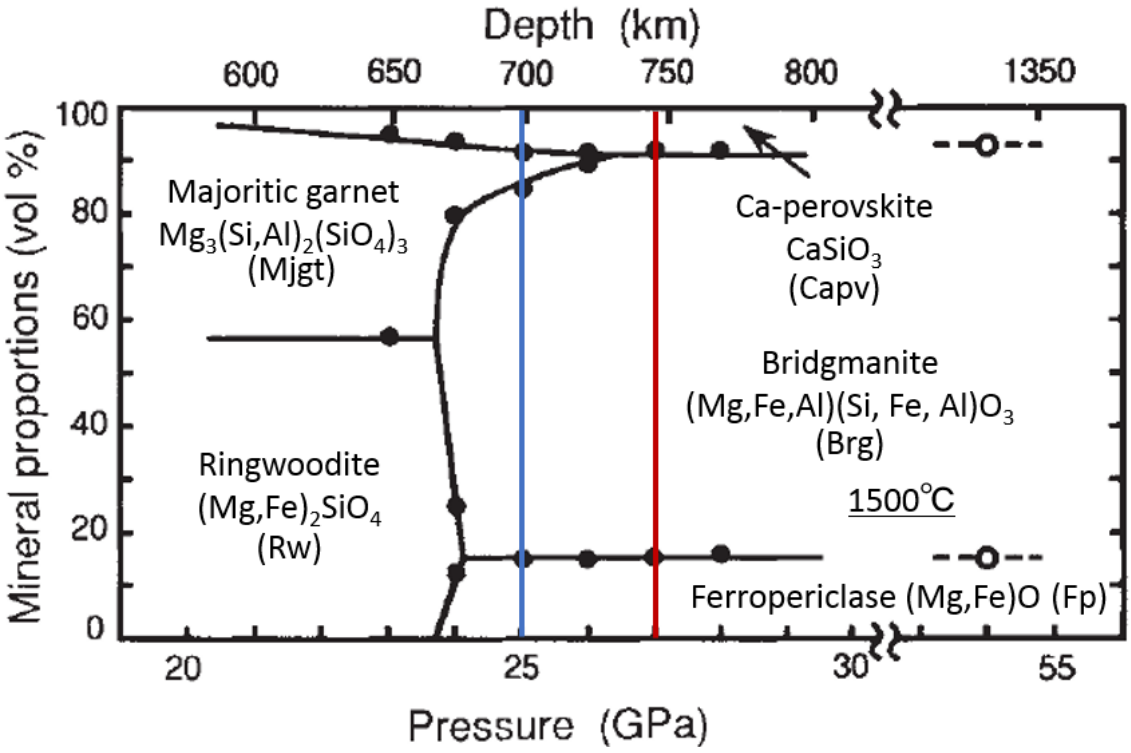

Fig. 2.1 Mineral proportions of pyrolitic material at 1500°C as a function of depth and pressure (modified from Irifune, 1994). Blue and red lines represent the pressure condition of our experiments.

2.2. Experimental procedure

2.2.1. Synthesis of starting material

The annealing experiments were performed using a powder of pyrolite composition as a starting material (Table 2.1). Chemical composition of the powder is similar to that used in Irifune (1994). The method of the synthesis of starting material was described below. First, the powder of MgO and TiO_2, and the nanopowder of SiO_2 and Al_2O_3 were each dried at 1000°C in air using the muffle furnace. These annealed powders and the powders of Cr_2O_3, NiO, Fe_2O_3, $CaCO_3$, and Na_2CO_3 were mixed using agate mortar. The mixed powder was pressed to make a pellet. This pellet was annealed at 1000°C using an oxygen-fugacity controlled furnace. Then, the annealed pellet was milled using the agate mortar to get the fine powder of pyrolitic chemical composition. This starting material was kept in a vacuum oven at 140°C to avoid absorption of water into the starting material.

Table 2.1 Chemical composition of the starting material used in this study

	pyrolite (wt%)
SiO_2	45.51 (1.03)
TiO_2	0.49 (0.25)
Al_2O_3	4.26 (0.23)
Cr_2O_3	0.62 (0.18)
FeO	7.78 (0.25)
MgO	36.82 (1.16)
NiO	0.33 (0.20)
CaO	3.73 (0.46)
Na_2O	0.46 (0.08)
Total	100

2.2.2. Grain growth experiments

The grain growth experiments of pyrolitic material were carried out using the Kawai-type multi-anvil apparatus at Kyushu University (QDES) (Fig. 1.4) and at Geodynamics Research Center (GRC) of Ehime University. Tungsten carbide anvils with a TEL of 2.5 mm (Fujilloy F08) were used with pyrophyllite gaskets of 2.5 mm in height and 3.0 mm in width for the grain growth experiments at 25 GPa. In the case of experiments at 27 GPa, anvils with a TEL of 3.0 mm (Fujilloy TF05) and pyrophyllite gaskets of 3.0 mm in height and 2.5 mm in width were used.

Fig. 2.2 shows the sample assemblies for annealing experiments at 25 GPa (Fig. 2.2a) and 27 GPa (Fig. 2.2b). These assemblies were composed of a sintered (Mg, Co)O pressure medium, a cylindrical $LaCrO_3$ heater, MgO insulators and graphite capsule. Temperature is measured by the W3%Re-W25%Re thermocouples. The relationship of temperature and electric power were summarized in Fig. 2.3, which systematically changed when we used a different block of $LaCrO_3$ after the run of Py_42.

The pressure calibration at room temperature was made by using pressure fixed points of ZnS (15.6 GPa), GaAs (18.7 GPa) and GaP (23.5 GPa) (Dunn and Bundy, 1978; Ito, 2007). On the other hand, the pressure calibration at 1600°C was made by using transition of Mg_2SiO_4 ringwoodite to $MgSiO_3$ bridgmanite + MgO periclase (23.0

GPa) (Fei et al., 2004).

The sample was pressed to 500 ton at room temperature condition and then heated to desired temperatures with a heating rate of 100°C/min. The sample was slowly decompressed after quenching.

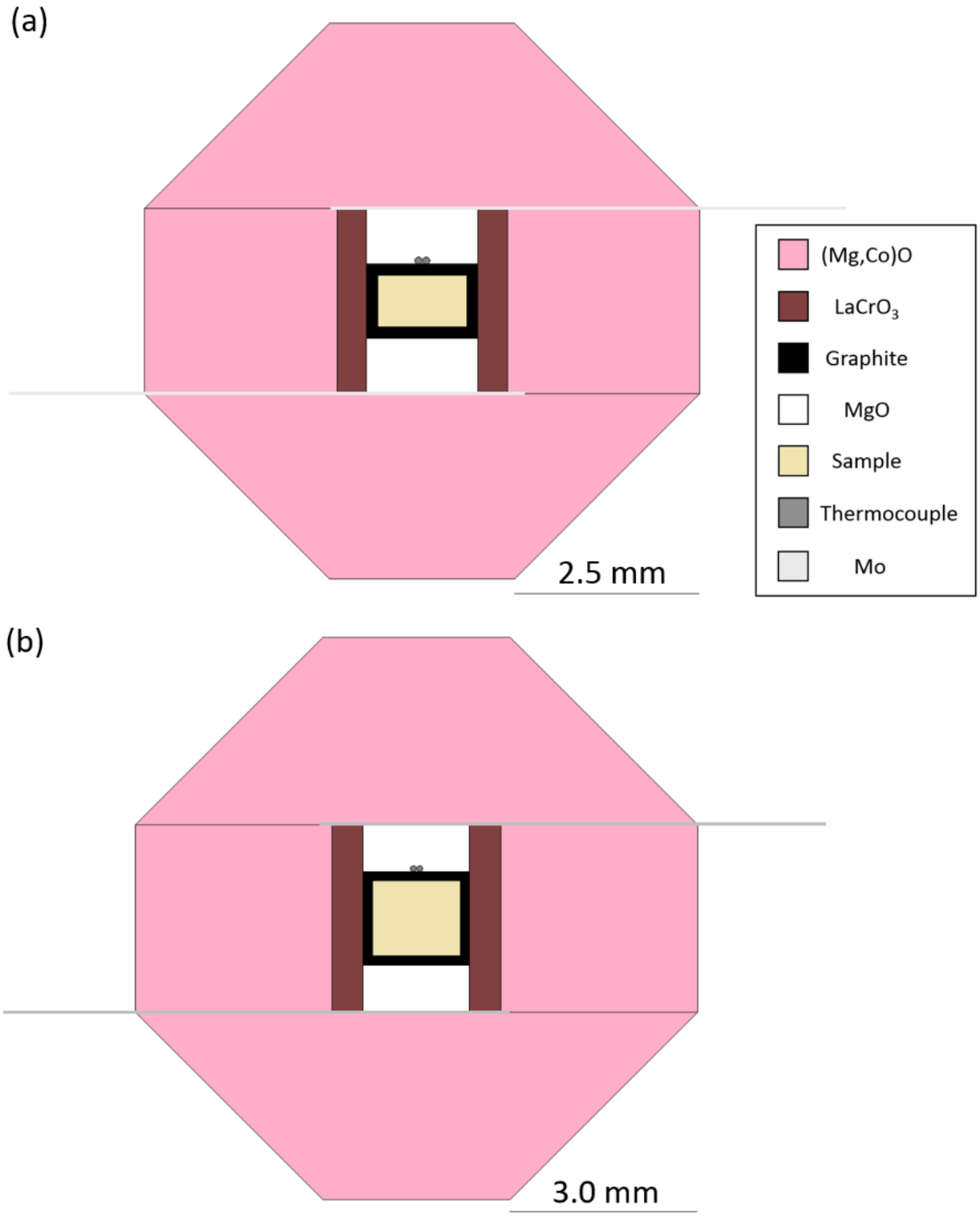

Fig. 2.2 Sample assemblies for grain growth experiments (a: TEL 2.5 mm, b: TEL 3.0 mm).

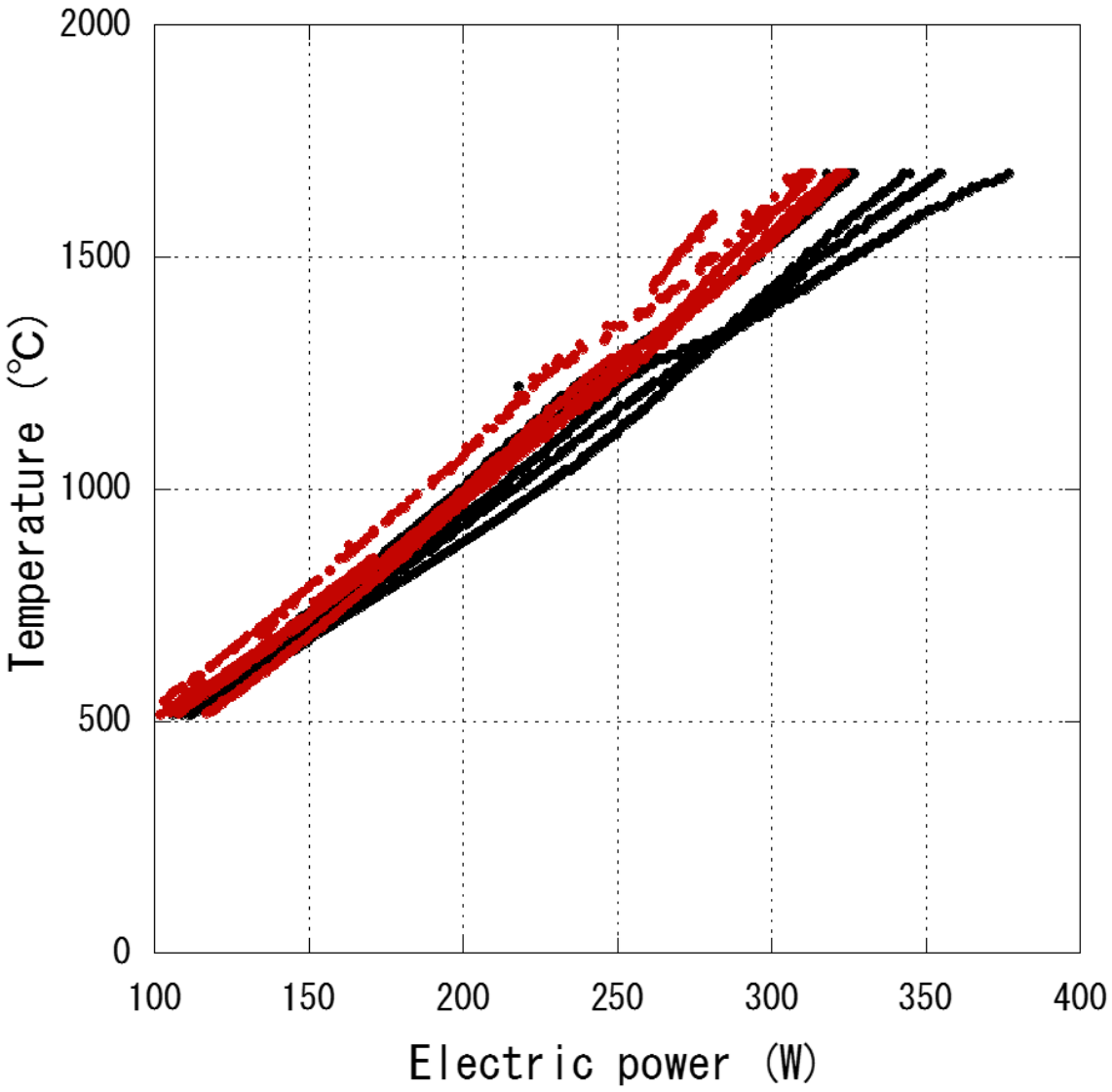

Fig. 2.3 Relationship between the electric power and temperature (red: Runs Py_1-42, black: Runs Py_43-55).

2.2.3. Analysis of recovered samples

The recovered samples were cut into two fractions. One of them was used for the water content and X-ray diffraction (XRD) measurements. Another part was polished into thin section using a diamond paste to examine the grain growth microstructures and the chemical compositions of existing phases.

Phases in recovered sample were determined by XRD measurements using a RINT RAPID II microdiffractometer installed at Kyushu University. The incident beam was Cu Kα radiation generated at 40 kV and 30 mA, and collimated to 300 μm in diameter. The exposure time was 10 minutes. The phase identification was also performed by using synchrotron radiation monochromatic X-ray at the beamline of NE-7 of Photon Factory.

Infrared spectra of recovered samples were measured using micro FT-IR spectrometer (FT/IR-4100 and IRT-3000, JASCO Co., Ltd.). The water contents were estimated based on the calibration (Paterson, 1982) as follows:

$$C_{OH} = \frac{X}{150\zeta} \int \frac{K(\nu)}{(3780 - \nu)}\, d\upsilon \qquad (2.17)$$

, where C_{OH} is the molar concentration of hydroxyl, ζ is an orientation factor which is 1/3, υ is the wavenumber, K (υ) is the absorption coefficient, X is an average density factor. The density factor is estimated by

$$X = \sum_i X_i \times f_i \qquad (2.18)$$

, where X_i is the density factor of i-th minerals, and f_i is the volume fraction of i-th minerals (Bolfan-Casanova et al., 2000).

We observed grain-growth microstructure and chemical mapping image using FE-SEM/EDS (JSM-7001F, JEOL Co., Ltd.) installed at Kyushu University. The analytical condition was 0.50-5.00 nA probe current, 10-15 kV accelerating voltage and 10.0 mm working distance. Chemical compositions of existing phases were examined by using FE-EPMA/EDS (JXA-8530F, JEOL Co., Ltd.) installed at Kyushu University. The analytical condition was 3.00 nA probe current, 15 kV accelerating voltage and 10.0 mm working distance.

2.3. Results

2.3.1. Phase identification and volume fractions of existing phases

Experimental conditions and results were shown in Table 2.2. Grain growth experiments were performed at 25-27 GPa and 1600-1950°C for 30-3000 minutes. Powder X-ray diffraction patterns of the recovered samples were shown in Fig. 2.4. Bridgmanite, ferropericlase, and majoritic garnet were identified in the sample annealed at 25 GPa (Fig. 2.4a). On the other hand, the 2 phases without majoritic garnet were present in the sample annealed at 27 GPa as shown in Fig. 2.4b. Ca-perovskite should exist at both pressures and we observed Ca-rich phase in SEM observation as mentioned later. However, it is difficult to identify its presence because it becomes amorphous when decompression to room pressure. Thus, it was assumed that 4 phases and 3 phases existed in the grain growth experiments at 25 GPa, and 27 GPa, respectively.

Chemical compositions of existing phases in recovered samples at 25 GPa were summarized in Table 2.3. Chemical analyses were performed for the samples annealed for the longest durations at each temperature condition. These compositions were not obviously different from previous studies on the phase equilibrium in pyrolite composition (e.g., Nishiyama and Yagi, 2003). In the case of the grain growth experiments at 27 GPa, grain sizes of each phase were too small to measure chemical

compositions quantitatively.

Volume fractions of each phase were estimated from the chemical composition based on the mass balance calculation (Irifune et al., 1986). The mass balance was calculated from

$$S = \sum_i x_i C' \qquad (2.19)$$

, where S is the chemical composition of starting material, x_i is the weight fraction of each phase and C' is the composition of each element. In the calculation, the measured chemical compositions were used for bridgmanite, ferropericlase and majoritic garnet, and that of end member was assumed for Ca-perovskite (i.e., $CaSiO_3$). The results were summarized in Fig. 2.5. The volume fraction in the 3-phase system in the previous study (Nishiyama and Yagi, 2003) is also shown. The volume fractions were almost constant with temperature. It has been known that the volume fraction of majoritic garnet increases with temperature in the previous study (Nishiyama and Yagi, 2003). However, its tendency was not obvious in this study. Because the volume fraction of Ca-perovskite was rather small (about 3 vol %), we analyzed grain growth kinetics ignoring this phase in the following discussion.

Table 2.2 The experimental conditions and results

Run No.	P (GPa)	Temp. (℃)	duration (min)	microstructure	phases and mean grain size (μm)						Water content
					bridgmanite	N	ferro periclase	N	majoritic garnet	N	(wt ppm H_2O)
Py_28	25	1600	300	non-equigranular							
Py_32	25	1600	600	equigranular	1.39 (0.06)	393	1.13 (0.03)	216	1.47 (0.05)	48	
Py_39	25	1600	1200	non-equigranular							
Py_40	25	1600	3000	non-equigranular							
Py_41	25	1700	60	non-equigranular							228.4 (43.4)
Py_52	25	1700	300	equigranular	1.47 (0.04)	175	0.95 (0.02)	207	1.03 (0.06)	22	
Py_48	25	1700	600	equigranular	1.95 (0.05)	196	1.17 (0.02)	244	1.35 (0.03)	83	179.5 (112.3)
Py_46	25	1700	1200	equigranular	2.17 (0.04)	306	1.30 (0.03)	216	1.60 (0.05)	73	
Py_53	25	1700	3000	equigranular	2.47 (0.07)	146	1.38 (0.03)	122	1.61 (0.07)	20	665.7 (214.4)
Py_06	25	1800	6	non-equigranular							
Py_33	25	1800	30	equigranular	1.91 (0.05)	172	1.08 (0.03)	109	1.14 (0.08)	51	
Py_30	25	1800	60	equigranular	2.00 (0.07)	172	1.27 (0.04)	121	1.65 (0.05)	82	
Py_05	25	1800	300	equigranular	2.12 (0.06)	170	1.29 (0.04)	72	1.29 (0.07)	74	807.8 (300.0)
Py_08	25	1800	600	equigranular	2.35 (0.08)	120	1.29 (0.05)	64	1.79 (0.08)	30	
Py_51	25	1800	3000	equigranular	3.06 (0.06)	267	1.75 (0.04)	223	3.66 (0.19)	48	
Py_31	25	1950	6	non-equigranular							
Py_34	25	1950	30	equigranular	2.18 (0.06)	117	1.37 (0.06)	68	1.76 (0.20)	15	
Py_02	25	1950	60	equigranular	2.57 (0.07)	242	1.54 (0.04)	134	2.02 (0.20)	21	
Py_37	25	1950	300	equigranular	2.61 (0.05)	264	1.47 (0.03)	238	2.81 (0.14)	6	
Py_38	25	1950	600	equigranular	3.36 (0.09)	141	1.95 (0.04)	160	3.24 (0.17)	43	667.4 (215.1)
Py_23	27	1600	60	non-equigranular							
Py_55	27	1700	60	equigranular	0.65 (0.02)	180	0.47 (0.01)	201			
Py_19	27	1800	6	non-equigranular							
Py_4	27	1800	60	equigranular	2.24 (0.05)	185	1.17 (0.03)	131			696.7 (82.9)
Py_54	27	1800	600	equigranular	2.34 (0.08)	153	1.32 (0.04)	106			264 .1(103.1)

N: the number of measured grains of each phase.

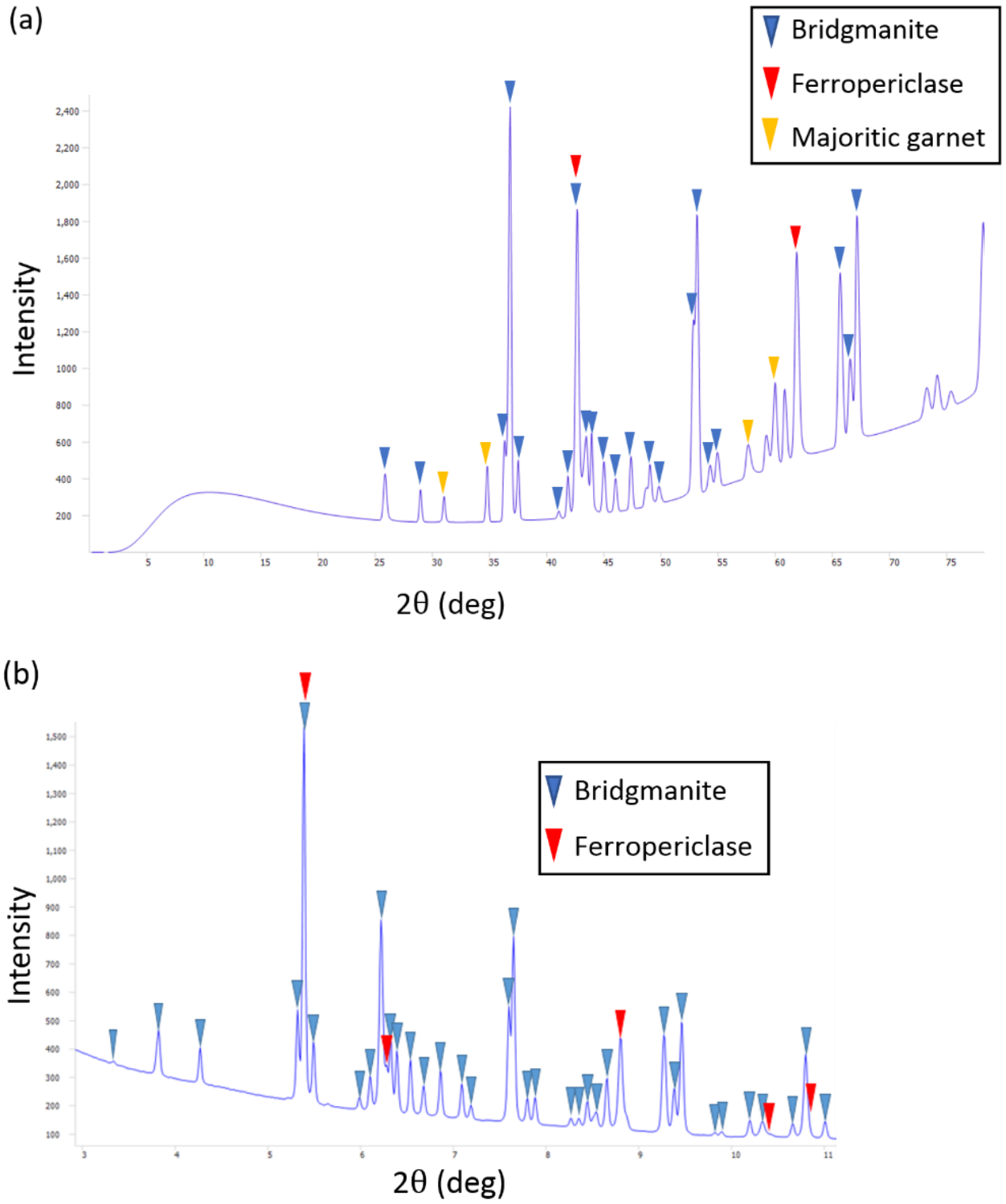

Fig. 2.4 XRD patterns of recovered samples (a: Run Py_37 at 25 GPa, b: Run Py_04 at 27 GPa)

Table 2.3 Chemical compositions of existing phase at 25 GPa

	Q304 (25 GPa, 1700°C, 50 h)						Q302 (25 GPa, 1800°C, 50 h)						Q259 (25 GPa, 1950°C, 10 h)					
	Brg (N=11)	S.D.	Fp (N=3)	S.D.	Mjgt (N=3)	S.D.	Brg (N=8)	S.D.	Fp (N=6)	S.D.	Mjgt (N=10)	S.D.	Brg (N=11)	S.D.	Fp (N=6)	S.D.	Mjgt (N=11)	S.D.
SiO_2	54.00	0.91	0.13	0.03	48.02	0.72	53.51	0.57	0.164	0.06	47.41	0.52	53.20	0.73	0.22	0.16	47.97	0.84
TiO_2	0.61	0.33	0.02	0.02	0.07	0.02	0.61	0.10	0.043	0.03	0.045	0.04	0.59	0.12	0.04	0.04	0.04	0.03
Al_2O_3	3.99	0.35	0.77	0.05	15.59	0.06	4.141	0.27	0.81	0.04	14.32	0.74	4.06	0.24	0.70	0.10	13.98	1.22
Cr_2O_3	0.47	0.09	1.32	0.08	0.81	0.06	0.451	0.07	1.249	0.04	0.865	0.05	0.48	0.06	1.24	0.03	0.80	0.06
FeO	5.28	0.45	23.05	0.48	4.07	0.14	5.637	0.25	24.25	1.01	4.042	0.13	5.59	0.33	24.16	0.17	4.21	0.48
MgO	36.13	0.70	69.47	1.34	25.51	0.33	36.38	1.09	68.04	3.08	27.31	1.06	34.93	0.92	70.27	0.51	27.26	1.53
NiO	0.08	0.06	2.04	0.18	0.03	0.04	0.073	0.04	1.814	0.15	0.066	0.05	0.08	0.05	2.05	0.18	0.07	0.06
CaO	0.85	0.73	0.09	0.03	4.26	0.14	0.625	0.09	0.058	0.03	3.865	0.10	0.67	0.10	0.06	0.03	4.36	0.35
Na_2O	0.06	0.02	2.04	0.18	1.12	0.05	0.049	0.03	1.019	0.05	0.986	0.04	0.05	0.03	0.96	0.07	0.87	0.099
Total	101.46		98.93		99.48		101.48		97.44		98.91		99.63		99.70		99.56	
N. O.	3		1		12		3		1		12		3		1		12	
Si	0.921	0.010	0.001	0.000	3.354	0.013	0.915	0.008	0.001	0.000	3.337	0.030	0.924	0.009	0.002	0.001	3.358	0.052
Ti	0.008	0.004	0.000	0.000	0.004	0.001	0.008	0.001	0.000	0.000	0.002	0.002	0.008	0.001	0.000	0.000	0.002	0.002
Al	0.006	0.001	0.008	0.001	0.045	0.003	0.006	0.001	0.008	0.000	0.048	0.003	0.007	0.001	0.007	0.000	0.044	0.004
Cr	0.080	0.007	0.007	0.000	1.284	0.019	0.083	0.006	0.007	0.000	1.188	0.061	0.084	0.005	0.006	0.001	1.153	0.097
Fe	0.075	0.007	0.149	0.002	0.238	0.011	0.081	0.004	0.159	0.002	0.238	0.009	0.081	0.004	0.154	0.002	0.246	0.029
Mg	0.919	0.013	0.803	0.003	2.656	0.005	0.927	0.021	0.795	0.004	2.865	0.101	0.902	0.019	0.801	0.003	2.846	0.169
Ni	0.001	0.001	0.013	0.001	0.002	0.002	0.001	0.001	0.011	0.001	0.004	0.003	0.001	0.001	0.013	0.001	0.004	0.004
Ca	0.016	0.013	0.001	0.000	0.319	0.007	0.011	0.002	0.000	0.000	0.292	0.008	0.015	0.005	0.000	0.000	0.327	0.026
Na	0.002	0.001	0.019	0.001	0.151	0.005	0.002	0.001	0.016	0.001	0.135	0.006	0.002	0.001	0.014	0.001	0.118	0.014
Total	2.03		1.00		8.05		2.03		1.00		8.11		2.023		1.00		8.10	
V. f.	0.73		0.14		0.10		0.74		0.13		0.10		0.74		0.15		0.09	

Brg: bridgmanite. Fp: ferropericlase. Mjgt: majoritic garnet. N. O.: Number of oxygens. S.D.: standard deviation. V. f.: volume fraction of each phase.

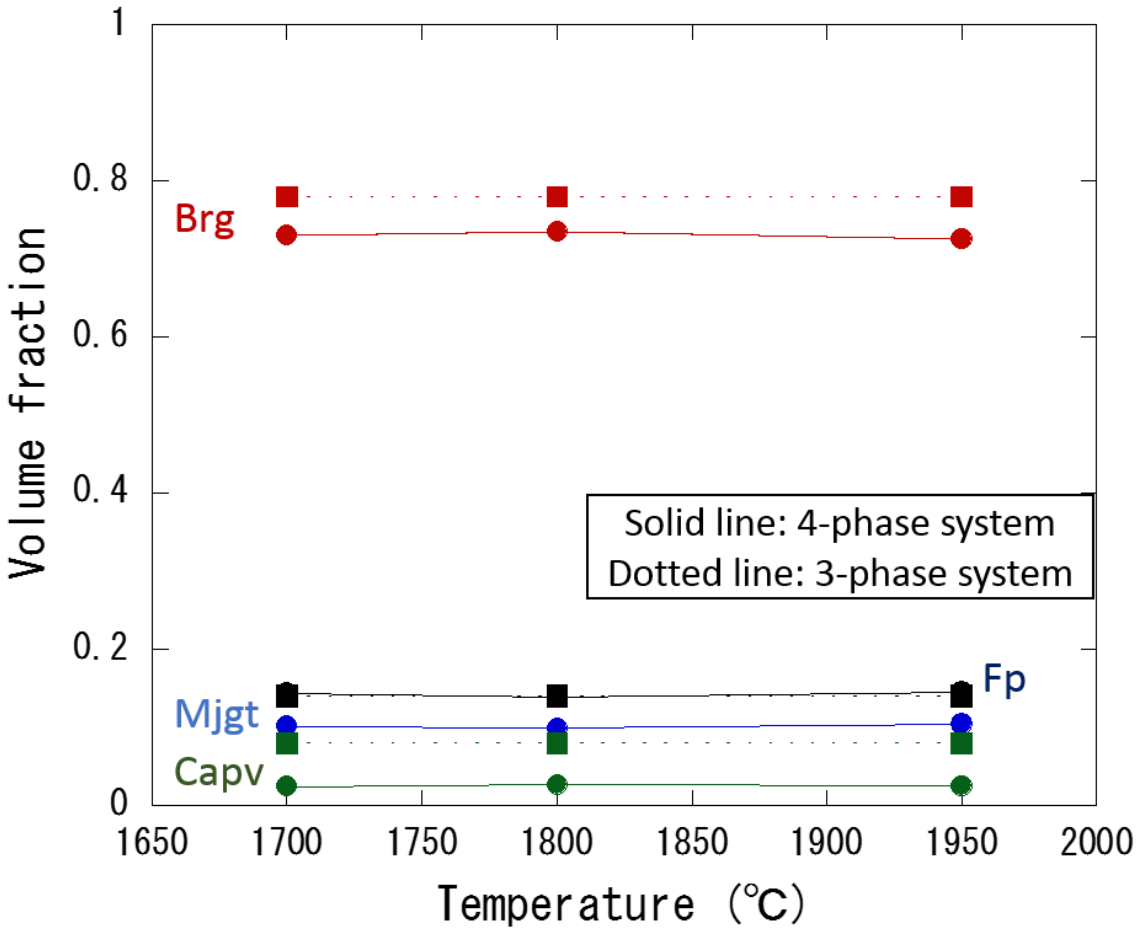

Fig. 2.5 Temperature dependence of volume fraction of each phase at 25 GPa (4-phase system, solid line). Those of the 3-phase system obtained in the previous study (Nishiyama and Yagi, 2003) are also shown (dotted line).

2.3.2. Grain-growth microstructures and grain size distributions

Fig. 2.6 compares grain growth microstructures of recovered samples with time and temperatures. The samples recovered in a short duration annealing at each temperature (Runs Py_06, Py_19, Py_23, Py_28, Py_31, Py_39-41) show non-equigranular heterogeneous textures, which is possibly affected by the eutectoid post-spinel transformation (Fig. 2.6a). These heterogeneous textures were diminished in longer annealing runs, and equigranular microstructures were achieved in 300 minutes at 1700°C and 30 minutes at 1800-1950°C (Fig. 2.6b-d).

Figs. 2.7 and 2.8 show BSE images and chemical mapping images of Mg, Ca, and Al elements of recovered samples at 25 and 27 GPa, respectively. The light grains are identical to ferropericlase in the BSE image, whereas, the dark grains are either bridgmanite or majoritic garnet, but could not be distinguished from the BSE image. Because of this, the Al chemical mapping was used to distinguish bridgmanite from majoritic garnet (Fig. 2.7c). Similarly, the Ca chemical mapping indicates the distributions of amorphous Ca-perovskite (Fig. 2.7d). Similar equigranular texture was observed in the sample recovered at 27 GPa (Fig. 2.8a). There are no Al rich grains in Fig. 2.8b, suggesting the absence of majoritic garnet at 27 GPa (i.e., 3 phase system). In both 3 and 4 phase systems, the minor phases (ferropericlase, Ca-perovskite, and

majoritic garnet) were distributed at the grain boundary of the major phase (bridgmanite), suggesting that the Ostwald ripening occurred by the grain-boundary diffusion.

The grain size of each grain was estimated from the diameter of the equivalent area circle by using the following equation (e.g., Sauveur, 1894; Jeffries et al., 1916; Takayama, 1994).

$$d_i = 2\sqrt{S_i/\pi} \tag{2.20}$$

, where d_i is the grain size of the i-th grain, S_i is the area of the i-th grain, and π is the circle ratio. Similarly, the average grain sizes of each phase were estimated from the average areas of each phase based on the following equation.

$$d_{av} = 2\sqrt{\Sigma_n S_i/N\pi} \tag{2.21}$$

, where d_{av} is the average grain size of each phase and N is the number of measured grains of each phase. The areas of each grain were measured from BSE images using a software of ImageJ after drawing the areas of each phase by Inkscape (Fig. 2.9). The grain size of Ca-perovskite could not be measured because the pores were usually present near the Ca-rich regions. The average grain size was estimated from more than 100 grains for bridgmanite and ferropericlase, and less than 100 grains for majoritic garnet.

The normalized grain size distributions of each phase were shown in Fig. 2.10. The value of d/d_{av} is less than 2. The grain size distributions were gaussian-like shaped and did not change with temperatures and times. Therefore, it is inferred that normal grain growth occurred in our study (Ardell, 1972).

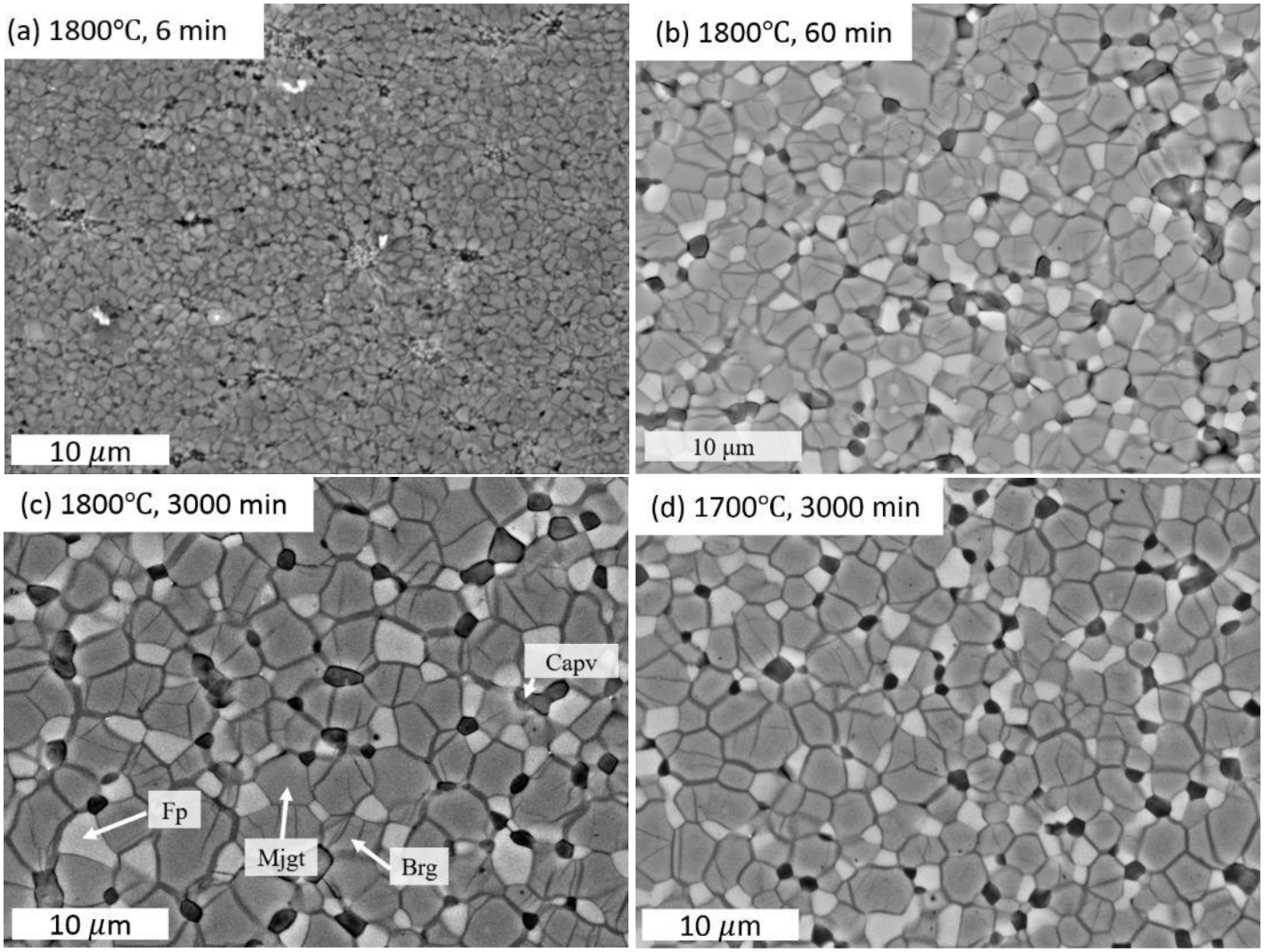

Fig. 2.6 Grain-growth microstructures of the recovered samples (BSE images) annealed at 25 GPa. The grain growth texture was heterogeneous at 25 GPa and 1800°C for 6 minutes (a). It became homogeneous and equigranular with time and temperature (b-d). The light grains were ferropericlase and the dark grains were bridgmanite or majoritic garnet.

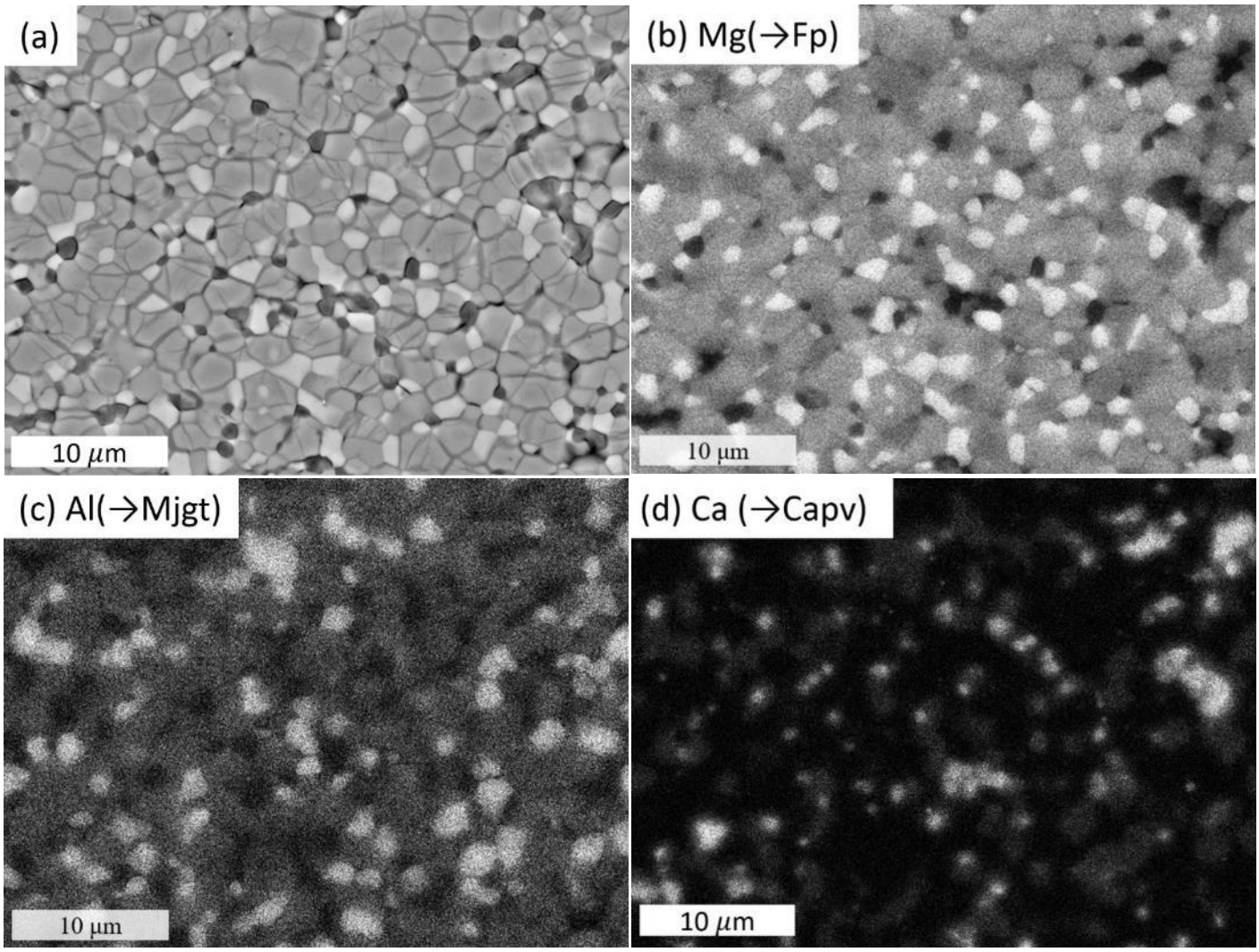

Fig. 2.7 BSE image (a) and Mg (b), Al (c), and Ca (d) chemical mapping images of the recovered samples at 25 GPa (Run Py_30, 1800°C for 60 minutes). The Mg-rich grains were ferropericlase. The majoritic garnet can be distinguished from bridgmanite by comparing the BSE image with the Al chemical mapping image. Most of the Ca-rich phase was present at the pores in the BSE image.

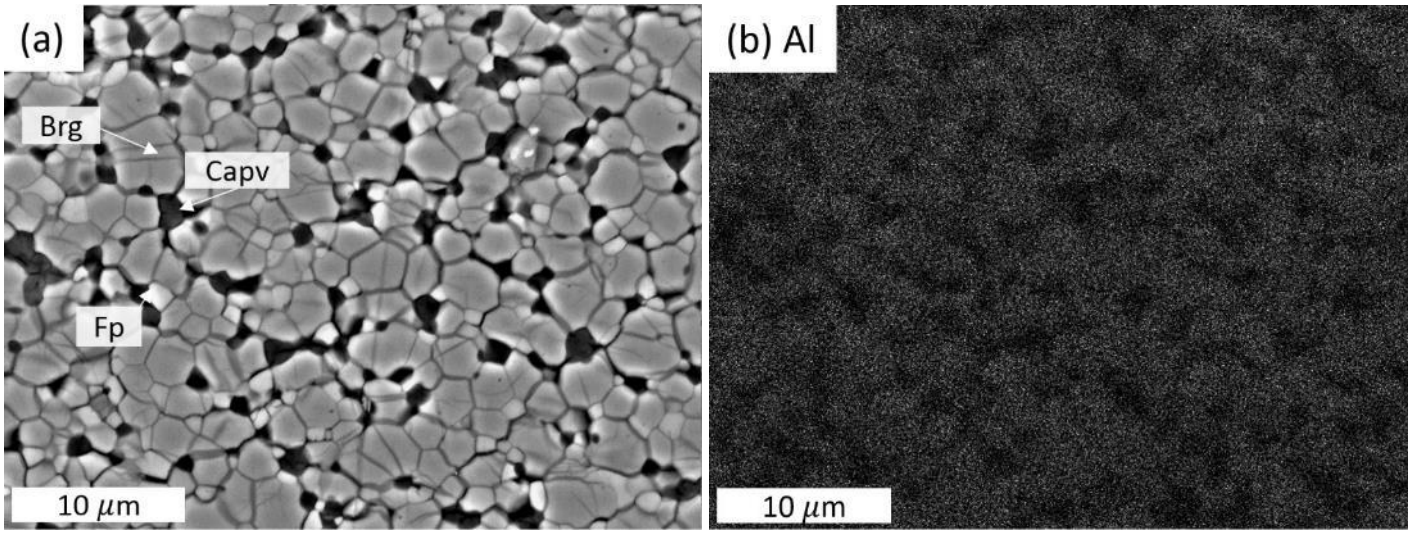

Fig. 2.8 BSE images (a) and Al mapping (b) of the recovered sample at 27 GPa (Run Py_04, 1800°C for 60 min). The Al rich grain were not observed, suggesting the absence of majoritic garnet at 27 GPa.

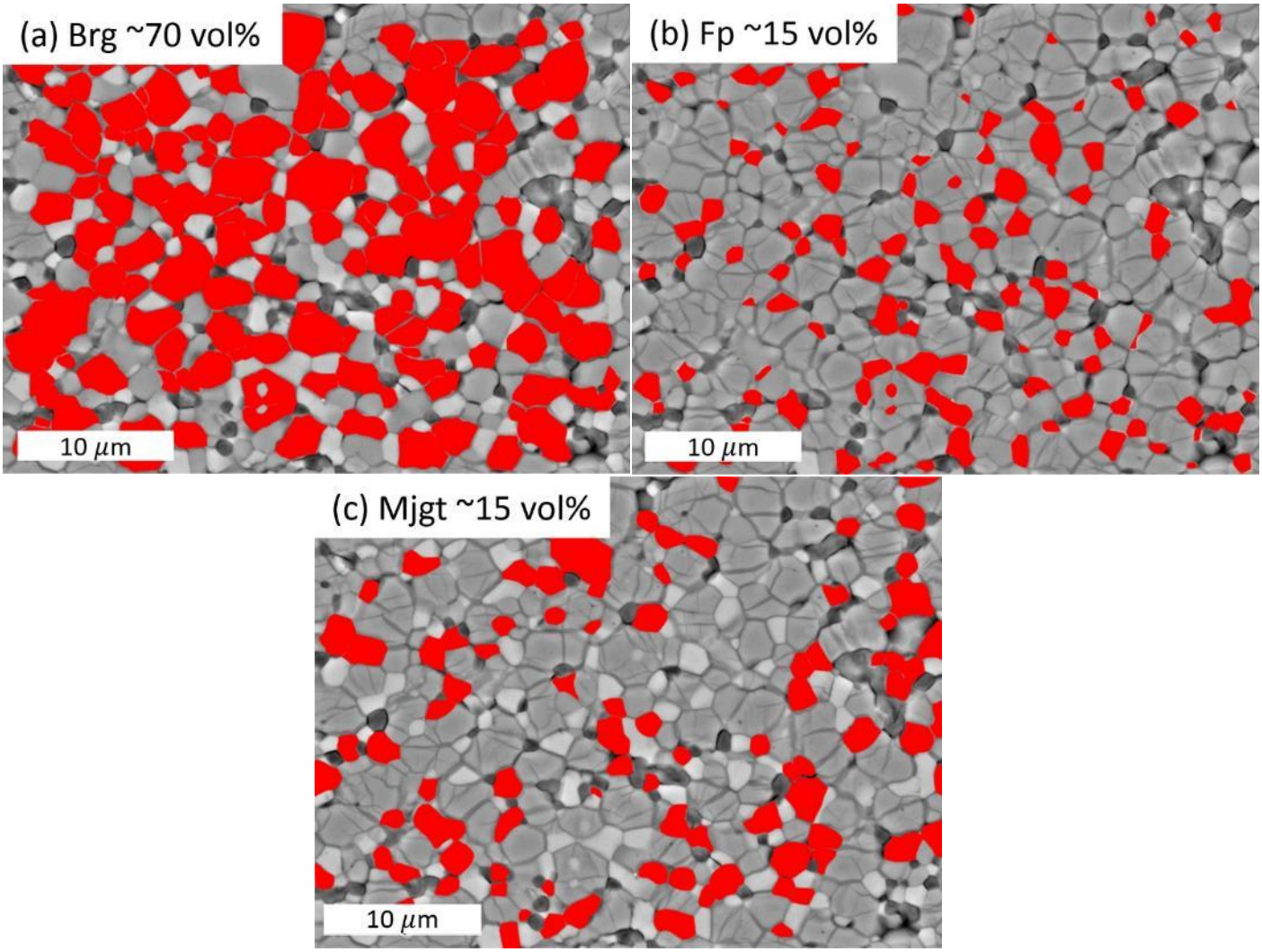

Fig. 2.9 Drawing the areas of each phase by the software of Inkscape (a: bridgmanite, b: ferropericlase, c: majoritic garnet).

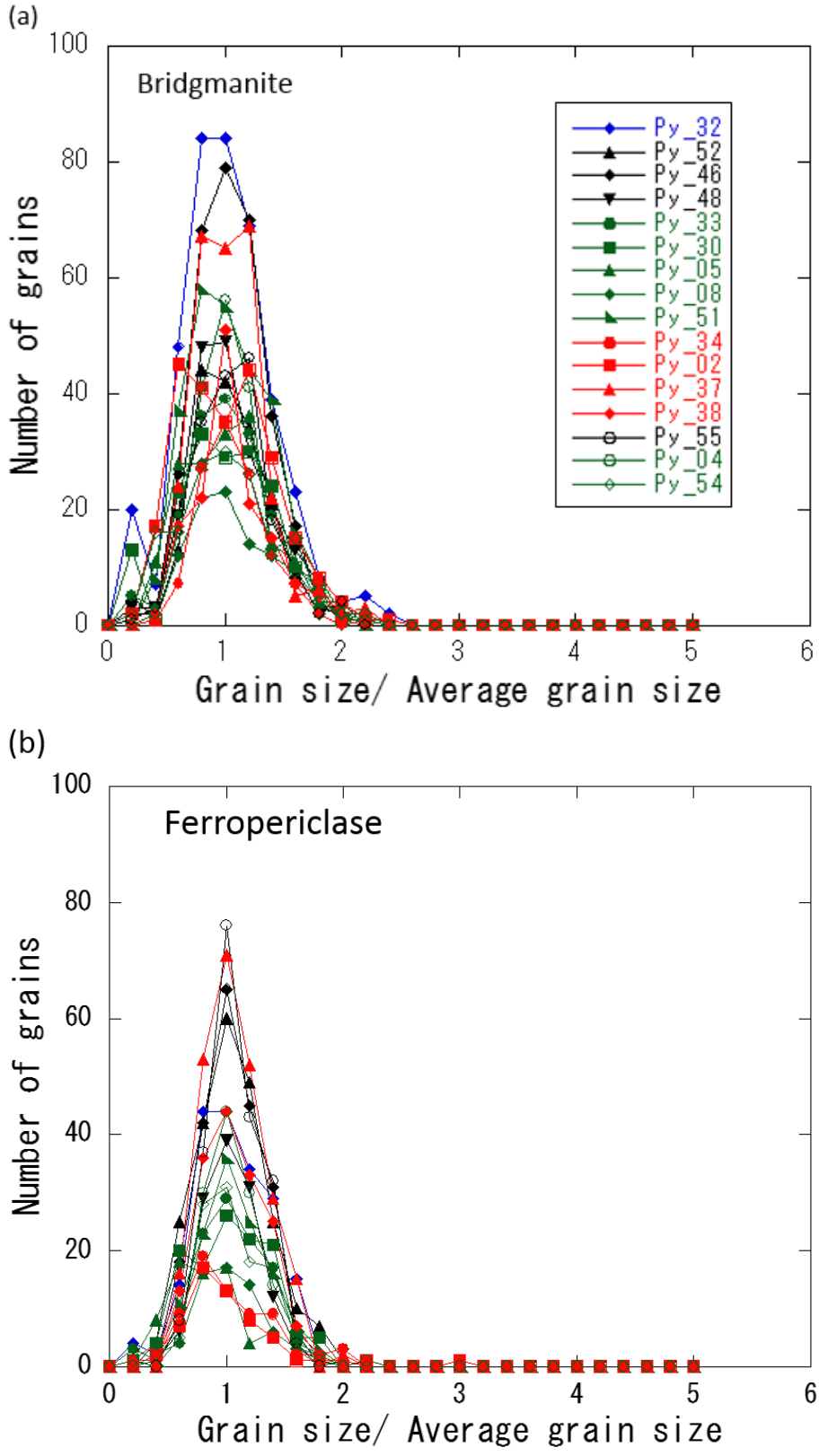
(a)
Bridgmanite
Number of grains
Grain size/ Average grain size
Py_32
Py_52
Py_46
Py_48
Py_33
Py_30
Py_05
Py_08
Py_51
Py_34
Py_02
Py_37
Py_38
Py_55
Py_04
Py_54
(b)
Ferropericlase
Number of grains
Grain size/ Average grain size

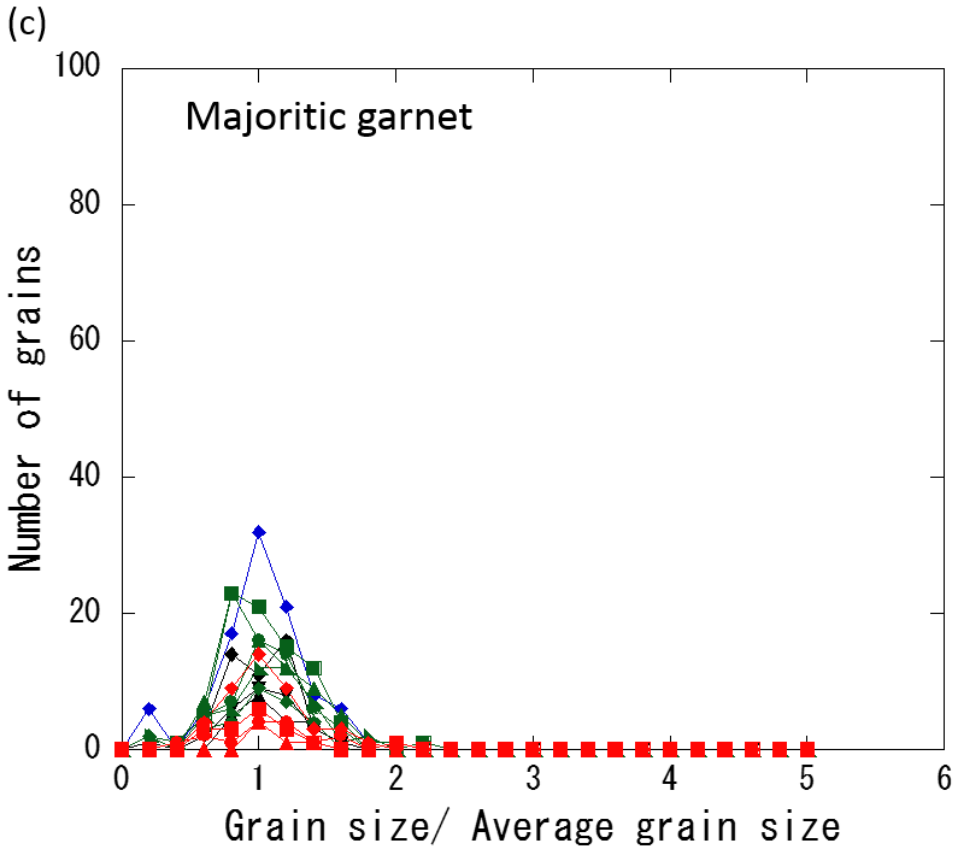

Fig. 2.10 Normalized grain size distributions of bridgmanite (a), ferropericlase (b) and majoritic garnet (c) (solid symbol: 25 GPa, Open symbol: 27 GPa, blue: 1600°C, black: 1700°C, green: 1800°C, red: 1950°C, circle: 30 min, square: 60 min, upward triangle: 300 min, diamond: 600 min, downward triangle: 1200 min, right-angled triangle: 3000 min).

2.3.3. Water contents

Infrared spectra of recovered samples are shown in Fig. 2.11. Broad absorption peak around 3400 cm^{-1} was generally observed in this study. Water contents estimated from the Paterson calibration (eq. 2.17) varied from ~180 to 810 wt. ppm H_2O (Table 2.2). We did not observe any systematic changes in water contents with temperatures and heating durations

Water contents of bridgmanite, ferropericlase, and majoritic garnet has been measured by Infrared spectroscopy and SIMS measurements in the previous studies (e.g., bridgmanite: Meade et al., 1994; Keppler et al., 1994; Bolfan-Casanova et al., 2000; Murakami et al., 2002, (ferro-)periclase: Bolfan-Casanova et al., 2000; Murakami et al., 2002; Keppler et al., 2007, majoritic garnet: Bolfan-Casanova et al., 2000; Katayama et al., 2003). Infrared spectra of bridgmanite showed broad absorption peak of ~3400 cm^{-1}, and relatively sharp absorption peaks of ~3300, 3400, 3500 and 3600 cm^{-1} (Meade et al., 1994, Keppler et al., 1994, Murakami et al., 2002). Absorption peaks for single crystal ferropericlase were present at 3620, 3520, and 3400 cm^{-1} (Murakami et al., 2002). Broad and sharp peaks were observed in majoritic garnet at ~3450 and 3550 cm^{-1}, respectively (Bolfan-Casanova et al., 2000, Katayama et al., 2003). Thus, the broad absorption peak of ~3400 cm^{-1} observed in the recovered samples were thought to

be mainly contributed from bridgmanite.

The maximum water solubility in bridgmanite, ferropericlase and majoritic garnet have been estimated to be about 3600, 2500 and 1250 wt. ppm H_2O, respectively (e.g., Murakami et al., 2002; Katayama et al., 2003). It has been suggested that the actual water contents in the lower mantle is 100-1000 wt. ppm H_2O (e.g., Karato, 2011). The water contents in our samples are much smaller than the maximum solubility level, and may be comparable to the actual lower mantle conditions.

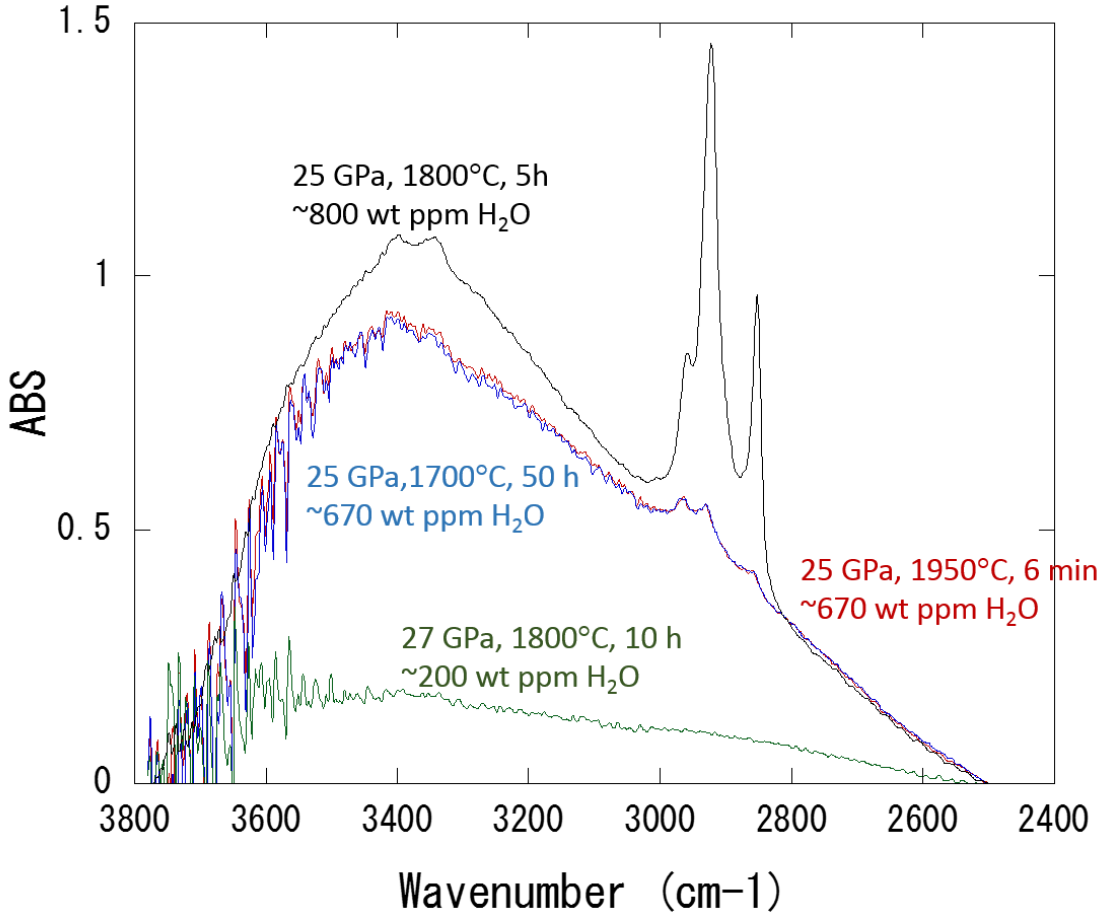

Fig. 2.11 Examples of FT-IR spectra measured in recovered samples. Experimental conditions and water contents estimated are also shown.

2.3.4. Grain growth kinetics in the 4-phase system

Grain sizes of each phase are plotted as a function of time in Fig. 2.12. Kinetic parameters (n, H^* and k_0) were estimated by fitting eq. 2.1 to the grain growth data in the 4-phase system. Kinetic parameters obtained are summarized in Table. 2.4, and the fitted curves are also shown in Fig. 2.12. The n values in each phase were not well constrained and contained large uncertainties. SEM observations indicated that the grains of minor phases are largely located at the grain boundary of the major phase of bridgmanite, in which the Ostwald ripening process is thought to be controlled by the grain-boundary diffusion. In this case, the n value is 4 as described in the previous section. Therefore, the grain growth data was also fitted assuming the n-value of 4 (Fig. 2.12 and Table 2.4). Grain growth data was also obtained in the 3-phase system as shown in Fig. 2.12. However, we do not have enough data to estimate kinetic parameters in the 3-phase system.

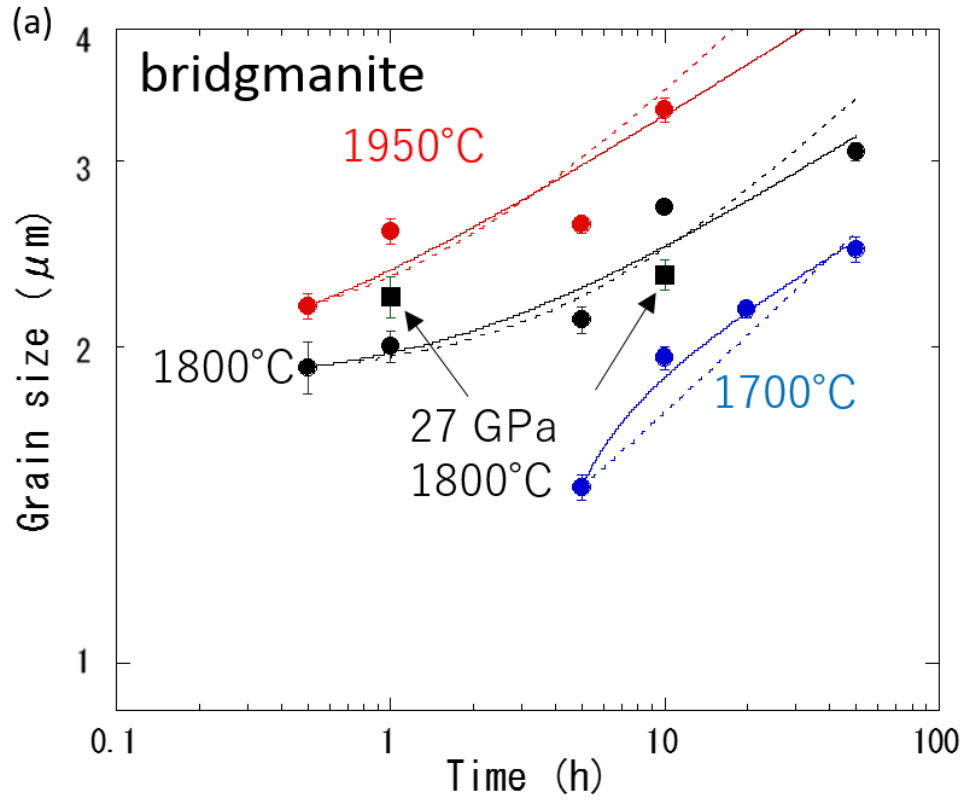
(a)
bridgmanite
1950°C
1800°C
27 GPa
1800°C
1700°C
Grain size (μm)
Time (h)
4
3
2
1
0.1
1
10
100

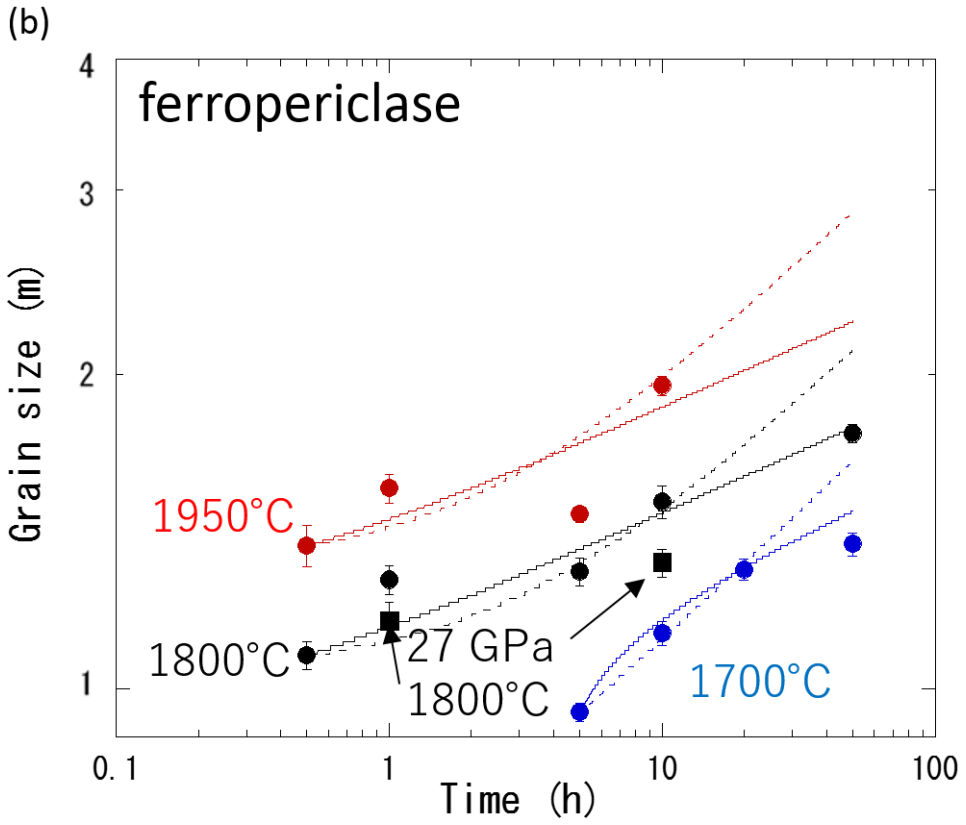
(b)
ferropericlase
1950°C
1800°C
27 GPa
1800°C
1700°C
Grain size (m)
Time (h)
4
3
2
1
0.1
1
10
100

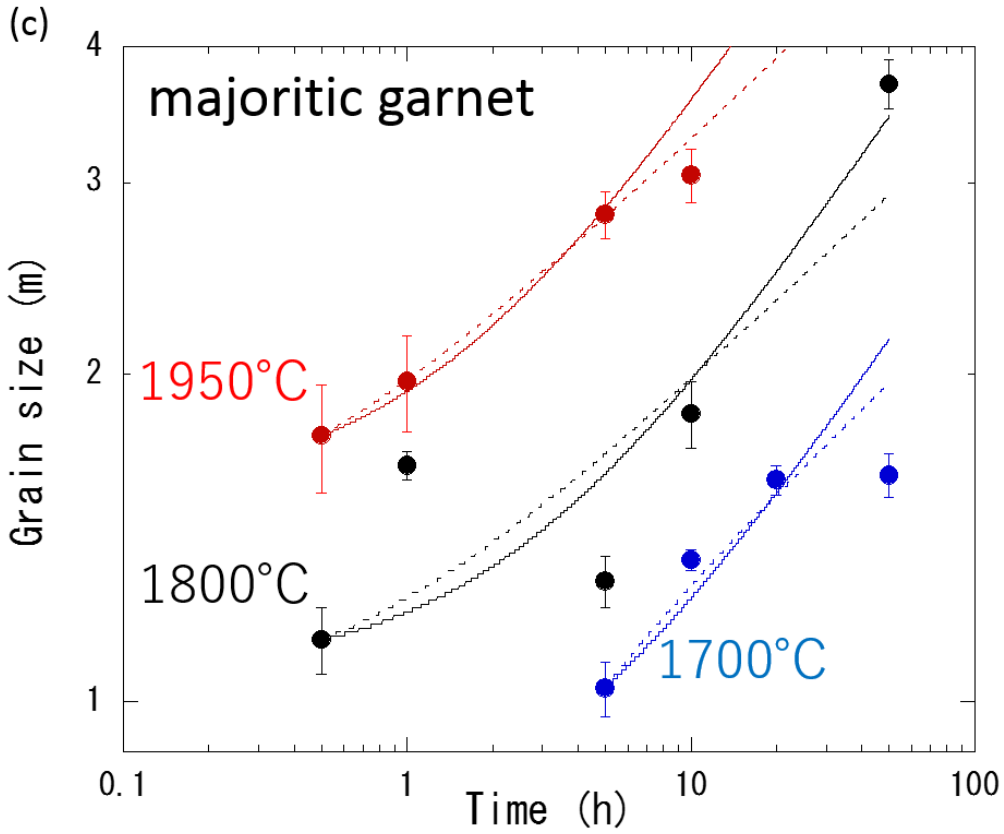

Fig. 2.12 Plots of grain size as a function of time (a: bridgmanite, b: ferropericlase, c: majoritic garnet). Results of the fitting by the rate equation for grain growth (eq. 2.1) were also shown (solid line: the *n* value was not fixed, dotted line: the n value was fixed to 4).

Table 2.4 Estimated values of parameters in grain growth kinetics

				n=4 fixed	
	n	log (k_0)	H^*	log (k_0)	H^*
Brg	6.7 (1.3)	-30.1 (-1.3)	472 (20)	-17.1 (-4.1)	396 (50)
Fp	8.4 (1.8)	-41.1 (-15.9)	501 (80)	- 20.0 (-16.0)	315 (99)
Mjgt	2.6 (0.5)	-8.9 (-2.8)	414 (100)	-14.1 (-3.9)	527 (150)

2.4. Discussion

2.4.1. Zener parameters

The Zener relationship was examined from our grain growth data in the 3- and 4-phase systems. It was assumed that Zener pinning effect on the grain growth of bridgmanite does not change by the kind of minor phase. The average grain size of the secondary phases was estimated from the following equation:

$$d_{II} = {(d_{Fp} * f_{Fp} + d_{Mjgt} * f_{Mjgt})}\Big/{(f_{Fp} + f_{Mjgt})} \quad (2.22)$$

, where d_{II} is the average grain size of the secondary phase, d_{Fp} is the grain size of ferropericlase, d_{Mjgt} is the grain size of majoritic garnet, f_{Fp} is the volume fraction of ferropericlase and f_{Mjgt} is the volume fraction of majoritic garnet. The relationship between the grain size of the major phase (bridgmanite) and that of the secondary phase (ferropericlase and majoritic garnet) is shown in Fig. 2.13. The grain size ratio between the major phase and the secondary phases ($d_{\mathrm{I}}/d_{\mathrm{II}}$) was estimated to be about 1.4 and 1.8 in the 4-phase and the 3-phase systems, respectively. It is thought that the larger value of the grain size ratio in the 3-phase system reflects the smaller volume fraction of the secondary phase.

Tasaka and Hiraga (2013) examined the relationship between the $d_{\mathrm{I}}/d_{\mathrm{II}}$ and the volume fraction of the secondary phase in olivine-enstatite system as shown in Fig. 2.14,

and determined Zener parameters (z and β) in eq. 2.7. Our data is also plotted in this figure. Although, it is difficult to estimate the Zener parameters only from the grain growth data obtained in the present study, our data is rather consistent with the previous study.

The z value depends on the location of the minor phase (e.g., Evans et al., 2001; Tasaka and Hiraga, 2013). The z value becomes 0.5 when the secondary phase is distributed on the grain boundary of the major phase. This texture was observed both in our study (Figs. 2.7, 2.8) and the study of Tasaka and Hiraga (2013). Therefore, it is reasonable to assume the z value of 0.5 in the multi-phase system treated in our study. The β value depends on the relative boundary energy (eq. 2.8). If we use the z value of 0.5, the β value was estimated to be 0.80 from the two data points. This value is almost similar to that obtained in the study of Tasaka and Hiraga (2013) within errors. Thus, the present study suggests that the Zener parameters obtained in the olivine-enstatite system can be applied to the 3- and 4-phase system in the pyrolitic composition under the lower mantle condition.

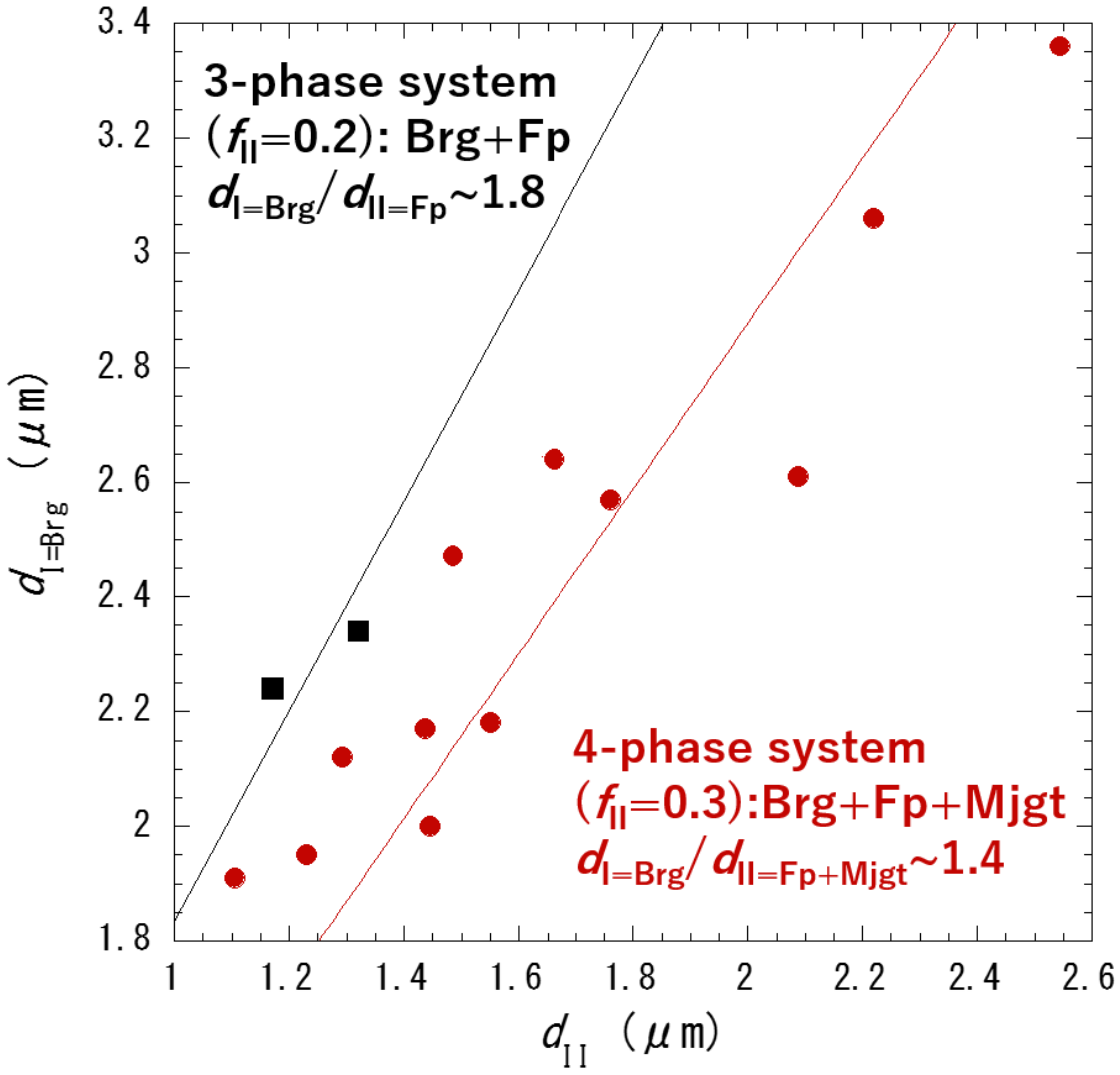

Fig. 2.13 Plots of the grain size ratio between the major and secondary phases against the grain size of the secondary phase.

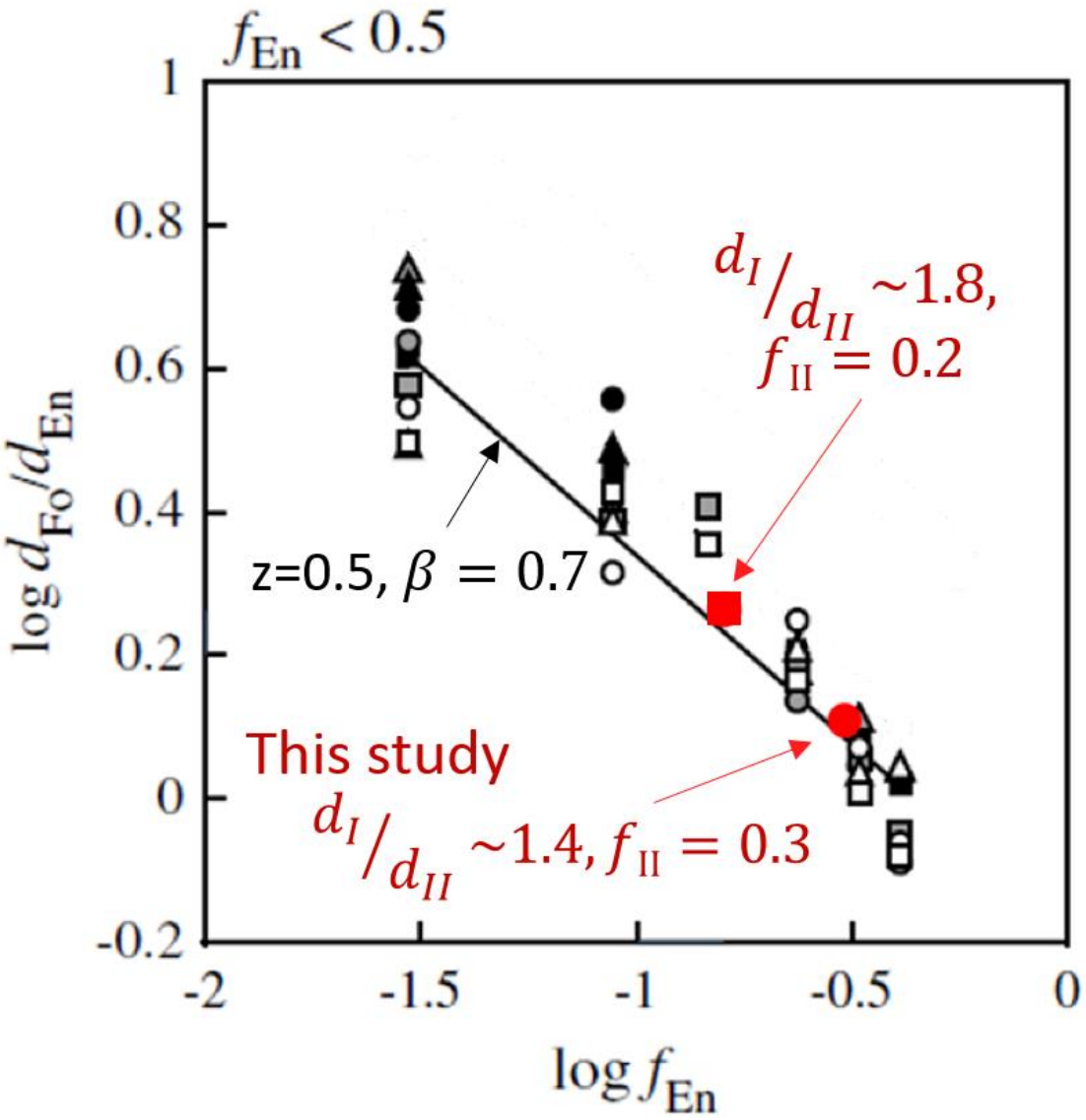

Fig. 2.14 Plots of the grain size ratio between the major phase (forsterite) and the secondary phase (enstatite) as a function of the secondary phase (modified from Tasaka and Hiraga, 2013). Our grain growth data obtained in the 3- (red circle) and 4-phase (red square) system is also shown.

2.4.2. Grain growth kinetics of bridgmanite in the 3-phase system

We observed the similar grain growth texture between the 3- and 4-phase systems, in which the pinning phase of ferropericlase was present at grain boundaries of bridgmanite (Figs. 2.7a and 2.8a). This suggests that the grain growth of ferropericlase occurs by the similar Ostwald ripening process controlled by the grain-boundary diffusion. Therefore, although the grain growth kinetics of ferropericlase in the 3-phase system could not be determined due to the limited number of the data point, it is likely to be same as that in the 4-phase system. Actually, the grain growth kinetics of minor phase do not change with the volume fraction of major phase in the olivine-enstatite system (e.g., Hiraga et al., 2010; Tasaka and Hiraga, 2013).

Assuming the same grain growth kinetics of ferropericlase both in the 3- and 4-phase systems, we can estimate the grain growth rate of bridgmanite in the 3-phase system from that of ferropericlase using the Zener relationship (eq. 2.15). An example for the case of $d_{0\,\mathrm{Fp}}$=1 μm at 1800°C is shown in Fig. 2.15 together with the two- data points obtained in the present study. In this way, we discuss the grain-size evolution in the lower mantle in the following sections although further experiments are needed to constrain the grain growth kinetics in the 3-phase system.

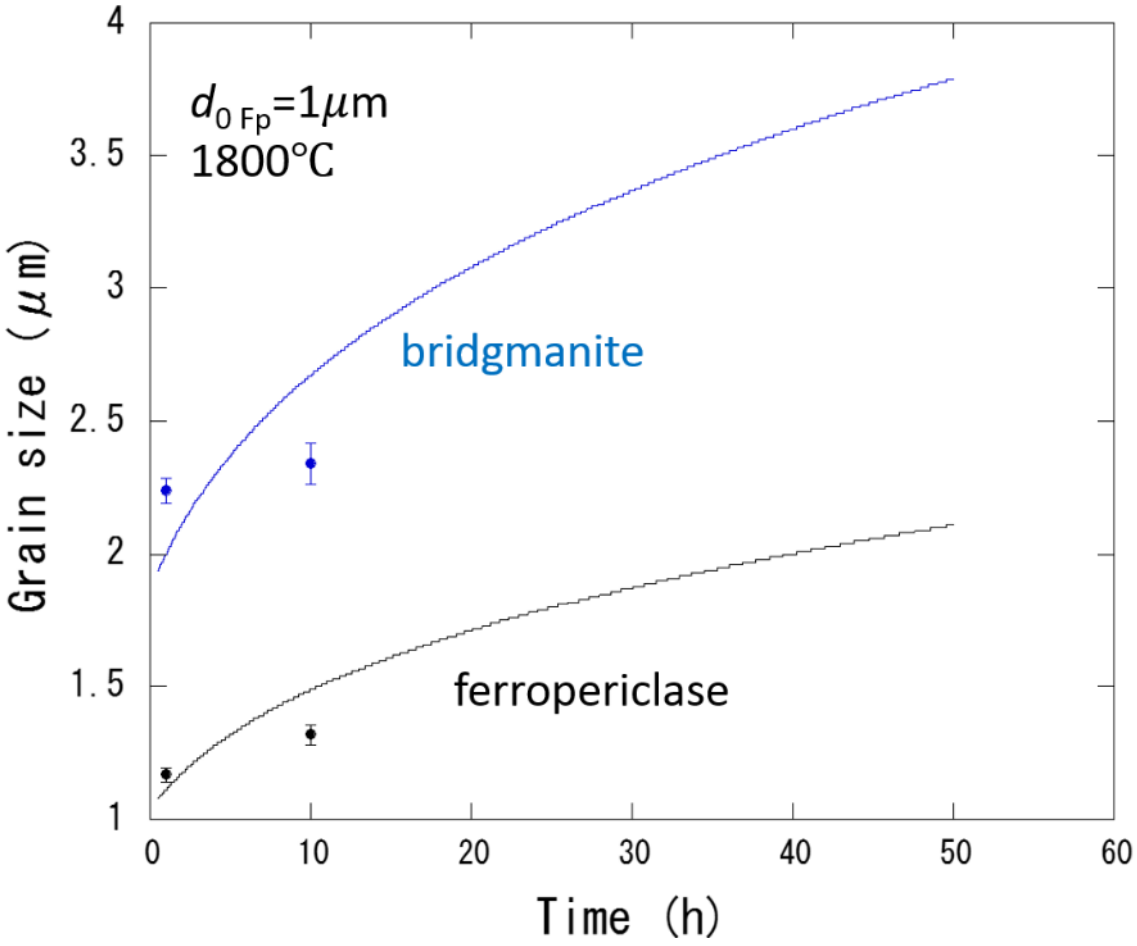

Fig. 2.15. Gain growth rate of bridgmanite and ferropericlase in the 3-phase system at 1800°C (solid line, blue: bridgmanite, black: ferropericlase) estimated from the grain growth kinetics of the secondary phase (ferropericlase) in the 4-phase system and the Zener relationship. Two data points obtained in this study are also shown (solid circles).

2.4.3. Grain-size evolution and deformation mechanisms in the lower mantle and lower-mantle slabs

This study demonstrated that the Ostwald ripening process controls the grain growth kinetics of the multi-phase system in pyrolitic composition under the lower mantle condition. In this case, the grain-size evolution of bridgmanite can be estimated from the grain growth kinetics of the secondary phase and the Zener parameters. On the basis of this principle, we calculated the grain-size evolutions of the two-phase systems of ferropericlase and bridgmanite were shown in Fig. 2.16. In this calculation, the grain growth kinetics of ferropericlase obtained in this study and the Zener parameters of z = 0.5 and β = 0.80 were used assuming the pyrolitic mantle (f_{II} = 0.2). We took the horizontal axis as the elapsed time after the material entering into the lower mantle through the post-spinel transformation. We assumed that the initial grain size of ferropericlase is 1 μm.

Fig. 2.16 shows that the grain size of bridgmanite is estimated to be about 10-200 μm for cold slab conditions at 800-1400°C in 2×10^7 years, and 500-3000 μm for surrounding mantle conditions at 1600-2400°C in 10^8 years. The critical grain size for between the two deformation mechanisms of diffusion creep and dislocation creep, which has been estimated on the basis of the Si diffusivity (Yamazaki et al., 2000 and

Xu et al., 2011), is also shown in this plot. Fig. 2.16 suggests that the grain size of bridgmanite is located around the boundary between these two deformation mechanisms in both cold slabs and surrounding mantle conditions. This implies that bridgmanite deforms by diffusion creep under the relatively low-stress conditions such as the most part of the lower mantle and lower-mantle slab. However, the deformation mechanism would change from the diffusion creep to the dislocation creep under the high-stress conditions such as the lower mantle around the subducting slabs and the D" layer. This is qualitatively consistent with the fact that seismic anisotropy has been observed only at limited regions in the lower mantle where the deformation is significant. Recently, on the basis of dislocation dynamics simulation, it has been suggested that grain-size-insensitive pure climb creep mechanism becomes dominant in bridgmanite when the grain size is larger than 100 μm (Boioli et al., 2017). Although we ignore this mechanism in this discussion due to still limited experimental evidences, this needs to be considered in future studies.

The volume fraction of the secondary phase depends on the chemical composition of the lower mantle, which is still under debate. The volume fraction of ferropericlase may also vary across regions in the lower mantle, which may result in the viscosity variations through the changes in the grain-size evolution. The effects of the

ferropericlase contents on the grain-size evolution of bridgmanite are examined on the basis of the Zener relationship in Fig. 2.17.

The volume fractions of ferropericlase in chondritic, pyrolitic, and olivine mantle models are ~0.1, ~0.2, and ~0.3, respectively. Fig. 2.17 suggests that, as can be seen from the Zener relationship, the grain size of bridgmanite increases with decreasing in the ferropericlase fraction, however its effect is not so large. Therefore, the effects of the lower-mantle composition on the viscosity variation is thought to be limited although the two-phase rheology with the interconnection of the weaker phase of ferropericlase is not considered in this study.

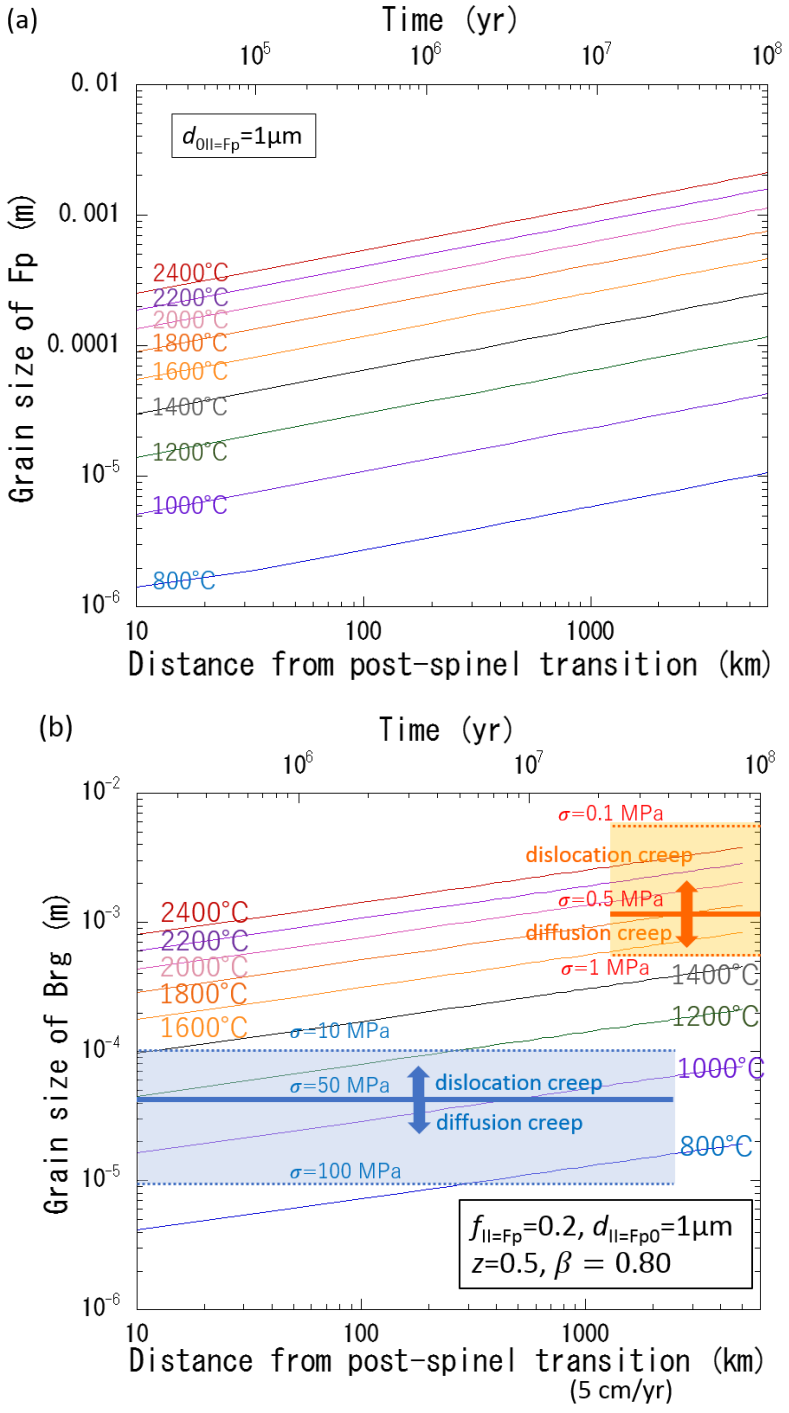

Fig. 2.16 Grain-size evolution of ferropericlase (a) and bridgmanite (b) after the material entering into the lower mantle. The critical grain size between diffusion and dislocation creep (e.g., Yamazaki et al., 2000; Xu et al., 2011) is also shown.

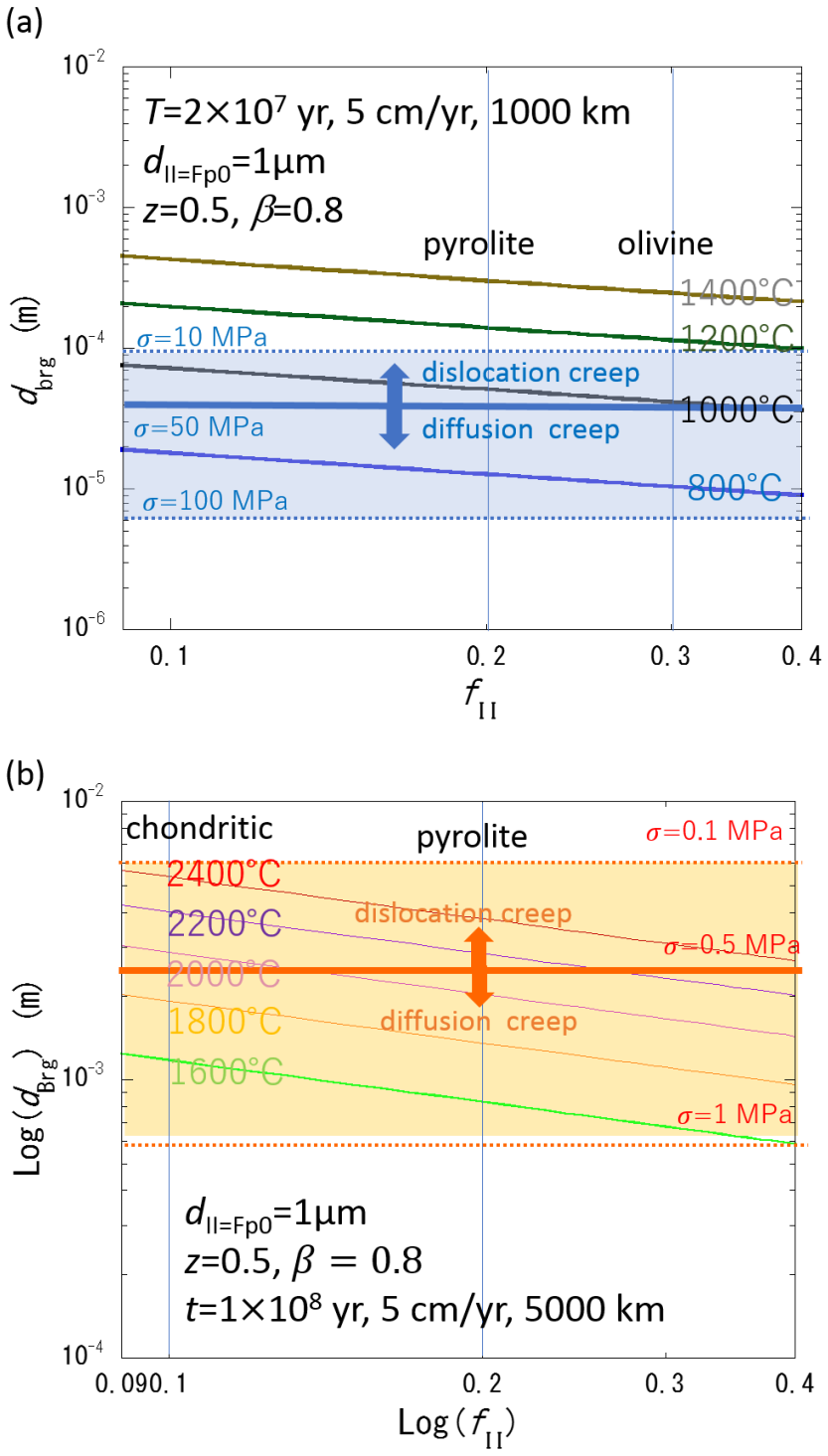

Fig. 2.17 Effects of the volume fraction of the secondary phase (ferropericlase) on the grain-size evolution of bridgmanite under the lower-mantle slab (a) and the lower mantle (b) conditions.

2.4.4. Rate-controlling process and grain-boundary diffusivity

The grain growth in our multi-phase system is controlled by the Ostwald ripening of secondary phase of ferropericlase. This process requires the grain deformation in the major phase of bridgmanite, which can be achieved by the faster process between the diffusion creep of bridgmanite or the interfacial reaction between bridgmanite and ferropericlase (e.g., Hiraga et al., 2016; Okamoto and Hiraga, 2018). If the former is the case, the rate of the Ostwald ripening of ferropericlase is controlled by slowest diffusion species not only in ferropericlase but also in bridgmanite. Previous diffusion studies have revealed that the Si diffusivity in bridgmanite is the slowest among these diffusion species (e.g., Yamazaki et al., 2000; Van Orman et al., 2003; Xu et al., 2011) and thus controls the Ostwald ripening of ferropericlase.

On the other hand, the interfacial reaction between $MgSiO_3$ bridgmanite and MgO periclase can be schematically shown in Fig. 2.18, in which bridgmanite dissolves at the interface of A, and precipitates at the interface of B. These reactions are described as follows:

A $$MgSiO_3 + V''''_{Si} + 2V^{\cdot\cdot}_O = Si_{Si}^{\times} + 2O_O^{\times} + MgO \quad (2.23)$$

B $$Si_{Si}^{\times} + 2O_O^{\times} + MgO = MgSiO_3 + V''''_{Si} + 2V^{\cdot\cdot}_O \quad (2.24)$$

, where V''''_{Si} and $V^{\cdot\cdot}_O$ are the atomic vacancies of Si and O, respectively, and $Si_{Si}^{\times}$ and

$O_O^{\times}$ are the atoms of Si and O, respectively. Thus, the Si diffusivity in bridgmanite also controls the interfacial reaction. As seen from the above considerations, the grain growth in the bridgmanite-ferropericlase system is likely to be controlled by the Si diffusion in bridgmanite.

The grain-boundary diffusivity controlling the grain growth can be estimated from $k_{4,\mathrm{II=fp}}$ based on eq. 2.16. We used the following parameters in the calculation (w = 1 nm, γ = 2 J/m^2, υ = 0.6-1.0, and c = 40900 mol/m^3. G = 0.35 was taken from the olivine-enstatite system in Tasaka and Hiraga, 2013). The rate-controlling grain-boundary diffusivity deduced from our experiments is compared with atomic diffusivities in bridgmanite as shown in Fig. 2.19.

In previous studies, volume and grain-boundary diffusion coefficients of Si, Mg, and O were measured in bridgmanite (volume diffusion of Si and Mg: Xu et al., 2011; O volume diffusion: Dobson et al., 2008; Si grain-boundary diffusion: Yamazaki et al., 2000; Mg grain-boundary diffusion estimated from the diffusion-controlled growth kinetics: Nishi et al., 2013). The high-pressure experiments were conducted under dry conditions in the study of Xu et al. (2011) (3-10 wt ppm H_2O) and Nishi et al. (2013) (~3.5 wt ppm H_2O). Water contents of the sample in other studies are unknown. Fig. 2.19 indicates that the grain-boundary diffusivity inferred from our study is much

faster than the volume diffusion rates of Si, Mg and O in bridgmanite.

On the other hand, the grain-boundary diffusivity of this study is roughly consistent with Mg grain-boundary diffusion rate (Nishi et al., 2013), but is larger than Si grain-boundary diffusion rate (Yamazaki et al., 2000). The reason for the discrepancy between the grain-boundary diffusivity of our study and the Si grain-boundary diffusivity is not clear. Water contents of the sample in our study may be larger than that in the study of Yamazaki et al. (2000) although the latter is unknown. Bridgmanite in our experiments contains various chemical components such as Fe and Al, whereas pure $MgSiO_3$ was used in Yamazaki et al. (2000). These factors may enhance the grain-boundary diffusivity in our study, however further studies are needed to clarify the reason.

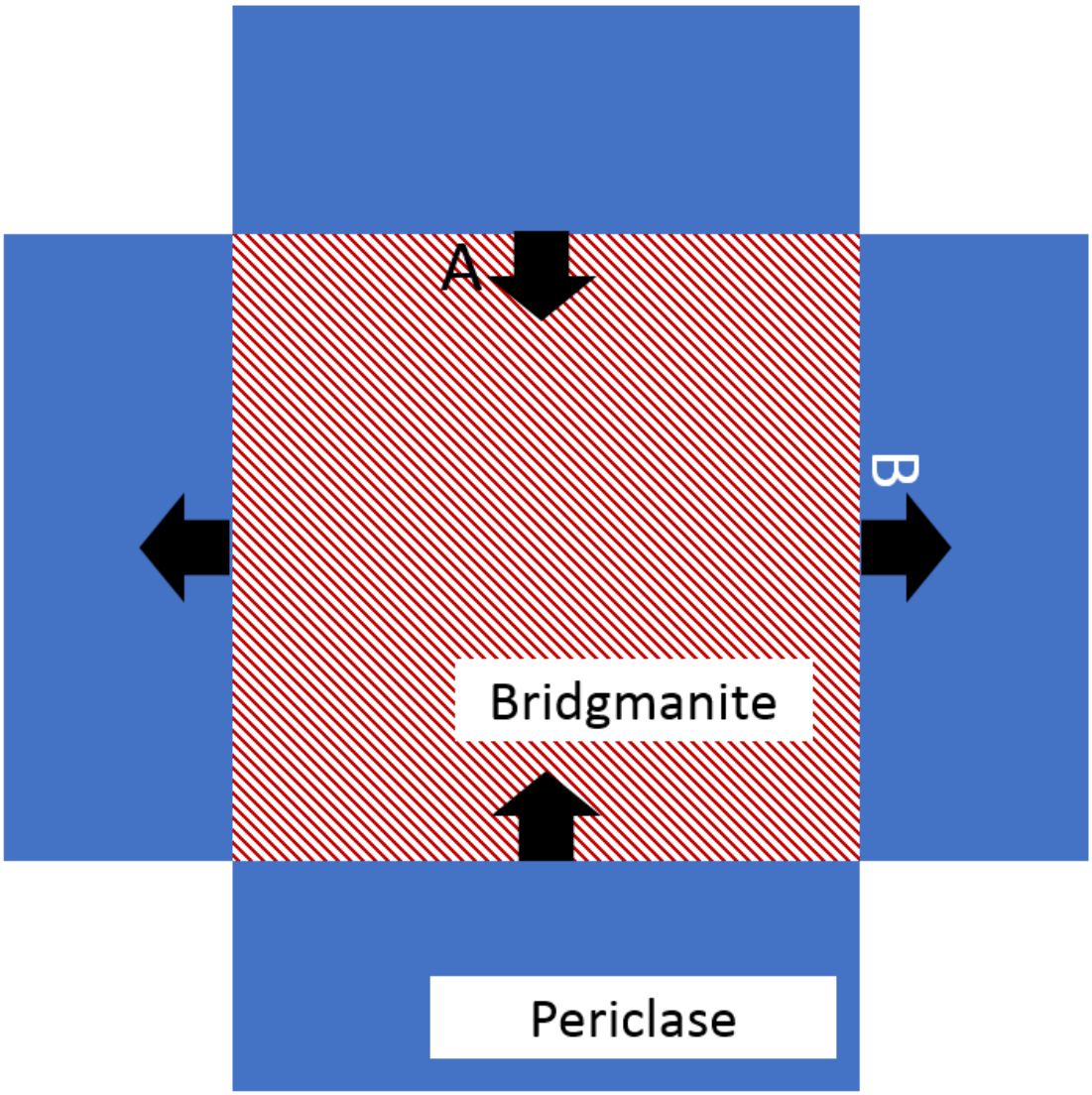

Fig. 2.18 The grain deformation in bridgmanite by the interfacial reaction during grain growth (red meshed area: bridgmanite, blue area: periclase). The reactions at the interface A and B are given in eq. 2.23 and 2.24. The black arrows show the direction of the deformation in bridgmanite by these reactions.

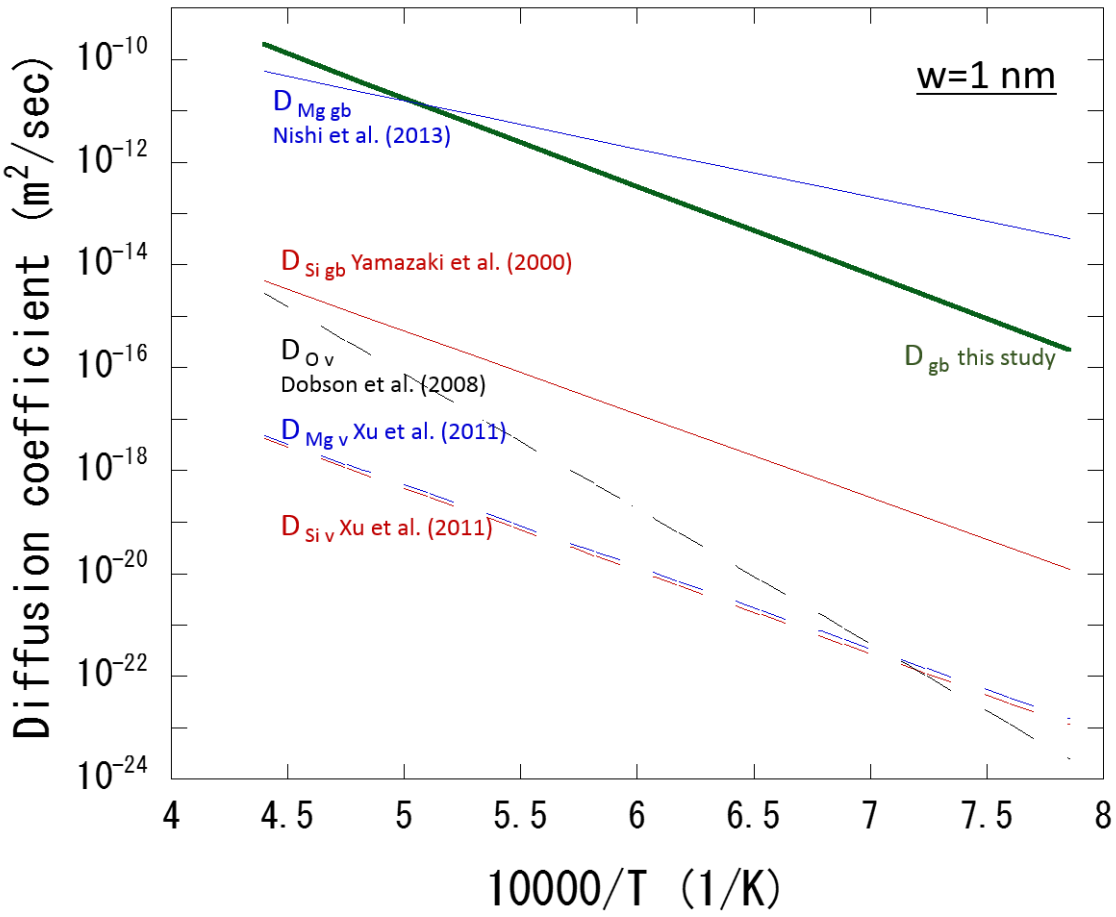

Fig. 2.19 Arrhenius plots of atomic diffusivity of Si (red), Mg (blue), and O (black) in bridgmanite (solid line: grain-boundary diffusion, dashed line: volume diffusion). The grain-boundary diffusivity inferred from the grain growth kinetics of this study is shown in green. The grain-boundary diffusivity is calculated using the grain-boundary width of 1 nm.

2.4.5. Viscosity variations in the lower mantle inferred from the grain growth kinetics

Hiraga et al. (2016) demonstrated that the rate-controlling process is common between the grain growth and diffusion creep in the olivine-enstatite system. They systematically examined grain growth kinetics and the flow law of diffusion creep in this two-phase system at room pressure, and revealed that both processes are controlled by effective diffusion of Mg. This has been also confirmed in the olivine-periclase two-phase system, in which the Si effective diffusion controls both grain growth rate and diffusion creep rate (Okamoto and Hiraga, 2018). On the basis of these pioneering works, we discuss the viscosity of the lower mantle from our results on the grain growth kinetics in pyrolitic material.

Diffusion creep viscosity can be calculated from effective diffusion rate as follows:

$$\dot{\varepsilon} = A\sigma \frac{D_{\mathrm{eff}}}{d^2} \frac{V}{RT} \tag{2.25}$$

$$D_{eff} = D_{\mathrm{v}} + \frac{\pi w}{d} D_{\mathrm{gb}} \tag{2.26}$$

$$\eta = \frac{\sigma}{\dot{\varepsilon}} = \frac{1}{A} \frac{d^2}{D_{eff}} \frac{RT}{V} \tag{2.27}$$

, where A is constant (=13.3), σ is the stress, D_{eff} is the effective diffusion coefficient of the rate controlling element (e.g., Frost and Ashby, 1982). We estimated the diffusion creep rate of bridgmanite condition considering the diffusivity obtained from the grain

growth kinetics.

In this study, only the grain-boundary diffusion rate was obtained from the grain growth experiments in relatively fine-grained materials. However, the volume diffusion may also become dominant with increasing the grain size. The effective diffusion rate of Si in bridgmanite was estimated by combining the grain-boundary diffusion rate of this study with the volume diffusion rate (Xu et al., 2011) as shown in Fig. 2.20. As mentioned in the previous section, the grain-boundary diffusion is much faster than the volume diffusion (Fig. 2.19). Fig. 2.20 suggests that the grain-boundary diffusion is still effective in the bulk diffusivity of polycrystalline material over the grain size of ~10 mm. This is contrast to the result of the previous study (Yamazaki et al., 2000) in which the volume diffusion becomes dominant when the grain size is larger than ~100 μm.

The pressure effect on the diffusivity is also important because the pressure increase in the lower mantle is quite large ~100 GPa. There have been few studies of the effects of pressure on the diffusivity under the lower mantle conditions. Nishi et al. (2013) reported the activation volume of ~3.8 cm^3/mol for the Mg grain-boundary diffusion in bridgmanite at the pressures of 24-50 GPa although it may decrease with increasing pressure. Yamazaki and Karato (2001) considered the pressure effect on the

viscosity based on the homologous temperature scaling, in which the effect becomes small with increasing pressures. We used the apparently constant activation volume of ~1.7 cm^3/mol taking from their study.

Firstly, we estimated viscosity variations of the down welling material across the 660 km discontinuity as shown in Fig. 2.21 considering the grain-size evolution discussed in Fig. 2.16. The viscosities are estimated to be $10^{20.5\text{-}18.2}$ Pas at the depth of ~1000 km and 800-1600°C. Thus, the viscosity of the colder lower-mantle slab would be smaller than that of the hotter surrounding lower mantle due to the small grain size in the slab at least at the top of the lower mantle. The viscosity increases with depth because of the pressure effect on the diffusivity and the grain-size evolution. The grain-size evolution and the viscosity variation are negatively coupled with temperatures, in which the temperature effect on the viscosity apparently becomes small. Therefore, the viscosity of the cold slab material may keep lower than the hotter mantle at deeper depths, however to check this point, the grain size and viscosity variations should be calculated taking the adiabatic temperature increase into accounts. Additionally, although we calculated the grain-size evolution assuming that the secondary phase of ferropericlase is isolated as an initial state, Yamazaki et al. (2014) has suggested that the interconnection of ferropericlase is formed due to the eutectoid

post-spinel transformation, and kept in geological timescales at low temperature conditions of ~700-800°C. This may weaken the cold slab in a different way (i.e., interconnection of the weaker phase in multiple phase system).

Finally, we discuss the viscosity profile in the lower mantle as shown in Fig. 2.22, in the similar way as used in Fig. 2.21. In contrast to the down going material across the 660 km discontinuity where the grain size is reset due to the post-spinel transformation, it is difficult to estimate the grain size of the surrounding lower mantle. Considering the convecting current in the lower mantle, the grain size may be controlled by the grain growth at the hottest region around the bottom of the mantle, where the temperature ranges between 2500-3500 K (e.g., Tateno et al., 2009; Nomura et al., 2014). It is estimated that the bridgmanite grain in the pyrolitic composition grows to ~3-9 mm in 10^8 years at 2500-3500 K, which was considered in the calculation of the viscosity profile in Fig. 2.22. This grain growth may result in that dislocation creep becomes dominant over the diffusion creep (Xu et al., 2011), however the diffusion creep is expected to be still dominant if we consider the faster grain-boundary diffusion obtained in this study.

The similar investigation on the lower mantle viscosity based on the Si diffusivity has been done assuming the grain size of 3 mm in the previous study

(Yamazaki and Karato, 2001). The result on the bridgmanite viscosity recalculated incorporating the new diffusion data (Yamazaki et al., 2000; Xu et al., 2011) are also shown in Fig. 2.22. The viscosity profile calculated in the present study is lower than the model of Yamazaki and Karato (2001) due to the faster grain-boundary diffusivity of this study. In our model, the lower-mantle viscosity can be explained with the possible grain size of 5-9 mm. The slope of the viscosity profile is steeper because of using the constant activation volume in our calculation

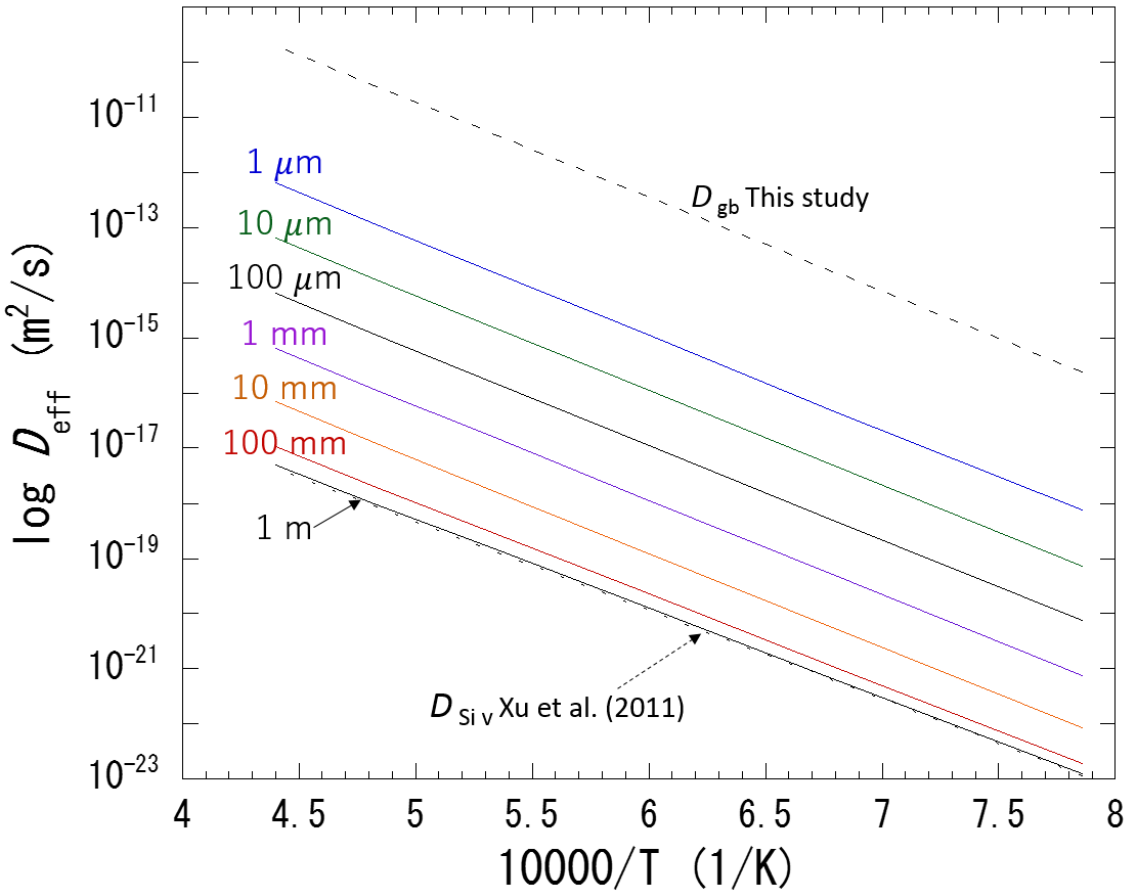

Fig. 2.20 Arrhenius plots of the effective diffusion coefficients (solid line) with grain size. Volume diffusion (Xu et al., 2011, dotted line) and grain-boundary difusion (this study, dashed line) rates are also shown.

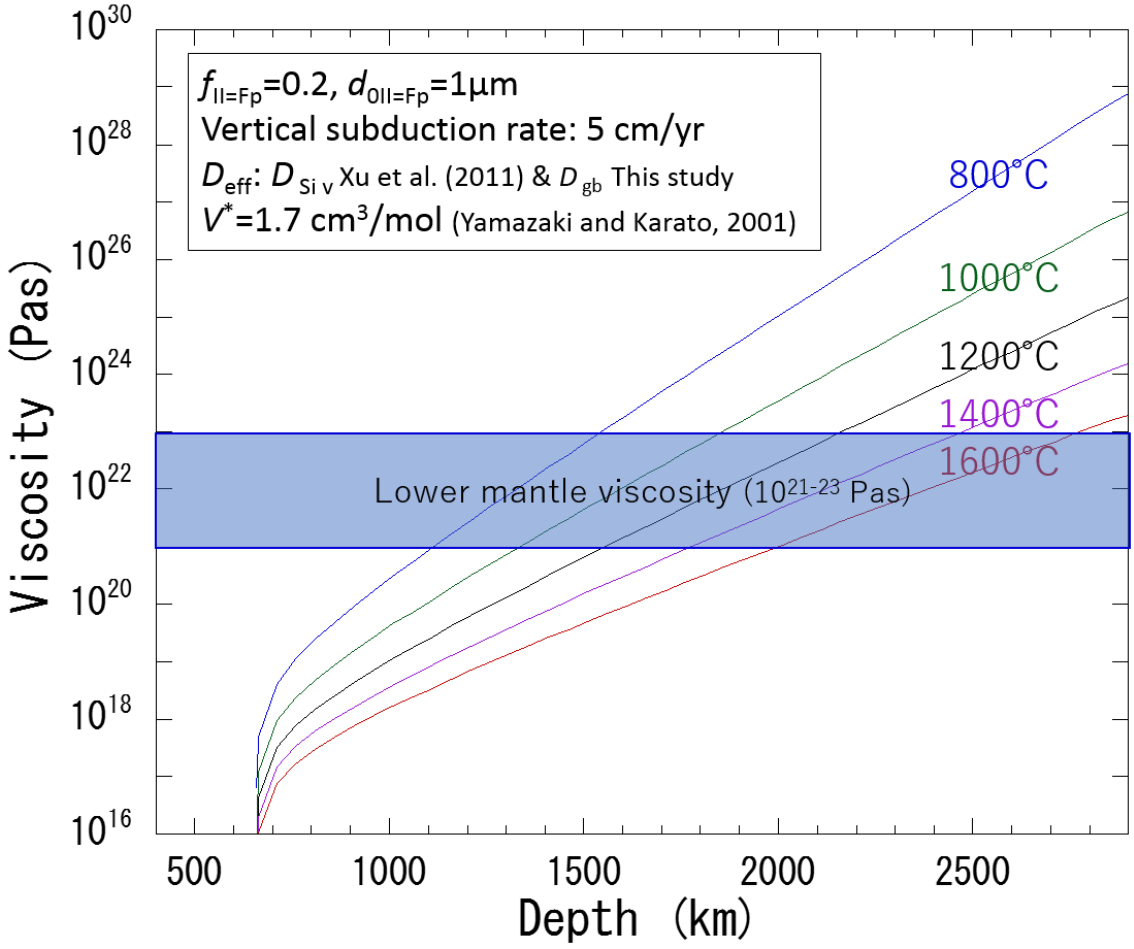

Fig. 2.21 Viscosity variations of the cold lower-mantle slab across the 660 km discontinuity considering the grain-size evolution and the atomic diffusivity.

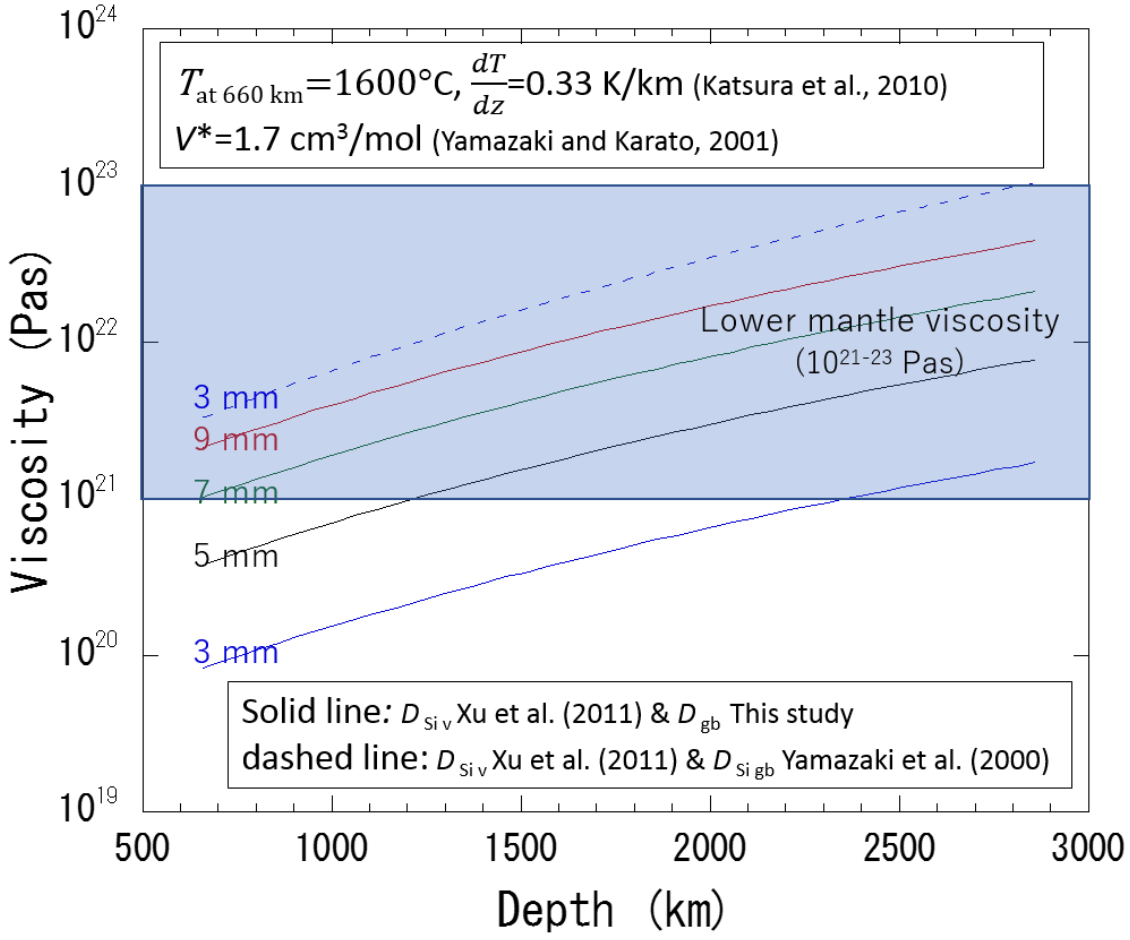

Fig. 2.22 Depth profile of the lower-mantle viscosity calculated based on the Si volume diffusivity (Xu et al., 2011) and the grain-boundary diffusivity estimated from the grain growth kinetics (solid lines). Grain sizes of 3-9 mm are used in the calculation considering the grain growth. The bridgmanite viscosity estimated from the previous study (the grain size was assumed to be 3 mm, Yamazaki and Karato, 2001) is also shown in the dotted line after the recalculation using the new volume diffusion data (Xu et al., 2011).

2.5. Summary

Grain growth experiments of pyrolitic material were conducted at 25-27 GPa and 1600-1950°C for 30-3000 minutes in order to understand the grain-size evolution and the viscosity variations in the lower mantle and lower-mantle slabs. Grain growth in 3 phases of bridgmanite, ferropericlase, and Ca-perovskite, and in 4 phases including majoritic garnet were observed at 25 GPa and 27 GPa, respectively. The grains of minor phases such as ferropericlase and majoritic garnet were solely located at the grain boundary of the major phase of bridgmanite and the grain size ratio between the major and minor phases were roughly constant. These results suggest that the grain growth of bridgmanite in the multi-phase system was controlled by Zener pinning and Ostwald ripening of minor phases. The grain growth kinetics of bridgmanite, ferropericlase, and majoritic garnet in the 4-phase system were constructed from the grain size data obtained at various temperatures and heating durations. The grain size of bridgmanite relative to that of minor phases increases with decreasing in the fractions of minor phases, which can be largely explained by the Zener relationships constructed in the olivine-enstatite system (Tasaka and Hiraga, 2013).

We estimated grain growth kinetics of bridgmanite in the 3-phase system from the grain growth kinetics of ferropericlase and Zener parameters. The grain size of

bridgmanite was estimated to be about 10-200 μm for cold slab conditions at 800-1400°C in 2×10^7 years, and 500-3000 μm for surrounding mantle conditions at 1600-2400°C in 10^8 years. These grain sizes are near the critical grain size between the diffusion and dislocation creep mechanisms (Xu et al., 2011), suggesting that the diffusion creep is dominant under most parts of the lower mantle and changes into the dislocation creep in the highly deformed regions around subducting slabs and the D" layer. The grain size of bridgmanite depends on the chemical composition of the lower mantle (i.e., the minor phase fraction), however the effect is not so large.

It has been suggested that the rate-controlling process is common between the grain growth and diffusion creep in multi-phase system. That is thought to be the Si grain-boundary diffusivity of bridgmanite in the lower mantle. We deduced it from the grain growth kinetics in this study, and estimated the diffusion creep viscosity considering the grain-size evolution. The viscosity of the colder lower-mantle slabs down to the depths of ~1000-1500 km is expected to be weaker than that of the surrounding hotter mantle because of the smaller grain size at the top of the lower mantle. On the other hand, the geophysical models of the lower mantle viscosity ($\sim10^{21\text{-}23}$ Pas) can be partially explained if the grain size becomes enough large around 5-9 mm at the hottest regions of the lower mantle.

References of chapter 2

Ardell, A. J. On the coarsening of grain boundary precipitates. *Acta Metall.* **20,** 601–609 (1972).

Bolfan-Casanova, N., Keppler, H., Rubie, D. C. Water partitioning between nominally anhydrous minerals in the MgO-SiO_2-H_2O system up to 24 GPa: Implications for the distribution of water in the Earth's mantle. *Earth Planet. Sci. Lett.* **182,** 209–221 (2000).

Boioli, F., Carrez, P., Devincre, B., Gouriet, K., Hirel, P., Kraych, A., and Ritterbex, S. Pure climb creep mechanism drives flow in Earth's lower mantle. *Science Advance*. **3**, e1601958 (2017).

Dunn, K. J. and Bundy, F. P. Materials and techniques for pressure calibration by resistance-jump transitions up to 500 kilobars. *Review of Scientific instruments*. **49**, 365-370 (1978).

Dobson, P. D., Dohmen, R., and Wiedenbeck, M. Self-diffusion of oxygen and silicon in $MgSiO_3$ perovskite. *Earth Planet. Sci. Lett.* **270,** 125–129 (2009).

Evans, B., Renner, J., Hirth, G. A few remarks on the kinetics of static grain growth in rocks. *Int. J. Earth Sci.* **90,** 88–103 (2001).

Fei, Y., Van Orman, Li, J., van Westrenee, W., Sanloup, C., Minarik, W., Hirose, K.,

Komabayashi, T., and Funakoshi, K. Experimental determined postspinel transformation boundary in Mg_2SiO_4 using MgO as an internal pressure standard and its geophysical implications. *J. Geophys. Res.* **109**, B02305 (2004).

Foley, B. J. and Long, M. D. Upper and mid-mantle anisotropy beneath the Tonga slab. *Geophys. Res. Lett.* **38**, L02303 (2011).

Forte, A. M., and Mitrovica, J. X. New inferences of mantle viscosity from joint inversion of long-wavelength mantle convection and post-glacial rebound data. *Geophys. Res. Lett.* **23**, 1147-1150 (1996).

Frost, H. J., and Ashby, M. F. DEFORMATION-MECHANISM MAPS. *Pergamon Press.* (1982).

Hiraga, T., Tachibana, C., Ohashi, N., Sano, S. Grain growth systematics for forsterite ± enstatite aggregates: Effect of lithology on grain size in the upper mantle. *Earth Planet. Sci. Lett.* **291,** 10–20 (2010).

Hiraga, T., Nakakoji, T., Nagao, H., Kano, M., and Ito. S. Precise measurements of grain boundary transport properties of polycrystalline forsterite + enstatite by grain growth and creep experiments. *AGU Fall meeting*. MR41E-05 (2016).

Irifune, T., Sekine, T., Ringwood, A. E., Hibberson, W. O. The eclogite-garnetite transformation at high pressure and some geophysical implications. *Earth Planet.*

Sci. Lett. **77,** 245–256 (1986).

Irifune, T. Absence of an aluminous phase in the upper part of the Earth's lower mantle. *Nature* **370,** 131–133 (1994).

Ito, E. Theory and oractice-multianvil calls and high-pressure experimental methods. In: Price, G. D. (Ed.), Minera Physics, Treatse on Geophysics, vol. 2. Elsevier, Amsterdam. 197-230 (2007).

Jeffries, Z., Kline, A. H., Zimmer, E. B. The Determination of Grain Size in Metals. *Trans. AIME*. **57**, 594-607 (1917).

Karato, S. Grain growth kinetics in olivine aggregates. *Tectonophysics* **168,** 255–273 (1989).

Karato, S., Zhang, S., and Wenk. H.-R. Superplasticity in Earth's Lower mantle: Evidence from Seismic Anisotropy and Rock Physics. *Science*. **270**, 458-461 (1995).

Karato, S. Water distribution across the mantle transition zone and its implication for global material circulation. *Earth Planet. Sci. Lett.* **301,** 413–423 (2011).

Katayama, I., Hirose, K., Yurimoto, H., Nakashima, S. Water solubility in majoritic garnet in subducting oceanic crust. *Geophys. Res. Lett.* **30,** 5–8 (2003).

Keppler, H., McCammon, C. A., Rubie, D. C. Crystal-Field and Charge-Transfer

Spectra of (Mg,Fe)SiO_3 Perovskite. *Am. Mineral.* **79,** 1215–1218 (1994).

Keppler, H., Kantor, I., Dubrovinsky, L. S. Optical absorption spectra of ferropericlase to 84 GPa. *Am. Mineral.* **92,** 433–436 (2007).

Kubo, T., Ohtani, E., Kato, T., Urakawa, S., Suzuki, A., Kanbe, Y., Funakoshi, K., Utsumi, W., Fujino, K. Formation of metastable assemblages and mechanism of the grain-size reduction in the postspinel transformation of Mg_2SiO_4. *Geophys. Res. Lett.* 27, 807-810 (2000).

Kubo, T., Kaneshima, S., Torii, Y., and Yoshioka, S. Seismological and experimental constrains on metastable phase transformations and rheology of the Mariana slab. *Earth Planet. Sci. Lett.* **287**, 12–23 (2009).

Lay, T., Williams, Q., and Garnero, E. J. The core-mantle boundary layer and deep Earth dynamics, *Nature*. **392**, 461-468 (1998).

Lau, H. C. P., Mitrovica, J. X., Austermann, J., Crawford, O., Al-Attar, D., and Latychev, K. Inferences of mantle viscosity based on ice age data sets: radial structure. *J. Geophys. Res.* **121**, doi: 10.1002/2016JB013043 (2016).

Mainprice, D., Tommasi, A., Ferré, D., Carrez, P., and Cordier, P. Predicted glide system and crystal prefferred orientations of polycrystalline silicate Mg-Perovskite at high pressure: Implications for the seismic anisotropy in the

lower mantle. *Earth Planet. Sci. Lett.* **371**, 135-144 (2008).

Meade, C., Reffner, J. A., Ito, E. Synchrotron Infrared Absorbency Measurements of Hydrogen in $MgSiO_3$ Perovskite. *Science (80-.).* **264,** 1558–1560 (1994).

Mitrovica, J. X., and Forte, A. M. A new inference of mantle viscosity based upon joint inversion of convection and glacial isostatic adjustment data. *Earth Planet. Sci. Lett.* **225**, 177-189 (2004).

Mitrovica, J. X., Hay, C. C., Morrow, E., Kopp, R. E., Dumberry, M., and Stanley, S. Reconciling past changes in Earth's rotation with 20th century global sea-level rise: Resolving Munk's enigma. Oceanography. doi: 10.1126/sciadv.1500679 (2015).

Moore, M. M. and Garnero E. J. Shear wave splitting and waveform complexity complexity for lowermost mantle structures with low-velocity lamellae and transverse isotropy. *J. Geophys. Res.* **109**, B02319 (2004).

Murakami, M., Hirose, K., Yurimoto, H., Nakashima, S., and Takafuji, N. Water in Earth's Lower Mantle. *Science*. **295**, 1885-1887 (2002).

Nakada, M., Lambeck, K. Late Pleistocene and Holocene sea-level change in the Australian region and mantle rheology. *Geophys. J. R. Astron. Soc.* **96,** 497–517 (1989).

Nakada, M., Okuno, J., and Irie, Y. Inference of viscosity jump at 670 km depth and lower mantle viscosity structure from GIA observations. Geophys. J. Int. doi: 10.1093/gji/ggx519 (2018).

Nishi, M., Nishihara, Y., Irifune, T. Growth kinetics of $MgSiO_3$ perovskite reaction rim between stishovite and periclase up to 50 GPa and its implication for grain boundary diffusivity in the lower mantle. *Earth Planet. Sci. Lett.* **377–378,** 191–198 (2013).

Nishihara, Y., Shinmei, T., Karato, S. I. Grain-growth kinetics in wadsleyite: Effects of chemical environment. *Phys. Earth Planet. Inter*. **154,** 30–43 (2006).

Nishiyama, N., Yagi, T. Phase relation and mineral chemistry in pyrolite to 2200°C under the lower mantle pressures and implications for dynamics of mantle plumes. *J. Geophys. Res. Solid Earth* **108,** doi:10.1029/2002JB002216 (2003).

Nishiyama, N., Irifune, T., Inoue, T., Ando, J. ichi, Funakoshi, K. ichi. Precise determination of phase relations in pyrolite across the 660 km seismic discontinuity by in situ X-ray diffraction and quench experiments. *Phys. Earth Planet. Inter*. **143,** 185–199 (2004).

Nishizawa, T. Grain Growth in Single- and Dual-Phase Steels. *Testu-to-Hagané*. **15**, 194-202 (1984).

Nomura, R., Hirose, K., Uesugi, K., Ohuishi, Y., Tsuchiyama, A., Miyake, A., and Ueno, Y. Low Core-Mantle Boundary Temperature Inferred from the Solidus of Pyrolite, *Science*. **343**, 522-525 (2014).

Ohuchi, T., Nakamura, M. Grain growth in the forsterite-diopside system. *Phys. Earth Planet. Inter*. **160,** 1–21 (2007).

Okamoto, A. and Hiraga, T. Diffusion mechanism of creep and grain growth of two-phase polymineralic rocks: Constrains on grain size and viscosity of the lower mantle. *JpGU*. SIT22-11

Paterson, M. S. The determination of hydroxyl by infrared absorption in quartz, silicate glass and similar materials. *Bulletin Mineralogie*. **105**, 20-29 (1982).

Pelteir, W. R. Mantle Viscosity and Ice-Age Ice Sheet Topography. *Science*. **273**, 1359-1364 (1996).

Peltier, W. R. POSTGLACIAL VARIATIONS IN THE LEVEL OF THE SEA: IMPLICATIONS FOR CLIMATE DYNAMICS AND SOLID-EARTH GEOPHYSICS. *Reviews of Geophysics*. **36**, 603-6089 (1998).

Rudolph, M. L., Lekić, V., and Lithgow-Bertelloni, C. Viscosity jump in Earth's mid-mantle. *Science*. **350**, 1349-1352 (2015).

Sauveur, A. Microstructure of steel. *Trans. AIME*. **167**, 546-557 (1894).

Solomatov, V. S. Grain size-dependent viscosity convection and the thermal evolution of the earth. *Earth Planet. Sci. Lett.* **191,** 203–212 (2001).

Speight, M. V. Growth kinetics of grain-boundary precipitates. *Acta Metall.* **16,** 133–135 (1968).

Takayama, Y. Methods for estimation and determination of grain size. *J. Jpn, Inst. Light Met*, **44,** 48-56 (1994).

Tasaka, M., and Hiraga, T. Influence of mineral fraction on the rheological properties of forsterite + enstatite during grain size sensitive creep: Grain size and grain growth laws. *J. Geophys. Res. Solid Earth* **118,** 3970–3990 (2013).

Tateno, S., Hirose, K., Sata, N., and Ohishi, Y. Determination of post-pervskite phase transition boundary up to 4400 K and implications for thermal structure in D" layer. *Earth Planet. Sci. Lett.* **277,** 130–136 (2009).

Tsujino, N., and Nishihara, Y. Grain-growth kinetics of ferropericlase at high-pressure. *Phys. Earth Planet. Inter.* **174,** 145–152 (2009).

Tsujino, N., Nishihara, Y., Yamazaki, D., Seto, Y., and Takahashi, E. Mantle dynamics inferred from the crystallographic preferred orientation of bridgmanite. *Nature.* **539,** 81–84 (2016).

Van Orman, J. A., Fei, Y., Hauri, E. H., Wang, J. Diffusion in MgO at high pressures:

Constraints on deformation mechanisms and chemical transport at the core-mantle boundary. *Geophys. Res. Lett.* **30,** 26–29 (2003).

Xu, J., Yamazaki, D., Katsura, T., Wu, Xi., Remmert, P., Yurimoto, H., Chakraborty, S., Silicon and magnesium diffusion in a single crystal of MgSiO3perovskite. *J. Geophys. Res. Solid Earth* **116,** 1–8 (2011).

Yamazaki, D., Kato, T., Ohtani, E., Toriumi, M. Grain Growth Rates of $MgSiO_3$ Perovskite and Periclase Under Lower Mantle Conditions. *Science*. **274**, 2052-2054 (1996).

Yamazaki, D., Kato, T., Yurimoto, H., Ohtani, E., Toriumi, M. Silicon self-diffusion in MgSiO3 perovskite at 25 GPa. *Phys. Earth Planet. Inter.* **119,** 299–309 (2000).

Yamazaki, D., and Karato, S., Some mineral physics constraints on the rheology and geothermal structure of Earth ' s lower mantle. *Am. Mineral.* **86,** 385–391 (2001).

Yamazaki, D. and Karato, S. Fabric development in (Mg,Fe)O during large strain, shear deformation: implications for seismic anisotropy in Earth's lower mantle. *Phys. Earth Planet. Inter.* **131,** 251-267 (2002).

Yamazaki, D., Matsuzaki, T., and Yoshino, T. Grain growth kinetics of majorite and stishovite in MORB. *Phys. Earth Planet. Inter.* **183,** 183–189 (2010).

Yamazaki, D., Yoshino, T., and Nakakuki, T. Interconnection of ferro-periclase controls

subducted slab morphology at the top of the lower mantle. *Earth Planet. Sci. Lett.* **403,** 352–357 (2014).

Wookey, J., Kendall, J., and Barruol, G. Mid-mantle deformation iferred from seismic anisotropy. *Nature*. **415**, 777-780 (2002).

Wookey, J. and Kendall, J. Evidence for midmantle anisotropy from shear wave splitting and the influence of shear-couples P waves. *J. Geophys. Res.***109**, B002871 (2004).

Acknowledgements

I would like to thank to Prof. T. Kubo and the late Prof. T. Kato for constructive discussions, suggestions and continuous encouragement through this work. I am also grateful to Dr. S. Azuma for his helpful advices and valuable discussions, and Prof. S. Kaneshima, Prof. T. Ikeda, Prof. Y. Nishihara, Prof. A. Toramaru, and Prof. T. Hiraga for their constructive suggestions. I am grateful to Dr. S. Uehara and seminar members for useful discussions.

I wish to thank Dr. T. Kikegawa, Prof. A. Suzuki, Dr. Y. Higo, Dr. Y. Tange, and Dr. D. Wakabayashi for their technical help, and M. Ikehara, K. Kamura and K. Moriyama for their support during the in-situ X-ray diffraction experiments at the synchrotron radiation facilities of SPring-8 and PFAR. I am also grateful to S. Koizumi and M. Nishi for providing the starting materials. I would like to thank A. Toramaru for FTIR measurements and K. Shimada for technical assistance for the use of FE-SEM/EDS and FE-EPMA/EDS.

In-situ X-ray diffraction experiments were conducted at PFAR-NE7 of the Photon Factory (proposal nos. 2014G680 and 2016G598) and BL04B1 beamline of SPring-8 (proposal nos. 2015B1545, 2016A1467, 2016B1358, and 2017A1535).